Nanoscale Multimodal Characterization of Operating Electrolyte-Gated Transistors

Shubham Tanwar

Nanoscale Multimodal Characterization of Operating Electrolyte-Gated Transistors

UNIVERSITAT DE BARCELONA

FACULTY OF PHYSICS

Doctoral Thesis
submitted by

Shubham Tanwar

under supervision of
Dr. Adrica Kyndiah and Dr. Gabriel Gomila Lluch

(2023)

Nanoscale Multimodal Characterization of Operating Electrolyte-Gated Transistors

UNIVERSITAT DE BARCELONA

Memoria presentada para optar al grado de doctor por la
Universitat de Barcelona.

Programa del doctorado en	Biomedicina
Autor	Shubham Tanwar
Directores y Tutor	Dr. Adrica Kyndiah y Dr. Gabriel Gomila Lluch
Lugar de realización de la tesis	Instituto de Bioingeniería de Cataluña

Shubham Tanwar **Dr. Adrica Kyndiah** **Dr. Gabriel Gomila Lluch**

Doctoral program in Biomedicine, Biomedical Engineering research line at the Universitat de Barcelona, Faculty of Physics.

In cooperation with Institute for Bioengineering of Catalonia, Nanoscale Bioelectrical Characterization group.

This project has received funding from the European Union’s Horizon 2020 research and innovation program, under the Marie Sklodowska-Curie grant agreement no. 813863.

Dedicated to my parents and my beloved family

Abstract

Electrolyte-gated transistors (EGTs) have emerged as key platforms for transducing and amplifying biological and biochemical signals, making them an integral part of diverse biosensing and bioelectronic applications ranging from single molecule biosensors to neuromorphic devices. Despite being the foundational architecture, the fundamental understanding of the nanoscale electronic and ionic transport governing the device operation remains poor, which hinders further progress in the rational and targeted optimization of devices for various applications. The limitation mainly stems from the lack of characterization methods that can probe ionic and electronic transport processes in operating devices at the nanoscale under electrolyte environments and in application-relevant conditions. Further complexity arises due to diverse molecular design of organic semiconductors that expresses wide variety of coupled electrical and mechanical behaviours.

In this thesis, we developed an advanced multimodal characterization method based on in-liquid Scanning Dielectric Microscopy (SDM) that simultaneously probes relevant electrical and mechanical properties at the nanoscale in functional EGTs. The presented method significantly advances an earlier implementation of in-liquid SDM for the same purpose by adding automated data acquisition and analysis functionalities along with technical improvements for the comprehensive characterization of EGTs. We introduced a straightforward and robust approach for data interpretation and representation that effectively eliminated experimental artefacts and the calibration procedures, enabling rapid and accurate analysis. The approach also enabled quantification of the local electric potential directly from raw experimental data, thereby providing direct access to fundamental charge transport parameters such as contact access resistances, inter-and intra-domain charge transport, and anisotropy, which weren't accessible earlier at the nanoscale in operating EGTs.

We studied two varieties of EGTs, namely Electrolyte-Gated Organic Field-Effect Transistors (EGOFETs) and Organic Electrochemical Transistors (OECTs), which exhibit distinct operating mechanisms. We first focused on EGOFETs based on a blend of organic semiconducting material diF-TES-ADT and the insulating polymer polystyrene (PS), where we investigated the local electrical properties in various operating regimes, namely sub-threshold, linear and saturation. This investigation reveals that the pinch-off characteristics are dependent on the microstructural property of the organic semiconducting blend, which controls the extension of the pinch-off into the channel region. We also investigated regions consisting of different structural features and their influence on the evolution of local electrical properties, thereby identifying the attributes that lead to inferior charge transport characteristics. Using the developed electric potential mapping mode, we quantified the impact of grain boundaries and contact access resistances and observed that the intrinsic conductivity of individual grains can be as high as 40S/m, whereas the effective device conductivity is a factor of 10 lower, indicating serious charge transport bottlenecks. Therefore, focusing on contact and grain boundary interface engineering would potentially enable reaching electrical characteristics close to that of individual crystalline domains.

After that, we focused on OECTs based on ladder-type polymer BBL, where we investigated the coupled electrical and mechanical behaviour across different operating regimes by utilizing the multimodal character of our in-liquid SDM implementation. The spatial variability in the mechanical stiffness in response to applied drain potentials is correlated with the corresponding local electrical properties. A peculiar sudden phase change in mechanical response is observed that coincides with the maximum (positive or negative) transconductance points of the device, where an influx of ions into the polymer affirmed with a simultaneous increase of the effective interfacial capacitance happens. The local electrical mapping is also used to explain device current-voltage characteristics at high doping conditions in the negative transconductance regime.

In a nutshell, the thesis provides a detailed understanding of the operating mechanism in a variety of EGTs through a multimodal nanoscale perspective and lays the foundation for further advanced studies.

Resumen

Los transistores que utilizan dieléctricos líquidos (electrolitos) (EGTs, por sus siglas en inglés) han surgido como plataformas clave para la transducción y amplificación de señales biológicas y bioquímicas, convirtiéndolos en una parte integral de diversas aplicaciones de biosensado y bioelectrónica, que van desde biosensores de moléculas individuales hasta dispositivos neuromórficos. A pesar de ser una arquitectura fundamental, la comprensión básica del transporte electrónico y iónico a escala nanométrica que rige el funcionamiento de estos dispositivos sigue siendo limitada, lo que dificulta el progreso en la optimización racional de los dispositivos para diversas aplicaciones. La principal limitación se debe a la falta de métodos de caracterización que puedan sondear los procesos de transporte iónico y electrónico en dispositivos en funcionamiento a escala nanométrica en medios electrolitos y en condiciones relevantes para las aplicaciones. Además, la presencia del electrolito induce una mayor complejidad debido a que los semiconductores orgánicos en contacto con ellso exhiben una amplia variedad de comportamientos eléctricos y mecánicos acoplados.

En esta tesis, hemos desarrollado un método avanzado de caracterización multimodal basado en la Microscopía Dieléctrica de Barrido en medio Líquido (SDM, por sus siglas en inglés) que sondea simultáneamente propiedades morfológicas, eléctricas y mecánicas relevantes a escala nanométrica en EGT en funcionamiento. El método presentado constituye un avance significativo de una implementación previa de la SDM en líquido con el mismo propósito, al agregar adquisición automatizada de datos y funcionalidades de análisis, junto con la consideración de propiedades mecánicas y mejoras técnicas para la caracterización integral de EGT. Además, se ha introducido un enfoque directo y robusto para la interpretación y representación de datos, que elimina eficazmente los artefactos experimentales y los procedimientos de calibración, permitiendo un análisis rápido y preciso. Este enfoque también ha permitido la cuantificación del potencial eléctrico local

directamente a partir de datos experimentales sin procesar, lo que proporciona acceso directo a parámetros fundamentales relacionados con el transporte de los portadores de carga, tales como la resistencias de acceso de contacto, transporte de carga entre dominios y dentro de ellos, y anisotropía, que antes no se podían obtener a escala nanométrica en EGT en funcionamiento.

En la tesis se han estudiado dos variedades de EGTs, a saber, Transistores Orgánicos de Efecto de Campo con Electrolito (EGOFETs) y Transistores Orgánicos Electroquímicos (OECTs), que presentan distintos mecanismos de funcionamiento. En primer lugar, nos hemos centrado en los EGOFETs basados en una mezcla de material semiconductor orgánico diF-TES-ADT y el polímero aislante poliestireno (PS), donde hemos investigado las propiedades eléctricas locales en varios regímenes de funcionamiento, a saber, subumbral, lineal y de saturación. Esta investigación ha revelado que las características de estrangulamiento del canal de conducción dependen de la microestructura de la mezcla semiconductora orgánica, que controla la extensión del estrangulamiento en la región del canal. También hemos investigado regiones que consisten en diferentes características estructurales y su influencia en la evolución de las propiedades eléctricas locales, identificando así los atributos que conducen a características de transporte de carga inferiores. Utilizando el modo de mapeo de potencial eléctrico desarrollado, hemos cuantificado el impacto de los límites de grano y las resistencias de acceso de contacto, y hemos observado que la conductividad intrínseca de los granos individuales puede ser tan alta como 40S/m, mientras que la conductividad efectiva del dispositivo es un factor 10 menor, lo que indica serios cuellos de botella en el transporte de carga. Por lo tanto, centrarse en la ingeniería de la interfaz de contacto y los límites de grano podría permitir alcanzar características eléctricas cercanas a las de los dominios cristalinos individuales.

Por otra parte, se han estudiado los OECTs basados en el polímero de tipo escalera BBL, donde investigamos el comportamiento eléctrico y mecánico acoplado en diferentes regímenes de funcionamiento utilizando el carácter multimodal de nuestra implementación de la SDM en líquido. Se ha visto que la variabilidad espacial en la rigidez mecánica en respuesta a los potenciales de drenaje aplicados se correlaciona con las correspondientes propiedades eléctricas locales. Además, se ha observado un peculiar cambio repentino de fase en la respuesta mecánica que coincide con los puntos máximos (positivos o negativos) de transconductancia del dispositivo, donde ocurre un flujo de iones al polímero, que conlleva un aumento simultáneo de la capacitancia interfacial efectiva. El mapeo eléctrico local también se ha utilizado para explicar las características corriente-voltaje del dispositivo en condiciones de alto dopaje en el régimen de transconductancia negativa.

En resumen, la tesis proporciona el desarrollo de instrumentación de caracterización que ha permitido una comprensión detallada del mecanismo de funcionamiento en una variedad de EGTs a través de una perspectiva nanométrica multimodal y sienta las bases para futuros estudios avanzados.

Acknowledgments

First and foremost, I would like to thank my advisors, Dr. Adrica Kyndiah and Dr. Gabriel Gomila, for their persistent support, patience, and mentorship throughout this journey. Their expertise, insightful feedback, and continuous motivation have been instrumental in shaping this thesis and my development as a researcher. They have been the perfect set of mentors one could ask for. A sincere thanks also to the past and present members of the Nanobioelec group at IBEC for a great time: Larissa, Martina, Marti, Annalisa, Aurora, Ruben, Stella, Hari and Helena.

I also extend my thanks to collaborators from ICMAB, Linköping University and IIT Milano for access to state-of-the-art devices: Dr. Marta Mas-Torrent, Dr. Simone Fabiano, Dr. Fabrizio Antonio Viola, Sara Ruiz-Molina, Han-Yan Wu and Chi-Yuan Yang. Also, a special thanks to all BORGES ESRs for a wonderful PhD experience.

I would like to express my heartfelt gratitude to my parents and family, for their unconditional love, encouragement, and unwavering belief in me. Their constant support, understanding, and sacrifices throughout my educational journey have been the driving force behind my achievements. I owe them everything. And to the people who have been like a family in Barcelona: Martina and Suze, thank you so much for everything and for making this journey memorable for a lifetime.

It would not be fair not to thank the IBEC administration who has handled amazingly all the bureaucratic processes, especially Karem and Berta, who have been my go-to point of contact. I further acknowledge the funding from the European Commission through BORGES Marie Skłodowska-Curie ITN under Horizon 2020 for enabling the unique international and collaborative PhD experience. The extended funding through the EIC PathFinder PRINGLE project has also enabled further progress in the last phase of my PhD.

Thank you all for being a part of my journey.

Abbreviations

AFM	Atomic Force Microscopy
BORGES	Biosensing with ORGanic ElectronicS
EDL	Electrical Double Layer
EGOFET	Electrolyte-Gated Organic Field-Effect Transistor
EGT	Electrolyte-Gated Transistor
ESM	Electrochemical Strain Microscopy
FEM	Finite Element Method
FET	Field-Effect Transistor
KPFM	Kelvin Probe Force Microscopy
MOSFET	Metal Oxide Semiconductor Field-Effect Transistor
OECT	Organic Electrochemical Transistor
OFET	Organic Field-Effect Transistor
OMIEC	Organic Mixed Ionic-Electronic Conductor
SDM	Scanning Dielectric Microscopy
TFT	Thin-Film Transistor

Contents

PART I

STATE OF THE ART

Chapter 1

Introduction

Abstract This introductory chapter briefly introduces Electrolyte-Gated Transistors (EGTs) based on organic semiconductors and mixed ionic-electronic conductors, describes their operating regimes, I-V characteristics, and figures of merits. Two variety of EGTs, namely Electrolyte-Gated Organic Field-Effect Transistors (EGOFETs) and Organic Electrochemical Transistors (OECTs) are discussed, highlighting their distinct operating mechanism and respective applications. The later part of the chapter deals with the operando characterization, requirements and challenges. A brief literature review is presented focusing on various operando scanning probe microscopy-based characterization techniques implemented and developed to reveal the dynamic multifunctional physical and chemical characteristics of organic semiconductors and devices at length scales varying from micrometres to nanometres. We conclude this chapter by highlighting directions for further development of operando techniques and the challenges this thesis aims to address and point towards the potential applications in revealing the fundamental characteristics of organic electronic devices.

1.1. Organic Semiconductors

Organic semiconducting materials have enabled emerging disruptive technology in the electronics arena, such as flexible displays[1], and are now enabling futuristic bioelectronic technologies[2] in the healthcare arena. As a class of materials, organic semiconductors are pi-conjugated small molecules and organic polymers exhibiting unique electronic, optical, and mechanical properties readily tunable by chemical design[3,4], making them a perfect material for a broad spectrum of applications, offering unparalleled opportunities for innovation in creating devices with various functionalities. One of the main appeals of organic semiconducting materials is their mechanical flexibility and the ability to be solution-processable at low temperatures. It allows for fabricating lightweight, thin, and flexible electronic devices, which can be produced using cost-effective techniques such as inkjet printing or roll-to-roll processing. As a result, organic semiconductors have found potential applications in a variety of sectors, from flexible electronics[5], organic photovoltaics[6], wearable electronics[7], and health sensors[8] to futuristic body-machine interfaces[9] and bioelectronic medicines[10], to name just a few.

Historically, organic semiconductors have exhibited inferior charge transport capabilities in comparison to inorganic semiconductors due to their chemical composition; however, this exact chemical nature also grants them processing versatility and unique properties, for example, the ability of low-temperature deposition on unconventional substrates like plastic, metal foil, paper and even textile which is not possible with silicon, and thus holds significant implications for emerging technologies that rely on more advanced features. Therefore, organic semiconductors should not be viewed or aimed at replacing conventional semiconductors but as a facilitator for more-than-moore technologies such as for integrating sensing capabilities with memory and processing[11].

One might ask, what gives organic materials such an ability for functional diversification? The answer is in the carbon atom! The carbon atom in organic materials gives them unique and highly tunable characteristics, owing to its ability to hybridize in three different configurations, namely sp^3, sp^2 and sp hybridization, as shown in Figure 1.1. Carbon atoms form bonds by mixing different orbitals, namely s- and p-orbitals, with varying s and p characters. sp^3 hybridizations mix one s-orbital and three p-orbitals, namely p_x, p_y and p_z, forming four σ bonds. Whereas, sp^2 hybridizations mix one s-orbital and two p-orbitals (p_x and p_y), giving rise to three σ bonds, and the remaining unhybridized p_z makes the π bond. Finally, the sp hybridizations mix one s-orbital and one p-orbitals, giving rise to two σ and two π bonds. The type of hybridization of the carbon atom has a direct influence on the resulting molecular geometry - for example, sp^3 hybrid orbitals arrange in tetrahedral, whereas the other two generally give trigonal planar (sp^2) and linear (sp) structures, as shown in Figure 1.1B. The characteristics of bonds formed between atoms also determine the charge transport properties. For example, the σ bonds between two atoms formed by head-on overlapping of orbitals give σ electrons a localized character. In contrast, the π bond formed by the side-by-side overlap of π orbitals leads to delocalized π electrons over these atoms, which can be utilized for electrical conduction. The σ and π bond formation is shown in Figure 1.1(C-D) for the simple organic molecule Ethene (C_2H_4).

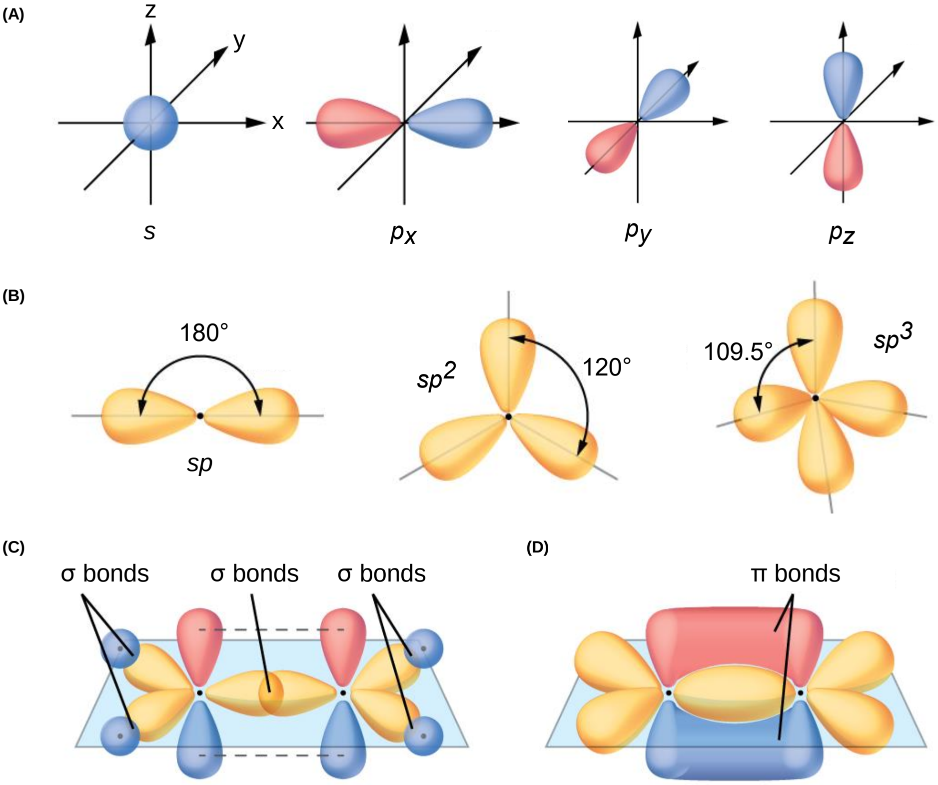

Figure 1.1: (A) The s-orbital and p-orbitals (p_x, p_y and p_z), (B) The hybridized orbitals (sp, sp^2 and sp^3) used in bond formation along with geometry, (C) The σ bonds in Ethene molecule (C_2H_4) showing one C-C σ (middle one) and four C-H σ bonds (blue spheres are hydrogen atoms), and (D) also showing one π bond formed by the side-by-side overlap of the two unhybridized p orbitals of the two carbon atoms. Adapted from reference [12] (CC BY 4.0).

Organic compounds for electronic applications are generally cyclic/rings consisting of alternate single (σ bond) and double (σ and π bond) bonds that allow the possibility of delocalization of π electrons over the whole ring and are thus crucial for charge transport in these conjugated systems. The spatial extent of π electrons delocalization determines the conducting/semiconducting properties of these molecules. For example, Benzene (Figure 1.2 A and 1.2 B) has delocalized electrons but is an insulator due to quantum confinement effects administered by the small spatial extent of π electrons. On the other hand, Pentacene (Figure 1.2 C and 1.2 D) consisting of five linearly-fused benzene rings is an organic semiconductor due to increased spatial delocalization.

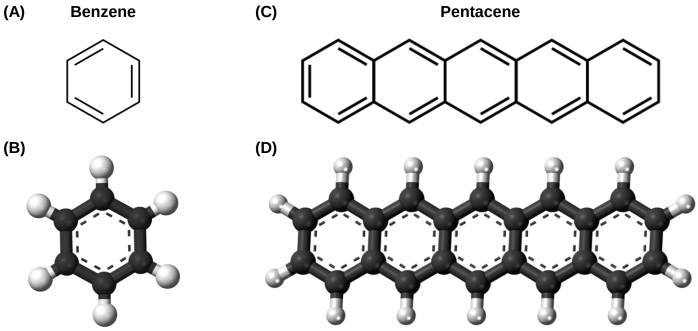

Figure 1.2: (A) The chemical structure of Benzene, along with (B) the ball-and-stick model showing carbon atoms in black and hydrogen in white. Similarly, (C) and (D) show the chemical structure of Pentacene. The dashed circles in the ball-and-stick model represent the delocalization of *pi* electrons.

In general, dynamic control over this delocalization, for example, by changing the hybridization of some carbon atoms to sp^3, can lead to tunable systems[13]. The functionalities of these systems are further extended through the diverse toolbox of synthetic organic chemistry for various emerging technologies[3].

1.2. Charge Transport in Organic Semiconductors

The molecular design of the organic material and its supramolecular assembly into thin films plays a central role in determining its charge transport characteristics. The molecular structure dictates intramolecular and intermolecular charge transport. It defines pathways for charge injection, extraction, trapping, recombination, and transfer which can be tuned through the versatile toolbox of synthetic organic chemistry for the desired applications[3]. For example, improving spatial delocalization of the π-orbitals by the rational introduction of substituents into the conjugation structure of the polymer backbone enhances electronic charge transport while altering the side chains of the backbone facilitates ionic intercalation, solubility, and processability of the material. The hierarchical assembly of the elementary molecular units into controlled thin film microstructures is also critical for long-range efficient charge transport. The well-order molecular packing promotes intermolecular charge-hopping between adjacent polymer units, thereby improving charge carrier mobility. In addition, molecular engineering embodies possibilities for emergent changes during device operation in response to applied electric fields, driving multiscale physical and chemical processes that give dynamic electronic, ionic, morphological, structural, and mechanical behaviour.

Organic transistors with solid dielectrics are among the popular devices that have received significant attention in the last decades for numerous applications such as in flexible electronics[5], memory devices[14,15], ionizing radiation sensing[16], health care[17], logic circuits[18] and opto-electronics[19]. Transistors gated through an aqueous electrolyte, known as Electrolyte-Gated Transistors (EGTs), have also been developed and are of central interest in biosensing and bioelectronic applications. EGTs provide the right physiological environment for interfacing with different biological and biochemical inputs and thus have emerged as the fundamental building block for various technologies. EGT is an umbrella term that includes inorganic materials as well; however, in this thesis, the discussion is limited to organic materials. Nevertheless, the objectives of the thesis and the developments presented are easily transferable to other systems of interest.

The following section will present the EGT architecture and its two main variants, namely EGOFETs and OECTs, which exhibit distinct operational mechanisms. Additionally, we will discuss figures of merits utilized to evaluate their performance and explore the specific applications they address.

1.3. Electrolyte-Gated Transistors (EGTs)

Electrolyte-Gated Transistors (EGTs) have emerged as an integral part of numerous applications in biosensing and bioelectronics[26,29], owing to their remarkable ability to efficiently transduce biological events into amplified electronic signals while stably operating in aqueous electrolytes. A typical EGT is a three-terminal device, as shown in Figure 1.4A, consisting of a semiconducting channel between

The first demonstration of Electrolyte-Gated Transistor (1984)[20]

The first demonstration of an electrolyte-gated transistor was by Wrighton and colleagues in 1984, using polypyrrole as the channel material and deoxygenated $CH_3CN/0.1M[n-Bu_4N]ClO_4$ as the electrolyte. They defined their device as a type of "chemiresistor" where an electrical signal oxidizes the chemical layer polypyrrole and dramatically changes its resistance. They noted that the threshold voltage could be tuned by rationally modifying the underlying molecular material. Since this demonstration, EGTs have undergone tremendous progress in terms of molecular modifications for efficient charge transport[3,4], interface engineering for enhanced charge injection[21–24], and improved fundamental understanding of the charge transport processes[25–28].

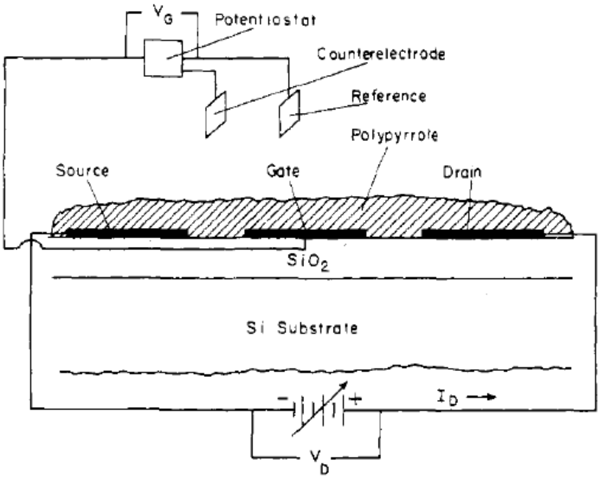

Figure 1.3: Architecture of the first reported EGT. Reproduced with permission from reference [20]. Copyright 1984 American Chemical Society.

source and drain electrodes capacitively coupled with the gate electrode through mobile ions in the electrolytes. Applying an electric field on the gate electrode with respect to the source allows control over the free charge carrier density of the semiconducting channel. A voltage applied to the drain electrode with respect to the source drives the charges from the source to the drain and sets up the drain current, eventually modifying the spatial distribution of the free charge carrier density.

The hallmark distinction of EGTs with respect to solid-state transistors is the low-voltage operation that comes from the high interfacial capacitances of the electrolyte interfaces involved. In EGTs, the capacitance of the semiconductor/-electrolyte interfaces are of the order of a few up to hundreds of $\mu F/cm^2$, whereas in OFETs, the dielectric capacitance is in the nF/cm^2 scale[30]. So, to inject the same level of charge carriers in the semiconductor, a lower voltage is required in EGTs ($Q = CV$). In electrophysiology and for many biosensors, low-voltage operation is of utmost importance. Also, another advantage for such applications is that in EGTs, the position of the gate electrode is not crucial to modulate the charge density of the channel as only the interface (Stern+diffuse) capacitance plays a role, while the contribution of the bulk electrolyte capacitance can be ignored for DC/low-frequency operation in electrolyte media. This can be seen from how the voltage applied at the gate electrode with respect to the source is distributed among different parts of the gate/electrolyte/semiconductor/source interface, as shown in Figure 1.5, with no voltage drop in the bulk electrolyte. Nevertheless, different architectures of the EGT exist suitable for specific applications.

1.3.1. Architectures of EGTs

Different variations exist in the geometry of the EGTs, and depending on the application, one design might be preferred over the others. Mainly the position of the gate electrode and electrolyte with respect to the channel is a distinguishing factor[29]. The most common one is a top-gated architecture, as shown in Figure 1.4A. The gate can also be positioned on the same device substrate used for source and drain electrodes (co-planar gate). However, if a clean gate interface is required, like for sensing applications, the co-planar design might not be the best strategy owing to the difficulty of functionalizing only the gate surface without exposing the semiconducting channel area during the process. Three variations exist for in-plane gates: a side-gated or planar gate architecture shown in Figure 1.4B, a less-common bottom-gate architecture shown in Figure 1.4C where generally a solid electrolyte is used for structural integrity, and lastly floating or extended gate architecture shown in Figure 1.4D for separating the recognition and sensing area in separate chambers which are capacitively coupled by the middle floating gate. The floating gate architecture is helpful for cases where the biological pro-

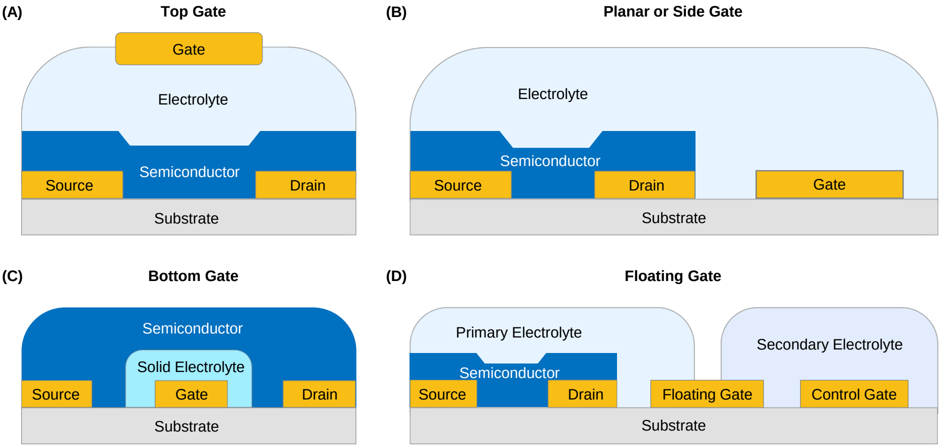

Figure 1.4: Schematics of basic architectures of Electrolyte-Gated Transistors (EGTs) distinguished by the position of the gate electrode relative to the channel (not to scale). (A) Top gate, (B) Planar/Side gate, (C) Bottom gate, and (D) Floating gate.

cess requires a specific electrolyte incompatible with the semiconductor and also avoids unspecific interactions of the biological media/analyte with the semiconductor, which could otherwise happen in other geometries; however, it needs to be designed judicially to exploit the amplifying character of EGTs fully[31].

1.3.2. Choice of Gate Electrode: Polarizable and Non-Polarizable

The choice and type of gate electrode greatly influence how the applied gate voltage is distributed among different parts of the gate/electrolyte/semiconductor/-source interface. The gate can be classified into polarizable and non-polarizable electrodes, depending on the polarizability of the gate/electrolyte interface[29]. A polarizable interface is electrically equivalent to a capacitor, illustrated by the occurrence of charge separation. In contrast, a non-polarizable interface is electrically equivalent to a resistor and illustrated by no charge separation. Using non-polarisable electrodes practically vanishes the potential drop at the gate/electrolyte interface that occurs in the case of polarizable electrodes, and therefore, all the (DC) potential arrives at the electrolyte/semiconductor interface, as shown schematically in Figure 1.5B for polarizable electrode and Figure 1.5C for non-polarizable electrodes. Therefore, non-polarisable electrodes offer simplicity in understanding the transistor electrical characteristics as one of the complexities

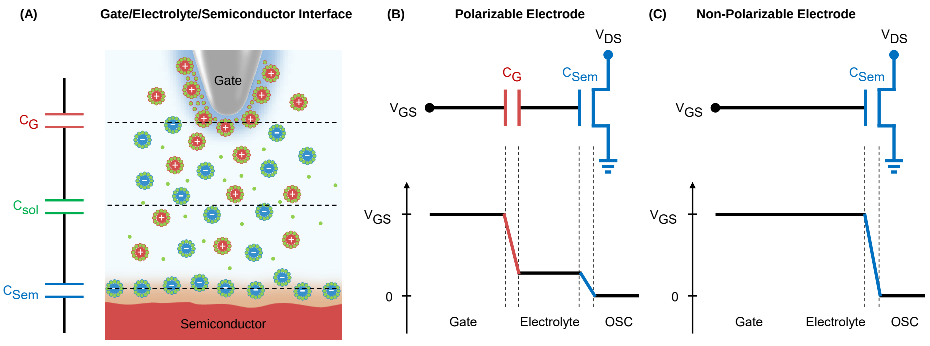

Figure 1.5: (A) Schematics of Gate/Electrolyte/Semiconductor interface showing Electrical Double Layers (EDLs) and respective capacitances, (B) Electrical schematic with a polarizable gate electrode along with diagram depicting DC gate potential division, and (C) same as (B) but for a non-polarizable gate electrode.

present in polarizable electrodes due to the involvement of gate/electrolyte capacitance that affects the voltage distribution as mentioned previously is not anymore included. The common polarizable gates are metal electrodes made of Gold (Au), Platinum (Pt), Tungsten (W) etc. The widespread non-polarisable gate used is the Ag/AgCl electrode.

The charge carrier density of the semiconductor depends solely on the effective gate voltage (the portion of the applied gate voltage) that arrives at the electrolyte/semiconductor interface, provided the (Source) electrode in contact with the semiconductor can inject charge carriers. On the other hand, the applied drain voltage sets up a potential distribution in the channel which modifies the local effective gate potential and eventually leads to spatial variability in charge carrier density along the semiconducting channel. The modelling and equation of the resulting drain current dependence on the applied gate and the drain voltage is discussed in the following section.

1.3.3. Drain Current Modelling

The drain current in EGTs is generally the output signal for many applications where one or more inputs like gate voltage, electroactive cells, biosensing recognition events etc., lead to changes in the measured drain current. The drain current is usually modelled by using the ideal current-voltage characteristics of FETs which are obtained by solving Poisson drift-diffusion and current continuity equations. For an n-type semiconductor, the drain current equation as a function of the gate (V_{GS}) and drain (V_{DS}) voltage reads[29,32]:

$$I_{\mathrm{DS}} = \frac{W}{L}\mu C' \cdot \left(V_{\mathrm{GS}} - V_{\mathrm{TH}} - \frac{V_{\mathrm{DS}}}{2}\right) V_{\mathrm{DS}} \quad \text{when} \quad V_{\mathrm{GS}} > V_{\mathrm{TH}},\ V_{\mathrm{GS}} - V_{\mathrm{DS}} \geq V_{\mathrm{TH}} \tag{1.1a}$$

$$I_{\mathrm{DS}} = \frac{W}{2L}\mu C' \cdot (V_{\mathrm{GS}} - V_{\mathrm{TH}})^2 (1 + \lambda V_{\mathrm{DS}}) \quad \text{when} \quad V_{\mathrm{GS}} > V_{\mathrm{TH}},\ V_{\mathrm{GS}} - V_{\mathrm{DS}} < V_{\mathrm{TH}} \tag{1.1b}$$

$$I_{\mathrm{DS}} = \frac{W}{L}\mu C_0 V_{ss}^2 exp\left(\frac{V_{\mathrm{GS}} - V_{\mathrm{TH}}}{V_{ss}}\right)\left(exp\left(\frac{V_{\mathrm{DS}}}{V_{ss}}\right) - 1\right) \quad \text{when} \quad V_{\mathrm{GS}} \leq V_{\mathrm{TH}},\ V_{\mathrm{GS}} - V_{\mathrm{DS}} < V_{\mathrm{TH}} \tag{1.1c}$$

where W is the channel width, L is the channel length, μ is the charge carrier mobility, C' is the equivalent gate-channel capacitance per unit area, V_{TH} is the threshold voltage, V_{ss} is the sub-threshold slope voltage (related to the sub-threshold slope S as $V_{ss} = S/ln(10)$), C_0 is the sub-threshold capacitance and λ is the channel length modulation parameter accounting for the extension of pinch-off into the channel in saturation regime. The Equation 1.1a is valid for the *Linear Regime*, Equation 1.1b for *Saturation Regime* and Equation 1.1c for the *Sub-threshold Regime*. These equations can be easily modified for p-type semiconductor by simply making the following substitutions: $V_{\mathrm{GS}} \rightarrow -V_{\mathrm{GS}}$, $V_{\mathrm{DS}} \rightarrow -V_{\mathrm{DS}}$ and $I_{\mathrm{DS}} \rightarrow -I_{\mathrm{DS}}$.

1.3.4. Current-Voltage Characteristics and Operating Regimes

The EGT works either in an accumulation mode or a depletion mode[26]. In accumulation mode, the transistor is normally in the OFF state in the absence of a gate voltage owing to the very small number of charge carriers available for conduction. On the application of a gate voltage, charges are accumulated in the semiconductor which turns ON the transistor, and hence the name *accumulation mode*. In contrast, depletion mode transistors are normally in the ON state and are intrinsically in the doped state with a large number of charge carriers available for conduction. On the application of the gate voltage, these charges are compensated and thus the semiconductor is depleted which turns OFF the transistor and hence the name *depletion mode*. In this thesis, we focused primarily on studying the accumulation mode transistors, nonetheless, the methods and results are equally transferable to depletion mode devices. The typical current-voltage transfer (I_{DS} vs V_{GS}) and output (I_{DS} vs V_{DS}) characteristics for an accumulation mode n-type and p-type semiconductor are shown in Figure 1.6.

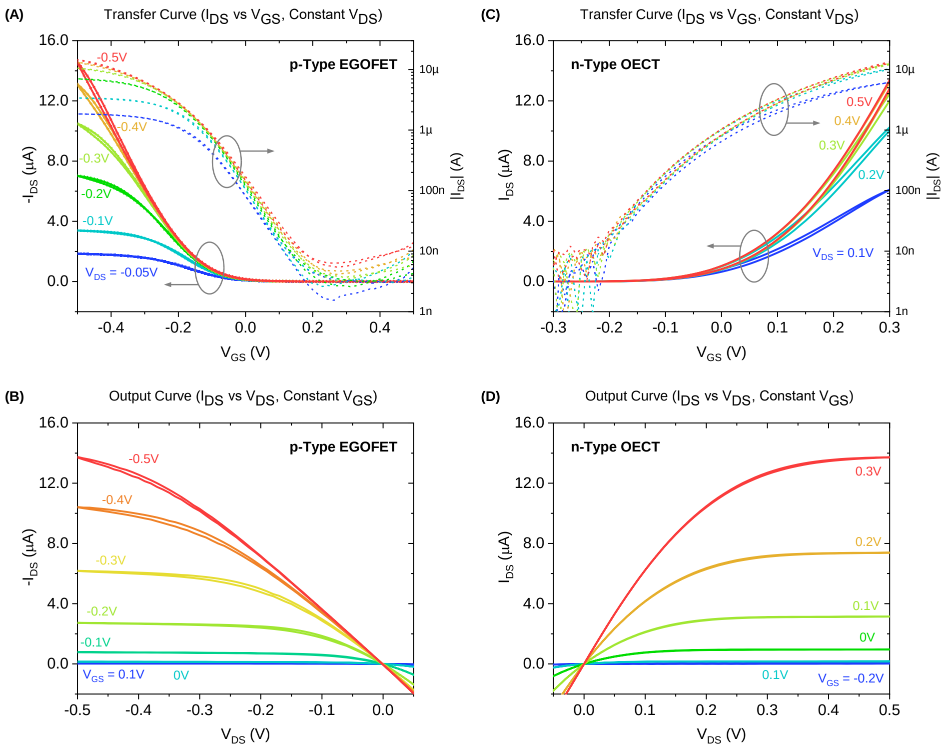

Figure 1.6: Typical (A) Transfer and (B) Output I-V characteristics of an accumulation mode p-type EGOFET. Similarly, (C) and (D) for an accumulation mode n-type OECT. EGOFET experimental parameters: Semiconductor = diF-TES-ADT:PS Blend, W/L = $19680\mu m/30\mu m$, Gate Electrode = Platinum (Pt), Electrolyte = milli-Q, Scan Rate = 10mV/100ms, Aperture Time = 20ms, Initial Delay = 100ms. OECT experimental parameters: Semiconductor = BBL Polymer, W/L = $100\mu m/10\mu m$, Gate Electrode = Gold (Au), Electrolyte = 10mM NaCl, Scan Rate = 10mV/200ms, Aperture Time = 20ms, Initial Delay = 200ms.

Different operating regimes using water analogy are depicted in Figure 1.7 along with the resulting current-voltage relationship in these regimes. Source and drain electrodes are the charge carriers (water) reservoirs, where one sources the charge carriers while the other sinks the charge carriers. These reservoirs are connected by the channel which is controlled by the gate. In the sub-threshold regime, the channel is not open, so no matter where the drain is situated (or whatever the drain voltage is applied), there is no flow of charge carriers (water) in the channel, which is represented by no current in the I_{DS} vs V_{DS} graph in Figure 1.7A. In the linear regime, shown in Figure 1.7B, the gate controls the channel, while the drain

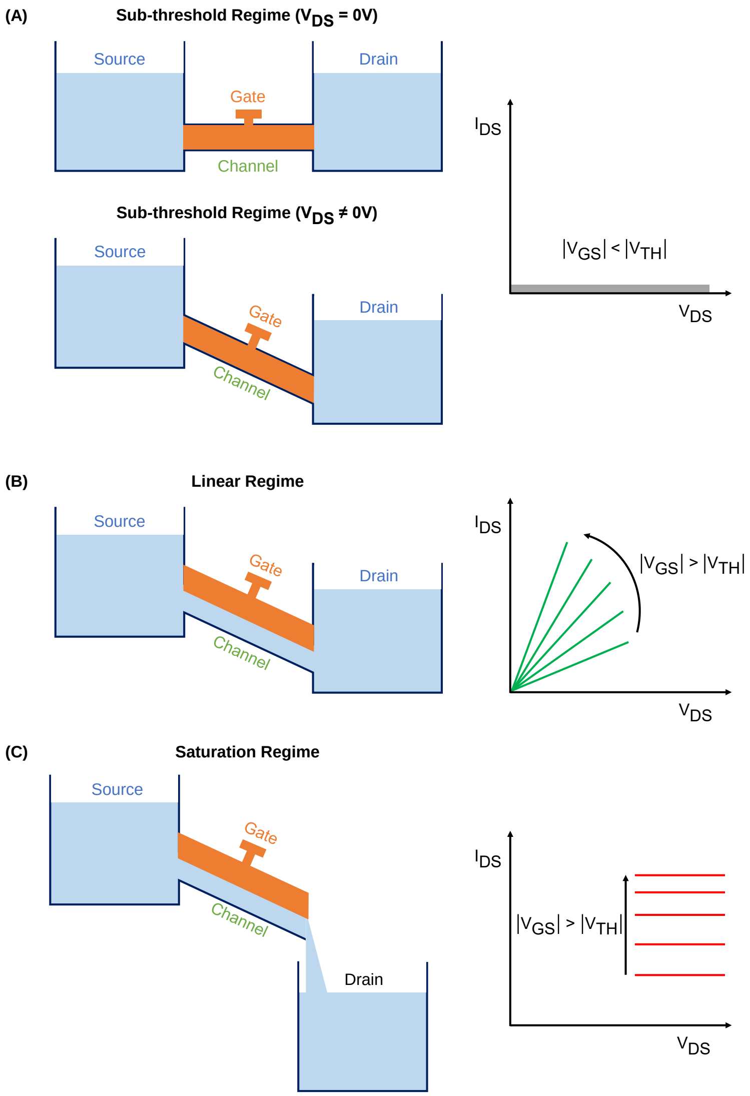

Figure 1.7: Water analogy of EGT in different operating regimes, namely (A) Subthreshold, (B) Linear, and (C) Saturation regimes. Corresponding current-voltage relationships are shown. Inspired from reference [33] (CC BY-NC-SA 4.0).

level (voltage) drives the flow. In the saturation regime, shown in Figure 1.7C, the drain is situated too far (i.e. two high drain voltage), so it doesn't affect the flow at all, as can be seen in the corresponding I_{DS} vs V_{DS} graph. Combining all the

I_{DS} vs V_{DS} graphs corresponding to different regimes together gives us the output characteristics of the device.

To assess the transistors' performance and/or benchmark the semiconducting materials, some standard figures of merit can be defined based on the parameters that go into the aforementioned drain current formula (Equation 1.1) and can be extracted from the current-voltage characteristics shown in Figure 1.6. These figures of merit are discussed in the next section.

1.3.5. Figures of Merit

The set of metrics that quantify the performance of EGTs is similar to a wide variety of other transistors, like MOSFETs, OFETs, and TFTs. However, the physicochemical properties and processes affecting these metrics are unique to each set of these transistors. The exact relation of these metrics to the physical parameters of the device is primarily absent in the case of complex devices like EGTs where the diffusive nature of the electrolytes has profound effects, and thus has introduced ambiguity in the interpretation of experiments[34]. Linking these metrics to the physical properties of the device is an ongoing research effort[32,34]. Nevertheless, some commonly used metrics and how they are extracted are mentioned below. It is essential to mention that the metrics defined below collectively determine the EGT performance; achieving exceptional attributes in one criterion is insufficient to guarantee overall exceptional performance.

Charge Carrier Mobility (μ)

Charge carrier mobility quantifies how easily and quickly the free charge carriers move through the material in response to an applied electric field. It is typically represented by the symbol μ and defined as the average drift velocity ($cm\,s^{-1}$) of the mobile charge carriers per unit applied electric field ($V\ cm^{-1}$), and thus bearing the unit of square centimetres per volt-second, i.e., $cm^2\ V^{-1}\ s^{-1}$. Charge carrier mobility is supposedly a characteristic intrinsic parameter of the semiconducting material; however, it is strongly influenced by extrinsic factors like material processing, deposition conditions, and environmental parameters (pressure and temperature) that dictate the molecular and supramolecular structures of the organic semiconductor in thin films. In addition, it is also influenced by the

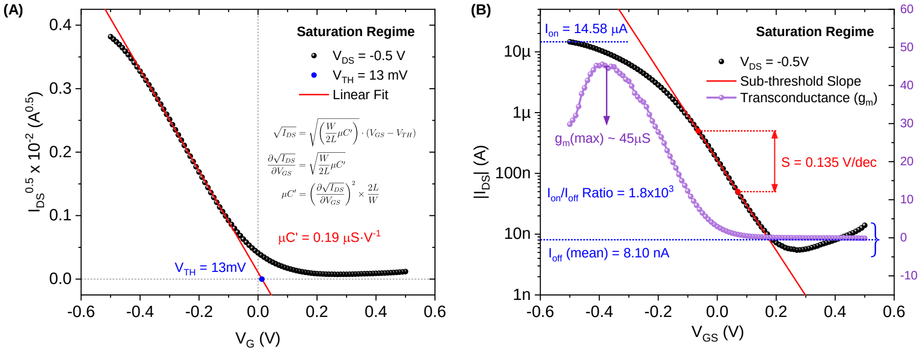

Figure 1.8: EGT parameter extraction process from the transfer curve in saturation regime. (A) showing extraction of threshold voltage and $\mu C'$ product from the plot of $\sqrt{I_{DS}}$ vs V_{GS} following the Equation 1.1b with $\lambda = 0$. (B) showing extraction of sub-threshold slope (S) and on-off drain current ratio (I_{on}/I_{off}) from the transfer curve. The data is taken from Figure 1.6 corresponding to a p-type EGOFET.

electric field strength and the charge carrier density[35–37]. Also, a single value for a crystalline or polycrystalline anisotropic material is insufficient. It is essential to consider the influence of anisotropy and crystal orientation on the mobility value measured with the EGT structure[38–40].

Attaining high charge carrier mobility is a goal of many research efforts as it directly relates to the transit frequency or switching speed of the moderate-channel-length transistors[41]. For short channel lengths, transit frequency is loosely related to charge carrier mobility and instead becomes heavily dependent on contact resistance[42]. Nonetheless, mobility is an important material property to measure and optimize. Charge carrier mobility is commonly extracted from the device's transfer characteristics (I_{DS} vs V_{GS}) in the linear or saturation regime. Figure 1.8A shows the mobility extraction in the saturation regime for the p-type EGOFET from the transfer characteristics shown earlier in Figure 1.6A (if we use the nominal value of capacitance per unit area $C' = 5.3\mu F/cm^2$ for this transistor[30], then we get $\mu = 0.037 cm^2 V^{-1} s^{-1}$).

It is important to mention that many reported mobility values in the literature are irreproducible and meaningless, primarily due to the lack of standard benchmarking procedures, uncontrolled testing conditions, unreliable data analysis, and overlooked device aspects[28,29]. Some efforts towards standardized approaches are documented in reference [43], [44], and [45], which mainly prescribes reporting standards and parameter extraction procedures following a conservative approach such as fitting the non-steep part in the case of non-ideal transfer characteristics for mobility extraction to avoid overestimation.

Transconductance (g_m)

The transistors have an intrinsic amplification character where a small potential change at the gate electrode translates to significant changes in the drain current. The transconductance (g_m) quantifies the efficiency of this modulation underpinning signal transduction and is a signature of ionic-electronic coupling in EGTs[46]. The transconductance is defined as the derivative/slope of the device's transfer characteristics (I_DS vs V_GS), i.e., $g_\mathrm{m} = dI_\mathrm{DS}/dV_\mathrm{DS}$. Figure 1.8B (violet symbols) shows the transconductance curve in the saturation regime for the p-type EGOFET derived from the transfer characteristics shown earlier in Figure 1.6A. As expected, it depends on the device operating point besides the properties of the interfaces and the presence of bio-layers in the case of biosensing applications. In EGOFETs (discussed in the subsection 1.4.1), it depends on the channel length and width. Although channel thickness does not directly affect transconductance in EGOFETs, as the ionic-electronic coupling is limited to the interface, it can affect the amount of injected charge carriers, and so does the drain current and, ultimately, transconductance. On the other hand, in OECTs (discussed in the subsection 1.4.2), the conduction is not limited to the interface as the ionic-electronic coupling extends into the bulk of the semiconductor and thus directly affects the transconductance[47]. Therefore, the transconductance is sometimes normalized with the channel's geometric parameters or applied drain voltage for the material comparison independent of the measurement conditions, as the case may be.

Threshold Voltage (V_TH)

The threshold voltage is a phenomenological voltage parameter which separates the subthreshold regime from the linear regime. For gate voltages applied ($|V_\mathrm{GS}|$) above the threshold voltage ($|V_\mathrm{TH}|$), there are enough charge carriers in the semiconductor which would lead to appreciable drain current under applied drain voltages and will turn ON the accumulation mode device. The threshold voltage accounts for the presence of fixed charges, the difference in the gate electrode and organic semiconductor workfunctions, the in-efficient capacitive coupling of the gate with the channel, and other physiochemical processes. It can be determined from the transfer characteristics in the linear or saturation regime. Figure 1.8A shows the extraction of threshold voltage in the saturation regime from the plot of $\sqrt{I_{DS}}$ vs V_{GS} following the Equation 1.1b with $\lambda = 0$ assumption.

ON-to-OFF Drain Current Ratio (I_{on}/I_{off})

The ON-to-Off drain current ratio as the name suggests is the ratio between the drain current in the ON-state and the OFF-state at the specified drain voltage. It can be determined from the transfer curve as shown in Figure 1.8B. Maximizing this ratio is desirable, especially for switching applications, and tells us about the level of control the gate voltage exercises.

Sub-threshold Swing (S)

The drain current has an exponential dependence on V_{GS} for $|V_{\mathrm{GS}}| < |V_{\mathrm{TH}}|$, as shown in Figure 1.8B by the linear region on a semilog scale. A quantity known as sub-threshold swing (S) can be defined to capture the steepness of the transfer curve, which is expressed as $S = dV_{\mathrm{GS}}/d(logI_{\mathrm{DS}})$[48]. Sub-threshold swing (S) is the gate voltage required to change the drain current (I_{DS}) by one decade in the sub-threshold region. It can be determined from the transfer curve represented on a semilog scale in both linear and saturation regimes, while also reporting the device geometry. Figure 1.8B shows the extraction of sub-threshold swing, giving $S = 135mV/dec$. As apparent, the lower the gate voltage required to cause a decade change in drain current, the steeper the resulting transfer curve. How steep can the transfer curve be or in other words, what is the minimum theoretical limit of sub-threshold swing? The minimum theoretical limit of sub-threshold swing can be estimated from the thermal voltage (KT/q), which at room temperature results in a minimum sub-threshold swing of $S = ln(10)KT/q \approx 60mV/dec$[49].

Gate and Channel Capacitances (C')

The higher the gate-electrolyte and channel-electrolyte equivalent capacitance per unit area ($C'_{eq} = ({C_G}^{-1} + {C_{Sem}}^{-1})^{-1}{A_{Sem}}^{-1}$, where C_G is the total gate capacitance, C_{Sem} is the total semiconductor capacitance, and A_{Sem} is the semiconductor area[29]), the lower the gate voltage required to reach a specific charge carrier density state of the semiconductor ($Q_{Sem} = C'_{eq} V_{GS} A_{Sem}$). In the case of an ideal non-polarizable gate electrode, $C_G = 0$ as there is no charge separation at the gate electrolyte interface. In the case of EGOFETs(discussed in the subsection 1.4.1), $C_{Sem} = C_{EDL} A_{Sem}$, where C_{EDL} is the electrical double layer (EDL) capacitance per unit area of the semiconductor-electrolyte interface[29]. These capacitances are generally obtained through electrochemical impedance spectroscopy (EIS) analysis and displacement current measurements (DCM)[30].

Volumetric Capacitance (C^*)

In the case of OECTs (discussed in the subsection 1.4.2), ions penetrate into the bulk of the semiconductor, leading to a variation of the volumetric capacitance of the semiconductor. So, the C_{Sem} is modified to $C_{Sem} = C^* A_{Sem} h_{sem}$, where C^* is the volumetric capacitance of the semiconductor per unit volume and h_{sem} is the semiconductor thickness. C^* can be viewed as an effective electrical double layer capacitance distributed over thickness (3D EDL) with relation $C^* = C_{EDL}/h_{sem}$ for unified treatment[29] and can be helpful in understanding the measurements (as we will see in Chapter 4). As apparent, the semiconductor capacitance scales with the thickness of the channel, which translates to the scaling of transconductance as well[25].

Product (μC^*)

In the case of OECTs (discussed in the subsection 1.4.2), the injection of ions within the semiconducting structure impart them with high charge storage capacity which is defined in terms of volumetric capacitance (C^*) as mentioned earlier. However, in addition to requirements for efficient charge transport and facile reversible ion injection properties, materials for OECTs must also confront dynamic structural disorders and morphological changes induced by ion injection for stable operation. The ion injection can lead to structural rearrangements and disorder, leading to localized variations in energy levels and hindering charge transport pathways. The disorder can result in increased scattering of charge carriers, reducing their mobility as they traverse through the material. Therefore, when considering the materials for OECTs and accessing figures of merits, it is essential to account for the impact of ion injection on the structural integrity and long-term stability of the material. Optimized electronic and ionic transport can be achieved by understanding and mitigating the effects of structural disorder on charge carrier mobility, ultimately leading to the development of more reliable and efficient devices. Therefore, the product of charge carrier mobility and volumetric capacitance (μC^*) suits better as the figure of merit to evaluate the performance of the material and device and is now often used as a benchmark to guide material design and processing conditions[50]. The μC^* can be easily extracted from the measurement of the transfer curve by taking the derivative and normalizing it with the channel geometry and effective gate voltage ($V_{\mathrm{GS}} - V_{\mathrm{TH}}$) as per Equation 1.1 with $C' = C^* h_{sem}$, while also reporting the drain voltage or regime of operation (linear or saturation). Generally, a single number corresponding to the peak transconductance value is reported. However, measuring devices with different geometries ($W h_{sem}/L$) and using the derivative of Equation 1.1 with $C' = C^* h_{sem}$ to fit the measurements is recommended for rigorous examination.

1.4. EGT Classification

The extensive library of materials used in EGTs provides them with diverse electrical and mechanical properties, offering a vast design space for exploration. This diversity can be broadly classified based on the semiconductor's ionic permeability, resulting in two EGT varieties, namely Electrolyte-Gate Organic Field-Effect Transistors (EGOFETs) based on ion-impermeable semiconductors and Organic Electrochemical Transistors (OECTs) for ion-permeable semiconductor[29]. The note-worthy operational distinction is that EGOFET mainly uses the electronic transport characteristics of the semiconductor, whereas OECT relies on the semiconductor's mixed ionic and electronic transport characteristics. The mode of operation directly impacts the performance of the EGTs. EGOFETs are faster but have lower Transconductance due to only interfacial ionic-electronic coupling, whereas OECTs are slower but have higher Transconductance owing to bulk ionic-electronic coupling giving high charge storage capacity[26].

In the following sections, we dwell more into the EGOFETs and OECTs regarding their operating mechanism and highlight some specific semiconducting materials used. We also highlight the applications and some notable proof-of-concept technologies created based on them.

1.4.1. Electrolyte-Gated Organic Field-Effect Transistor (EGOFET)

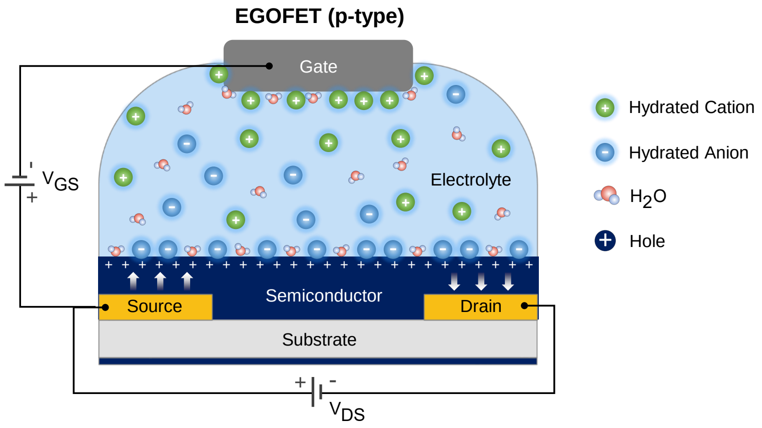

Figure 1.9: Schematic of p-type Electrolyte-Gated Organic Field-Effect Transistor (EGOFET) illustrating the ionic distribution within the electrolyte under application of gate bias voltage above the threshold.

In EGOFET, the applied gate potential controls the field strength of the Electrical Double Layer (EDL) at the semiconductor/electrolyte interface that causes the source electrode to inject free charge carriers into the semiconductor which then accumulates at the semiconductor/electrolyte interface forming a conduction channel, as shown in Figure 1.9. The accumulated charges lead to elevated interfacial conductivity. Upon application of a drain voltage, the injected charge carriers travel from the source electrode to the semiconducting channel at the interface and then to the drain electrode (the path is denoted by white arrows in Figure 1.9) and set up a drain current in the device.

EGOFETs demand superior electronic charge transport properties of the semiconducting material, which is favoured towards well-ordered crystalline thin-film materials. The assembly of the semiconducting material to a well-ordered thin film can be facilitated through rational modification of its molecular structure. Pentacene (Figure 1.2C) and its analogue anthradithiophene (ADT) (Figure 1.10A) have emerged as common building blocks whose aromatic cores are strategically manipulated to control their packing arrangements in thin films[3]. Figure 1.10 shows successive modifications of ADT (A) chemical structure to

TES-ADT (B) and diF-TES-ADT (C) chemical structures. The introduction of $-C \equiv C - Si(C_2H_5)_3$ improves processability and facilitates efficient π-stacking of aromatic cores in a thin film, which leads to higher charge carrier mobilities[3]. The addition of peripheral F-atom enables short-range non-covalent interactions further improving charge carrier mobility[3]; at the same time, on PFBT-treated source-drain electrodes, it enables F-F interactions between the molecule and PFBT that favours the growth of <001> crystallites so the π-stacking axis is along the in-plane direction of the channel and thus allows control over the orientation of molecules in the transistor channel for superior device transport characteristics[51].

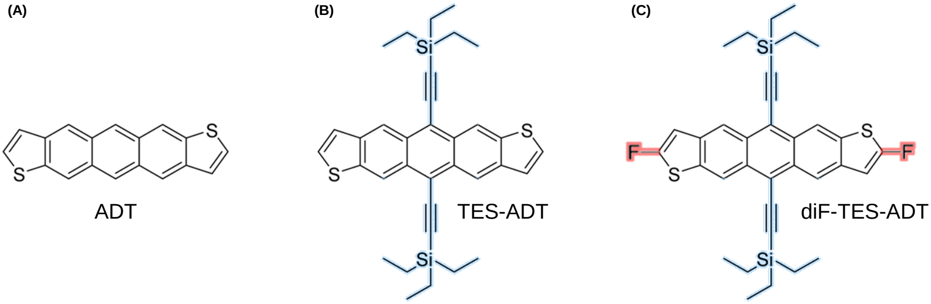

Figure 1.10: Chemical structure of (A) anthradithiophene (ADT), (B) 5,11-Bis(triethylsilylethynyl)anthradithiophene (TES-ADT) and (C) 2,8-Difluoro-5,11-bis(triethylsilylethynyl)anthradithiophene (diF-TES-ADT). Different modifications (blue and red) are highlighted that lead to improved processibility and efficient assembly of molecules in a thin film for superior charge transport properties.

EGOFET applications

EGOFETs provide the perfect platform for sensing applications. The modulation in the effective gate potential that controls the transistor output drain current can be triggered by any process or phenomenon that changes the electrical characteristics (fixed charges[52–54], interfacial capacitance[55–57], work function[58,59], broadly the potential drop) of the gate-electrolyte or semiconductor-electrolyte interfaces; it can be antigen/antibody interactions and even cellular electrical or biomolecular activities[60,61].

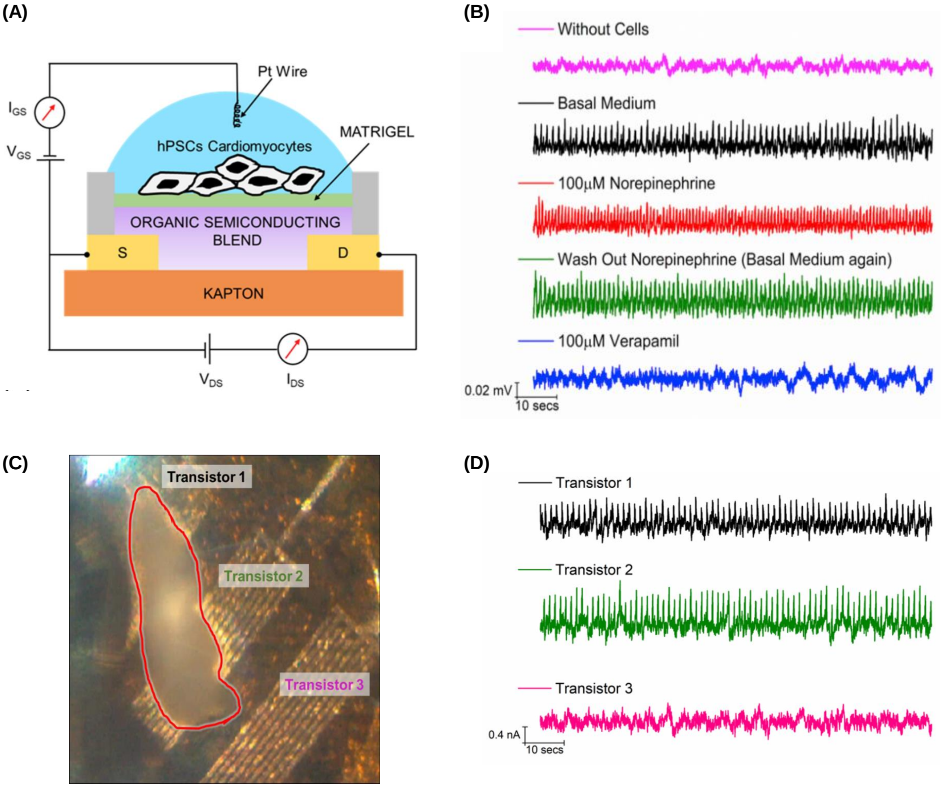

Figure 1.11: (A) EGOFET interfaced with human pluripotent stem cell-derived cardiomyocyte cells (hPSCs-CMs), (B) Drain current recordings under different conditions using the device schematically illustrated in (A), (C) Optical image highlighting a cluster of cells with three transistors, and (D) Drain current recording from three transistors shown in the optical image in (C), depicting that only the transistor locally interfaced with cells shows drain current spikes. Adapted with permission from reference [61]. Copyright 2020 Elsevier.

Therefore, EGOFETs can also be used for electrophysiological recordings. In this case, the variations in the cell membrane potential modifies the "effective" gate voltage applied to the transistor and result in a variation of the drain current. One example of an EGOFET application of this type is highlighted in Figure 1.11, where Kyndiah et al.[61] showed the bioelectronic recording of human pluripotent stem cell-derived cardiomyocyte cells (hPSCs-CMs) interfaced with the transistor channel at the semiconductor/electrolyte interface as shown in Figure 1.11A. They demonstrated the usability of this platform for screening pharmaceutical drugs, such as Norepinephrine and Verapamil, for cytotoxicity tests as shown in Figure 1.11B. Interestingly, the cells are tightly and locally coupled with the transistor channel, as only the cells which sit on top of the transistor channel induce electrical spikes due to cell electrical activity in the drain current as shown in Figure 1.11(C-D).

Recent reviews provide excellent comprehensive coverage of EGOFETs potential applications in biosensing[29,62,63], and bio-interfacing[64,65].

1.4.2. Organic Electrochemical Transistor (OECT)

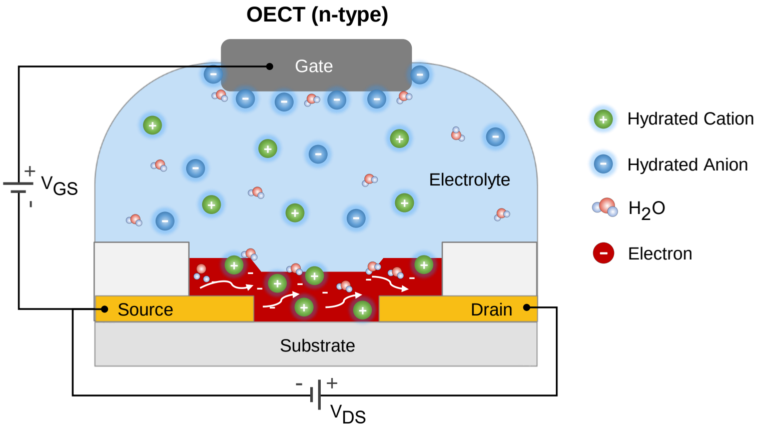

Figure 1.12: Schematic of n-type Organic Electrochemical Transistor (OECT) illustrating the ionic distribution within the electrolyte and semiconductor under application of gate bias voltage above the threshold.

In OECT, the applied gate potential drifts the ionic charges of the electrolyte into the bulk of the semiconductor and changes its redox state, which drives the injection of free charge carriers from the source electrodes into the semiconductor resulting in the modulation of its bulk conductivity, as shown schematically in Figure 1.12. Materials for OECT are thus generally soft, readily allowing ion uptake, and are often polymeric materials supporting both ionic and electronic conduction. These materials can either be homogeneous, where a single component carries both ionic and electronic charges, or intrinsically heterogeneous, such as block copolymers or blends consisting of separate components for ionic and electronic conduction[27]. A popular class is a polymer with conjugated backbone and hydrophilic side chains[66]. The ion uptake is controlled and optimized through side-chain engineering that allows scope for efficient ionic-electronic coupling with electronic charge carriers in the polymer backbone. The interplay between ionic and electronic charges is the basis for diverse applications of OECT materials ranging from energy storage devices[67] to neuromorphic artificial synapses[68]. Owing to this mixed-conduction property, OECT materials are also known as Organic Mixed Ionic-Electronic Conductors (OMIECs) in literature[27].

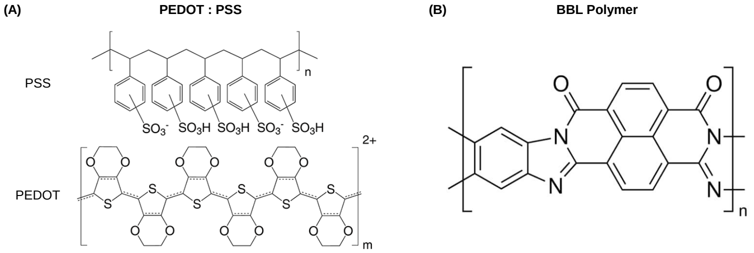

Figure 1.13: The chemical structure of state-of-the-art (A) p-type (PEDOT:PSS) and (B) n-type (BBL) OECT materials.

OMIECs greatly benefited from advancements in quantum and synthetic chemistry, which enabled the establishment of design rules and the synthesis of a wide range of molecular structures with tailored multifunctional properties[3,69]. One of the most popular materials for OECT and widely researched is poly(3,4-ethylenedioxythiophene) polystyrene sulfonate (PEDOT:PSS) due to its efficient electronic and ionic transport characteristics along with stable operation in aqueous conditions, processability through various methods, and easy commercial availability. It is a p-type material and a polymer blend in which PEDOT is intrinsically doped by PSS, which makes OECT based on PEDOT:PSS work in depletion mode. However, some chemical strategy exists that de-dopes PEDOT:PSS to make it work in accumulation mode (also called enhancement mode)[70]. The chemical structure of PEDOT:PSS is shown in Figure 1.13A. In the case of n-type OECT materials, poly(benzimidazobenzophenanthroline) (BBL) has shown impressive performances very close to that reported for p-type devices and works in accumulation mode. BBL is a homogeneous π-conjugated redox polymer where ionic and electronic processes are not phase separated, in contrast to the case of PEDOT:PSS. The chemical structure of BBL is shown in Figure 1.13B.

OECT applications

The mixed ionic-electronic conduction of OECT materials and the ability to tailor these characteristics with synthetic chemistry enables multiple applications. The OECT provides the means to leverage these functionalities, and at the same time, the transistor topology gives amplifying character. Therefore, OECTs have garnered considerable potential interest as circuit components[71–73], neuromorphic devices[11,74], sensing elements[75,76], and stimulation[77] segments in bioelectronics. OECT materials are a persistent research topic in academia and industries, and many impressive demonstrations of their potential applications already exist.

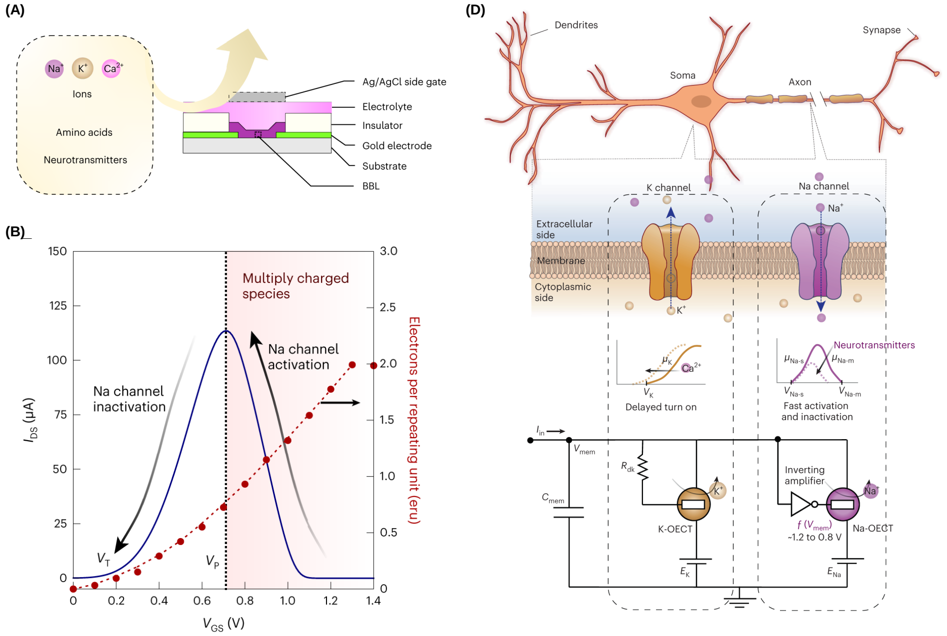

Figure 1.14: (A) OECT device structure employed to show conductance-based organic electrochemical neuron (c-OECN), (B) Antiambipolarity behaviour of the OECT used to mimic the activation and inactivation of sodium channels in a neuron, and (C) Illustrating the analogy between the biological neuron with sodium and potassium channels and the c-OECN circuit. Adapted from reference [68]. (CC BY).

One example of OECT applications is highlighted in Figure 1.14, where Harikesh et al.[68] used the OECT devices based on BBL polymer (A), which exhibits anti-ambipolar behaviour (B) to mimic the activation and inactivation of sodium channels in a biological neuron (C), and thus reporting what they named as "a biorealistic conductance-based organic electrochemical neuron (c-OECN)".

For comprehensive coverage of OECT applications, refer to the recent reviews in references [78], [64], [79], [80], [63], [29], and [65].

1.5. Operando Characterization

The EGT materials, devices and architectures introduced in the previous sections have the potential for diverse applications as mentioned earlier; however, they are still in their infancy. Many challenges must be overcome in dealing with stability, reliability and reproducibility. The major roadblock is that several fundamental aspects, especially at the nanoscale, are poorly understood, primarily owing to a lack of experimental characterization techniques explicitly developed to probe the relevant physics of these materials and devices. The dynamic and multimodal characteristics of these materials in operating devices need to be understood, which demands the development of operando characterization techniques, as discussed in what follows.

Organic bioelectronics is an inter- and multidisciplinary field, drawing on expertise from materials science, chemistry, physics, biology, and engineering. A myriad of research efforts is directed toward improving organic semiconductors' performance, stability, and efficiency, while also developing new materials and device architectures to advance the field further. However, the existing techniques and methods for assessing the multifunctional characteristics of organic devices during operation are limited and mostly not adequate enough to reveal the fundamental operating mechanism happening at the nanoscale in all its glory.

Establishing multiscale structure-property-function relationships in such systems is crucial in order to effectively address the requirements of various applications with a high level of reliability. Such relationships untangle how the local structural characteristics of a material or system influence its local properties and how these properties ultimately affect the global functionality of a device. These relationships will simultaneously address a range of fields, from materials science to engineering, and put them into consideration at the same plateau. The development of operando techniques could facilitate establishing these relationships.

Some recent reviews[27,81,82] have also put forth the need for developing advanced operando characterization methods for investigating organic materials and devices during operation from a multimodal perspective and aid in the fundamental understanding. Such operando techniques will set aside the traditional trial-and-error approaches in favour of more rational and scientific approaches to optimize materials and devices.

However, there are a few requirements that such operando techniques must meet in order to directly translates the result into design rules. Such requirements and the challenges in conforming to them are discussed in the following sections.

1.5.1. Requirements for Operando Techniques

The operando techniques should provide insights into various physical and chemical changes in the material during operation, which could be time and/or voltage-dependent. By studying phenomena under realistic conditions, operando techniques enable a more accurate understanding of the underlying mechanisms and dynamics than ex-situ techniques. It is important to note that "in situ" techniques are not generally "in operando" techniques, whereas "in operando" techniques are "in situ" techniques[81]. The term "in situ" means "on the site", not necessarily under operating conditions[83]. The in-situ methods are generally employed to probe the formation and assembly of the semiconducting materials into thin films to understand the film microstructure formation and ultimately to optimize processing conditions to achieve desired assembly. In this thesis, we focus on the operando techniques exclusively.

Operando techniques should adhere to realistic operating conditions; therefore, the requirements are set accordingly. The typical requirements become evident upon a judicious evaluation based on the possible parameters that can affect the response of the material or device. A recent assessment of operando characterization techniques emphasized the importance of following set requirements and suggested being cautious while extrapolating the results to different scenarios[81]. A true operando technique is one that is performed in the same geometries and experimental configurations used in the applications. Adhering to the geometrical dimensions and structural parameters is crucial, as highlighted in Figure 1.15, since they determine the magnitude of the electrical fields in the device's 3D space, directly impacting the local processes and functional relationships. At the same

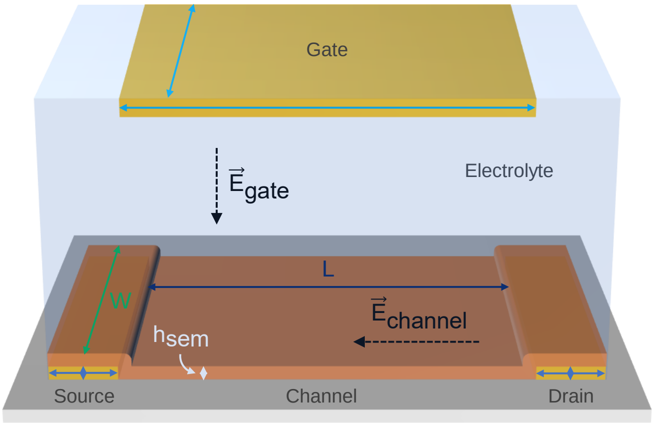

Figure 1.15: The geometrical dimensions and structural parameters that influence the EGT performance are highlighted: Channel length (L), Channel thickness (h_{sem}), Channel width (W), contact metal electrodes dimensions and type, gate electrode dimensions and type, substrate type, gating electrolyte type and ionic strength.

time, the technique should be operable in aqueous electrolytes and able to probe the semiconductor interface where the physical and chemical changes generally happen.

In the case of time-resolved measurements, it is necessary to ensure that the temporal resolution is sufficiently fast to decipher the underlying process accurately. According to the Nyquist-Shannon sampling theorem, the temporal resolution must be at least twice as fast as the characteristic time scale of the process being studied. For instance, if the process has a characteristic time scale of 1 second, then the operando technique must have a resolution of at least 0.5 seconds or better to resolve it. However, for practical purposes, it is recommended to use a temporal resolution ten times faster than the characteristic time. In the above example, a temporal resolution of 0.1 seconds or better would be appropriate to reliably resolve a process with a characteristic timescale of 1 second. The slowest process in the device is the rate-limiting step, so the bandwidth need to be enough to capture the whole process. Generally, the processes mediated by ions are slower than those mediated by electronic charges. A simple step or impulse excitation can be performed to extract the device's characteristic time scale. Knowledge of the time scales involved is crucial in determining the most suitable measurement technique.

1.5.2. Challenges in Operando Characterization

As previously stated, the optimal experimental design for the operando technique should accommodate the application-relevant device geometry and operating conditions. However, meeting these seemingly straightforward criteria presents significant technological and fundamental challenges when dealing with EGTs, primarily due to complications arising from the presence of the electrolyte. For example, Kelvin Probe Force Microscopy (KPFM) is a standard method for measuring local electrical potential in solid-state Organic FETs or TFTs in operando that enables extracting relevant information like contact resistance, charge carrier mobility, charge trapping, grain boundaries and other geometric effects[84]. However, the fundamental principles governing the conventional KPFM are readily violated in aqueous electrolytes due to DC (and low-frequency AC) bias-induced charge screening dynamics and electrochemical processes that prohibit direct local potential mapping[85]. Utilizing high-frequency (MHz) voltages can avoid or limit the charge screening dynamic, but it necessitates the use of high resonance frequency cantilevers, which is currently not possible with the commercially available standard cantilevers in a liquid environment[86].

Additionally, some techniques such as optical moving front[87,88], voltage probes[89], and scanning electrochemical microscopy[90] have limited resolution and therefore require devices considerably larger than those typically used in applications, and thus pose challenges in translating the finding directly to design rules. Also, some techniques such as NMR[91] and grazing incidence X-ray scattering[92] demand specialized sample holders to accommodate all the connections and electrodes due to instrument-specific spatial and technical requirements.

Nevertheless, some efforts and progress have been made to remove or get around these limitations for in operando characterization of EGTs. In the next section, we review the operando techniques implemented to gain insights into the operation of EGT devices. In this context, we primarily focus on operando in-liquid scanning probe techniques due to their inherent capability to directly investigate micro/nanoscale features and allow forming multiscale correlations. At the same time, this aligns with the primary research objective of the current thesis. Some of the implementations reviewed employ a simplified two-electrode architecture, where one electrode is coated with a thin-film semiconductor and another serves as the gate electrode, as an alternative to the more complex transistor architecture. Nevertheless, they provide valuable insight into EGT materials.

1.6. Operando Scanning Probe Techniques for EGTs

Scanning probe techniques are powerful nanotechnology tools to study and manipulate surfaces at the atomic and molecular levels. Scanning probe techniques rely on the interaction between a sharp probe or tip and the sample surface to obtain/modify the local properties of the sample. The type of tip-sample interaction determines the characteristics of the probed property; it can be morphological, compositional, electrical, mechanical, and various other properties. While these techniques are widely used in dry environments, their application in liquid environments presents unique challenges and opportunities, especially in studying electrical properties.

The following section presents scanning probe implementations used in the literature to understand organic semiconductors' behaviours during operation interfaced with liquid environments.

1.6.1. Electrochemical Strain Microscopy (ESM)

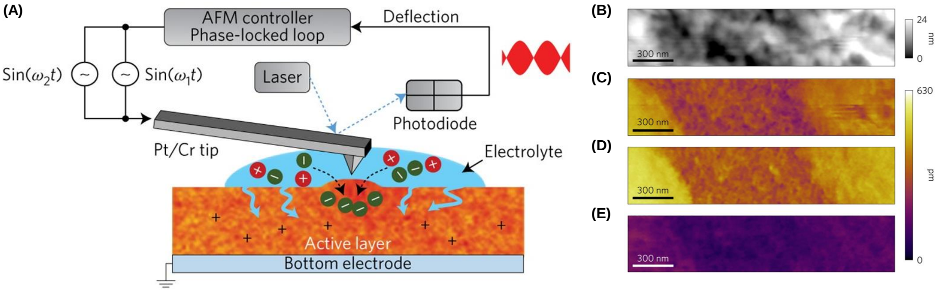

Figure 1.16: Electrochemical Strain Microscopy (ESM). (A) Schematic of operando electrochemical strain microscopy (ESM) with dual-amplitude resonant frequency tracking (DART) mode, (B) Topography of the P3HT film in 20mM KCl solution, and ESM amplitude images at gate voltages of (C) 0V, (D) -0.35V, and (E) +0.35V. The gate voltage is applied as an additional DC bias offset to the tip drive bias shown in (A). Adapted with permission from reference [93]. Copyright 2017 Springer Nature.

Electrochemical strain microscopy (ESM)[94] has been used to probe the ion transport in conjugated polymer thin films in aqueous electrolytes by monitoring the local electrochemical strain exerted on a conductive AFM probe in contact with the thin film upon swelling/deswelling of the polymer due to induced oxidation/reduction (concurrent with ion injection/expulsion) in response to applied AC potential between the tip and the sample[93,95–97] (see Figure 1.16A). The strain on the AFM tip is monitored at the contact resonance of the tip-sample interface in dual-amplitude resonant frequency tracking (DART) mode. The applied AC frequency is generally faster than the time required for full doping of the film, so the resulting swelling causing strain on the AFM tip is smaller. In addition, a DC offset voltage is applied which acts as the gate voltage to control the doped state of the polymer and probe voltage-dependent behaviour using dynamic AC strain in that doped state. So, the expression of tip voltage applied in ESM is

$$[V_{Tip}]_{ESM} = V_{DC} + A_1 sin(\omega_1 t) + A_2 sin(\omega_2 t) \tag{1.2}$$

Giridharagopal et al. first demonstrated the capability of ESM on conjugated polymer poly(3-hexylthiophene) (P3HT) thin films (see topography in Figure 1.16B) to directly probe ion transport as a function of applied DC offset voltages (gate bias), as shown in Figure 1.16(C-E). The data indicates that the swelling happens only in the doped state (Figure 1.16C and Figure 1.16D), while in the de-doped state, significantly less swelling is observed (Figure 1.16E). They also investigated local variations in ion transport, which revealed heterogeneous swelling anti-correlated with the local stiffness, i.e. softer regions are readily able to uptake ions exhibiting electrochemical operation mode (OECT-type), while stiffer regions inhibit ion uptake and thus exhibit field-effect operation mode (EGOFET-type).

In a nutshell, ESM represents a powerful technique to probe the nanoscale variations in ion uptake in correlation with local mechanical properties and thus provide a direct test of structure-function relationships in biased polymer thin films. Of course, it relies on the material's capacity to change its strain related to ion uptake, linked to OECTs rather than to EGOFETs.

1.6.2. Bimodal Atomic Force Microscopy (Bimodal AFM)

Bimodal AFM is a fast nanomechanical mapping method that can probe the elastic modulus of various biomaterials and polymers such as membrane proteins[99],

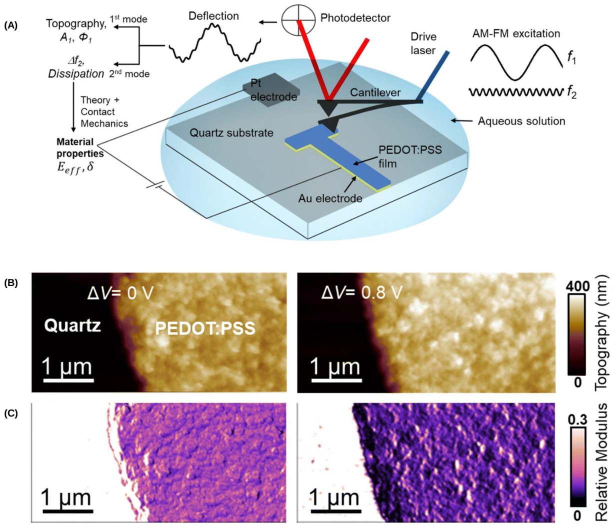

Figure 1.17: Bimodal Atomic Force Microscopy (Bimodal AFM). (A) Schematic of the Biomodal AFM implementation for operando nanomechanical characterization of the organic semiconductor. (B) and (C) shows simultaneously acquired Topographic and Young's modulus maps during doping (0V) and de-doping (0.8V) of PEDOT:PSS film in 50mM KCl solution, respectively. Adapted from reference [98]. (CC BY-NC 3.0).

collagen structures[100], supported lipid bilayers[101], and conducting polymers[98,102] in the liquid media. In Bimodal AFM, the first two eigenmodes of the cantilever are simultaneously excited, where the first mode controls the tip-sample distance in amplitude modulation (AM) feedback giving the apparent topographic image of the sample, and the second mode works in frequency modulation (FM) to track the shift in its resonant frequency. The both modes characteristics are used to quantify Young's modulus[98,102], as shown in Figure 1.17A. This configuration is also called Bimodal AM-FM.

Benaglia et al.[98] recently used Bimodal AFM to map the nanomechanical and structural properties of PEDOT:PSS thin films under air and electrolyte environments. They investigated the modulation of mechanical properties of the polymer in repeated doping de-doping cycles controlled by the external platinum gate electrode. Since, PEDOT:PSS works in depletion mode as mentioned earlier in subsection 1.4.2, under de-doping potentials, cations penetrate the semiconductor and compensate the sulfonate anions of PSS which depletes the PEDOT and thereby decreases the hole charge carrier concentration. The cation penetration into the polymer causes morphological and mechanical changes, making it softer than the doped state, as probed by the Bimodal AFM in Figure 1.17B. The subsequent doping de-doping cycles soften the polymer more and more which eventually saturated in its response indicating irreversible changes in the mechanical properties during prolonged operation due to persistent hydration of the polymer.

Like electrochemical strain microscopy (ESM), bimodal AFM provides valuable information about the dynamic changes in the mechanical properties of the organic semiconductor under applied biases, thus is relevant in the case of OECTs rather than EGOFETs.

1.6.3. Scanning Electrochemical Microscopy (SECM)

Scanning electrochemical microscopy (SECM) is a well-known electroanalytical technique used in a wide range of fields ranging from corrosion chemistry[103] to biological phenomena[104]. SECM makes use of a precisely positioned microelectrode to probe the local electrochemical properties and redox state by monitoring the fluxes of redox species by recording the current or potential response at the surface of the material immersed in an aqueous electrolyte environment[105–112].

Focusing on the implementation of SECM on transistor architecture, Mariani et al.[90] used SECM to map the local electrochemical potentials in millimetre-sized operating OECTs based on PEDOT:PSS in the aqueous electrolyte, as shown in Figure 1.18(A-B). The Pt microelectrode forms the ohmic contact with the PEDOT domains on the channel surface and allows measuring electrochemical potential along the channel with a high-impedance differential amplifier against the quasi-reference electrode (QRE) (see Figure 1.18A). They observed a direct linear relationship between the measured electrochemical potential and the doping state of the polymer which enabled the extraction of OECT charge transport parameters such as contact resistance, charge carrier concentration, and mobility, as shown in Figure 1.18(C-D).

SECM method provides valuable information that is not readily available by other scanning probe techniques, such as KPFM which cannot operate in an aqueous electrolyte environment due to the presence of charge screening dynamics. However, there are still some shortcomings of SECM such as the size of the micrometric SECM probe limiting the resolution and the device physics that can be explored,

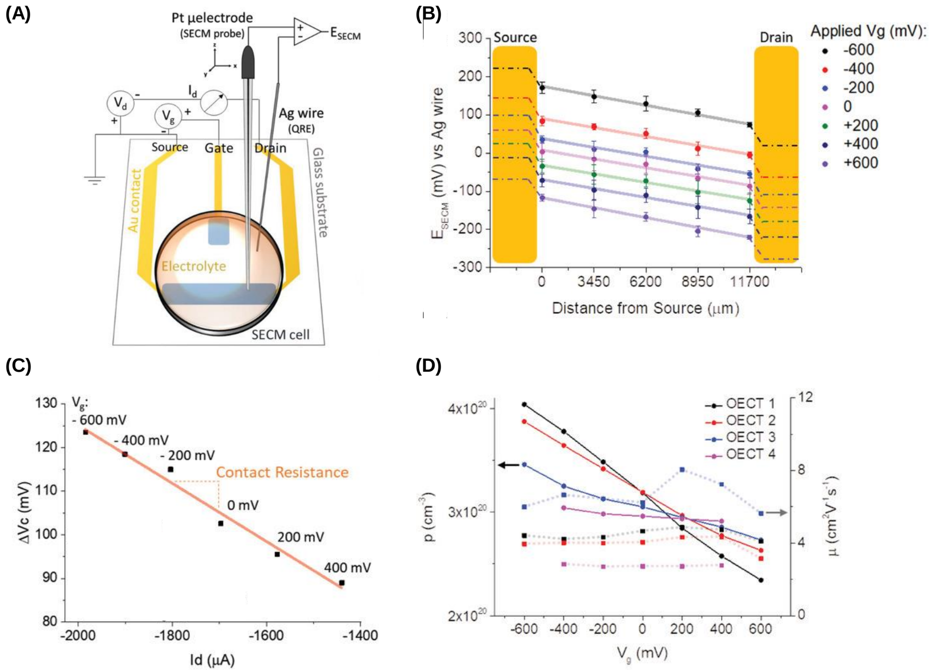

Figure 1.18: Scanning Electrochemical Microscopy (SECM). (A) Experimental setup for operando SECM on OECT for measurement of local electrochemical potential, (B) Electrochemical potential profile along the OECT channel in 0.1M PBS solution under different applied gate biases, (C) Contact potential drop (ΔV_c) as a function of drain current for different gate biases is used to determine the contact resistance (slope of the curve), (D) Estimated charge carrier density and mobility as a function of gate voltage for different OECTs measured. Adapted with permission from reference [90]. Copyright 2019 Wiley-VCH Verlag GmbH & Co. KGaA, Weinheim.

for example, to probe the charge transport across grain boundaries in heterogeneous blend semiconductors. Also, the imaging capabilities are cumbersome as the SECM measurement reported required re-polishing the microelectrode before probing a different location of the polymer surface. Nonetheless, the reported implementation provides a necessary proof-of-concept for further developments and exploration.

1.6.4. In-Liquid Scanning Dielectric Microscopy (in-Liquid SDM)

Scanning Dielectric Microscopy (SDM) is a scanning probe-based technique which allows high-resolution functional mapping of dielectric properties in air[113–121] and in-liquid environments[122–128]. The in-Liquid SDM is of particular interest as it allows direct probing of electrical material properties such as dielectric constant and/or conductivity in an aqueous environment by measurements of local electrostatic forces. In in-liquid SDM, a high frequency (in the 10's of MHz range) voltage is applied to the conductive AFM tip (SDM probe) whose amplitude is modulated by a low-frequency signal (in the kHz range). Given the quadratic dependence of the electric force acting on the tip on the applied potential, applying an amplitude-modulated (AM) waveform to the SDM probe leads, among other harmonics, to a modulated static bending of the cantilever at the modulation frequency which encodes the high-frequency information. The measured electrostatic force encodes the information about electrically relevant local properties like dielectric constant, conductivity, and interfacial capacitances, which are generally extracted by modelling the tip-sample interactions using physical models solved by the finite element method[125,128].

Kyndiah et al.[128] first implemented the in-liquid SDM technique for in-operando EGOFET characterization (specifically on diF-TES-ADT:PS blend semiconductor operated in a milli-Q environment in the saturation regime, as shown in Figure 1.19A). In this setup, a DC offset voltage, in addition to the amplitude-modulated waveform, is also applied to the tip which acts as the gate voltage. So, the expression of tip voltage applied in in-Liquid SDM implementation on a transistor is

$$[V_{Tip}]_{in-Liquid\ SDM} = V_{DC} + \frac{v_{ac}}{2}\left(1 + cos(\omega_{mod} t)\right) cos(\omega_{el} t) \tag{1.3}$$

The modulation frequency ($\omega_{wod}/2\pi$) is kept below the mechanical resonance frequency of the cantilever to avoid any mechanical cross-talk with the electrical signal. On the other hand, the high frequency ($\omega_{el}/2\pi$) is beyond the mechanical resonance frequency of the cantilever and at the same time, it needs to be above the dielectric relaxation frequency of the electrolyte to avoid screening by mobile ions in the electrolyte and facilitate the detection of electrostatic forces.

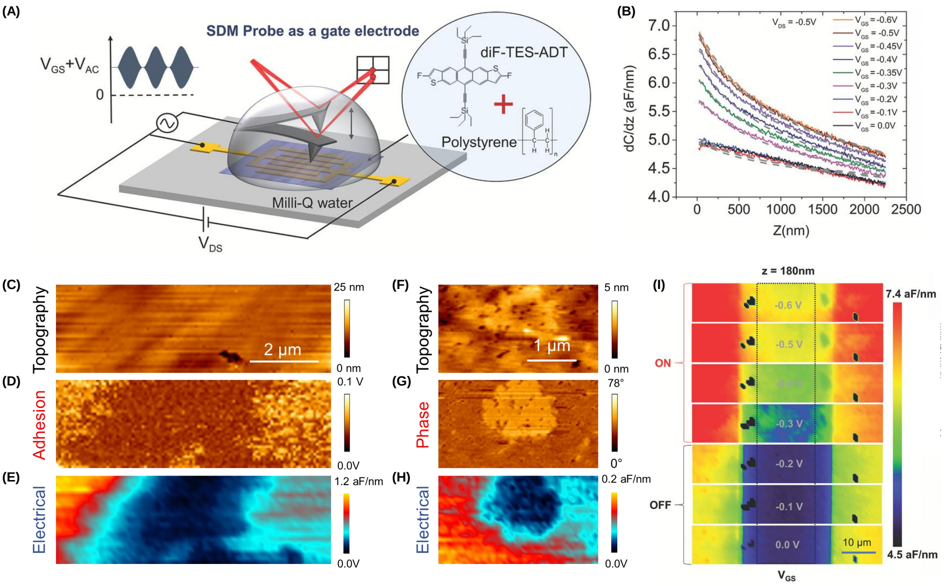

Figure 1.19: In-Liquid Scanning Dielectric Microscopy (in-Liquid SDM). (A) Schematic of the in-Liquid SDM implementation on EGOFET, (B) Electrostatic force represented in terms of capacitance gradient as a function of tip-sample distance for different applied gate potentials, (C) Topography, (D) Adhesion, (E) Constant height electrostatic force image at $z = 30nm$ of the zoomed region in the channel area of the transistor, (F) Topograph, (G) Mechanical phase, (H) Constant height electrostatic force image at $z = 30nm$ of another zoom region in the channel, and (I) Constant height electrostatic force images at $z = 180nm$ for different gate voltages (V_{GS}) and for the drain voltage of $V_{\mathrm{DS}} = -0.5V$. Adapted with permission from reference [128]. Copyright 2020 Wiley-VCH GmbH.

$$f_d = \frac{1}{2\pi R_{sol} C_{sol}} = \frac{1}{2\pi \rho_{sol} \varepsilon_{sol}} = \frac{\Lambda c}{2\pi \varepsilon_0 \varepsilon_{r,sol}} \tag{1.4}$$

Equation 1.4 gives the expression for estimating the dielectric relaxation frequency, where R_{sol} is the solution bulk resistance, C_{sol} is the solution bulk capacitance, ρ_{sol} is the solution resistivity, ε_{sol} is the solution dielectric permittivity, ε_0 is the vacuum permittivity, $\varepsilon_{r,sol}$ is the relative dielectric constant of the solution, Λ is the solution molar conductivity, and c is the solution concentration. For the NaCl solution, the molar conductivity is $12.6 Sm^{-1}M^{-1}$, so for 1mM NaCl solution, we have $f_d \approx 3MHz$, which thus warrants the use of high frequencies in the 10's of MHz range. These high frequencies do not affect the transistor operation and are not able to modulate the channel conductivity as the transit frequency of the transistor studied is well below these frequencies. This makes the measured electrostatic force to be only sensitive to the semiconductor conductivity and fixed interfacial capacitances[128].

The measured electrostatic force has a tip-sample distance dependence as shown in Figure 1.19B (represented in terms of capacitance gradient dC/dz, which is related to the force by $F_{\omega mod} = 1/8\ dC/dz\ v_{ac}{}^2)$[125], which ensures the locality of the measurements and is reported to have a lateral spatial resolution of $\approx 100nm$. As evident from the trend, the electrostatic force starts increasing as the gate voltage surpasses the threshold voltage and the conductivity is high enough to be detected by the SDM probe. The force increases further as the conductivity of the semiconductor increases in the ON state of the device until the force saturates and it is not any more dependent on the conductivity (i.e. the force is sensitive to the conductivity only in a certain range of conductivity values). Such approach curves are taken at every pixel in the device, known as the so-called force volume acquisition mode, from which electrostatic constant height images are generated at a particular constant distance from the substrate. Fitting the whole distance dependence of the electrostatic force with finite element simulations enables accurate estimation of local electrical properties (of course, within the range of sensitivity to them).

The measurements are shown to be sensitive to the electrical heterogeneities caused by the presence of an ultra-thin polystyrene layer on top of the semiconductor due to vertical phase separation phenomena commonly observed in blend-based devices, as shown in Figure 1.19(C-H). The ultra-thin polystyrene layers are identified based on the adhesion and mechanical phase contrast as the topography shows very little variation. On the other hand, the electrostatic force image shows a clear signature of electrical heterogeneity.

Figure 1.19I show the electrostatic force mapping on the region spanning the source-channel-drain area, where the transition from the OFF to ON state is clearly evident. The source/drain shows a noticeable contrast with respect to the channel regions, which is attributed to the presence of a metal electrode versus an insulating substrate beneath the semiconducting film (see Figure 1.20 where the dependence of the theoretically calculated electric force on the conductivity on the source and channel, for different interfacial capacitances, are plotted).

An important aspect to note is that the electrostatic force is influenced by both the variation in conductivity and interfacial capacitances as shown in Figure 1.20.

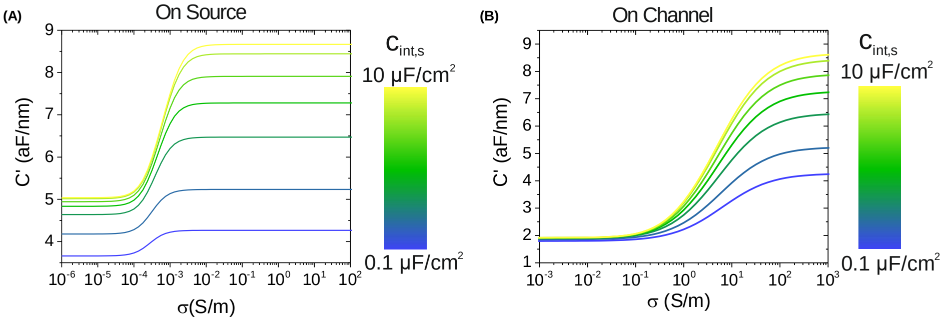

Figure 1.20: Simulated capacitance gradient (electrostatic force) at $Z = 50nm$ as a function of semiconductor conductivity for different interfacial capacitances on (A) Source, and (B) Channel. Adapted with permission from reference [128]. Copyright 2020 Wiley-VCH GmbH.

Decoupling them is challenging as one needs to be assumed constant while quantifying the other. Nonetheless, in-Liquid SDM is a powerful technique to probe the nanoscale electrical properties of operating devices.

1.7. Motivation and Objectives of the Thesis

Organic semiconductors and mixed ionic-electronic conductors with their tunable multifunctional characteristics have tremendous potential in creating futuristic technologies and enabling emerging applications in spaces where conventional silicon electronics are not the ideal candidates for example in interfacing with biological systems, as highlighted in this introductory chapter. Electrolyte-gated transistors are the fundamental blocks leveraging the potential of these materials and are topics of continuous research and development across academia and industry.

Despite being the foundational architecture, our fundamental understanding of the nanoscale modalities governing the device operation remains poor, which has been the roadblock in the development of application-relevant design rules towards targeted optimization of devices. Recently, a growing interest and attention have been diverted to developing experimental techniques and methods to probe dynamic changes in different modalities like electrical, mechanical, morphological, compositional, and molecular structural in operating devices. Some scanning probe-based techniques have emerged such as Electrochemical Strain Microscopy

(ESM), Scanning Electrochemical Microscopy (SECM) and in-liquid Scanning dielectric microscopy (in-liquid SDM), which have provided access to relevant mechanical and electrical properties, as discussed in section 1.6. However, they mostly have been proof-of-concept studies lacking any comprehensive exploration of these techniques' potential to probe materials and devices and have limited success in forming design rules for the targeted optimization of devices and gaining fundamental insight into their operating mechanism. On the other side, some of these and other beyond scanning probe-based operando techniques are performed in architectures that do not reflect the actual operating conditions in application-relevant scenarios either due to technical challenges in integrating the devices in standard experimental setups or due to limitations of the techniques themselves in resolving changes at the nanoscale level. Therefore, much still needs to be understood and explored from both the device and technique perspectives, with an emphasis on comprehensively probing the nanoscale dynamic response of the devices as a function of bias voltages and even better with a multimodal approach (e.g. electrical and mechanical) for a unified understanding.

This thesis aims to address these challenges and develop an advanced experimental setup to simultaneously probe different modalities (morphology, electrical, mechanical) at the nanoscale in operating electrolyte-gated transistors (EGTs) under close to application-relevant geometries, conditions and environments. The starting point of the work of thesis is an existing in-Liquid Scanning Dielectric Microscopy (in-Liquid SDM) implementation discussed earlier in subsection 1.6.4 to which we aim to add automated data acquisition and analysis functionality for comprehensive and simultaneous multimodal probing. The comprehensive analysis aided by the automated data acquisition approach takes the guesswork out of the equation and reveals the operating mechanism clearly. A particular emphasis is also on developing standardized approaches for integrating EGTs with an AFM setup for stable and reproducible connections and measurements. We would explore both kinds of EGTs introduced earlier, namely Electrolyte-Gated Organic Field-Effect Transistors (EGOFETs) and Organic Electrochemical Transistors (OECTs).

For EGOFETs, we chose the devices based on a blend of organic semiconducting material diF-TES-ADT and the insulating polymer polystyrene (PS)[30], which our group used as a stable bioelectronic recording platform for excitable cells[61] (mentioned earlier in Figure 1.11) and as a test platform to demonstrate the capabilities of in-Liquid SDM[128] (discussed earlier in subsection 1.6.4). The small molecule organic semiconductor diF-TES-ADT is a state-of-the-art material (refer subsection 1.4.1), and the structure-property relationships in its solid-state OFETs are well-studied with other techniques[51,129], thus providing the basis for corroborating our results. In these devices, the emphasis will be on exploring all operating regimes, namely sub-threshold, linear and saturation, with an additional focus on understanding the impact of microstructures and different non-idealities on the charge carrier transport to reveal various bottlenecks. The semiconducting thin film in these devices exhibits polycrystallinity whose impact on performance needs to be understood under operating conditions.

We then move to a more complex device showing multimodal behaviour, which is an OECT where the penetrations of ions into the semiconductor lead to various physical and chemical changes. For OECTs, we choose the devices based on state-of-the-art n-type ladder polymer BBL[73] (mentioned earlier in subsection 1.4.2). BBL is a homogenous π-conjugated redox polymer where ionic and electronic processes are not phase separated and thus demands probing of individual and coupled processes simultaneously, making it a perfect testbed for our multimodal (morphological, electrical, and mechanical) studies. We also aim to explore device behaviour in the high doping state leading to antiambipolar characteristics, which enables fascinating applications as mentioned earlier in Figure 1.14.

These thesis objectives would enable the development of structure-property-function relationships in functional devices and would aid in the fundamental understanding of ionic-electronic coupling and resulting complex processes.

1.8. Structure of the Thesis

This thesis is organized as follows:

The present chapter (Chapter 1) provides the relevant background information on organic semiconductors and the devices based on them, their architectures, figures of merit and applications. The later part of the chapter deals with the operando characterizations, requirements and challenges, and a brief literature review of scanning probe microscopy-based operando methods and ultimately addresses the motivation and objective of this thesis.

In Chapter 2, we dwell on the details of the methods, improved measurement protocols and data representation approaches developed during the project of the thesis along with the automated functionalities implemented on top of the existing in-Liquid SDM as a part of this thesis. A new potential mapping mode based on in-Liquid SDM is introduced that provides quantitative information without requiring calibration or finite element simulations, offering significant advantages and improving the accessibility of the technique.

Chapter 3 provides the results on the nanoscale operando characterization of EGOFETs based on semiconductor-insulator blends in different operating regimes, namely subthreshold, linear and saturation, focusing on revealing how the polycrystalline structure of the semiconductor film affects the local electrical properties (conductivity and potential) that prohibit the device in reaching its full potential.

Chapter 4 deals with the nanoscale multimodal characterization of OECTs in different operation regimes by simultaneously focusing on electrical and mechanical properties, revealing the multifunctional characteristics of organic mixed-ionic electronic conductors. The operating mechanism at high doping states leading to negative transconductance regime and antiambipolar behaviour are also probed, opening up en route to fundamental studies in extreme conditions and new fascinating applications.

Chapter 5 discusses some of the implications of the present thesis on our fundamental understanding of materials and devices in operating conditions.

Finally, Chapter 6 presents the main conclusions achieved in the thesis with an overview of possible future studies and applications.

1.9. References

1. G. H. Gelinck, H. E. A. Huitema, E. van Veenendaal, et al., “Flexible active-matrix displays and shift registers based on solution-processed organic transistors,” *Nature Materials*, vol. 3, pp. 106–110, 2004. doi:10.1038/nmat1061

2. S. Löffler, K. Melican, K. P. R. Nilsson, and A. Richter-Dahlfors, “Organic bioelectronics in medicine,” *Journal of Internal Medicine*, vol. 282, pp. 24–36, 2017. doi:https://doi.org/10.1111/joim.12595

3. H. Bronstein, C. B. Nielsen, B. C. Schroeder, and I. McCulloch, “The role of chemical design in the performance of organic semiconductors,” *Nature Reviews Chemistry*, vol. 4, pp. 66–77, 2020. doi:10.1038/s41570-019-0152-9

4. Y. Zheng, S. Zhang, J. B.-H. Tok, and Z. Bao, “Molecular design of stretchable polymer semiconductors: Current progress and future directions,” *Journal of the American Chemical Society*, vol. 144, pp. 4699–4715, 2022. doi:10.1021/jacs.2c00072

5. H. Liu, D. Liu, J. Yang, H. Gao, and Y. Wu, “Flexible electronics based on organic semiconductors: from patterned assembly to integrated applications,” *Small*, vol. 19, p. 2206938, 2023. doi:https://doi.org/10.1002/smll.202206938

6. L. Sun, K. Fukuda, and T. Someya, “Recent progress in solution-processed flexible organic photovoltaics,” *npj Flexible Electronics*, vol. 6, p. 89, 2022. doi:10.1038/s41528-022-00222-3

7. X. Xu, Y. Zhao, and Y. Liu, “Wearable electronics based on stretchable organic semiconductors,” *Small*, vol. n/a, p. 2206309, 2023. doi:10.1002/smll.202206309

8. Y. H. Lee, O. Y. Kweon, H. Kim, J. H. Yoo, S. G. Han, and J. H. Oh, “Recent advances in organic sensors for health self-monitoring systems,” *J. Mater. Chem. C*, vol. 6, pp. 8569–8612, 2018. doi:10.1039/C8TC02230E

9. H. Roh, C. Cunin, S. Samal, and A. Gumyusenge, “Towards organic electronics that learn at the body-machine interface: A materials journey,” *MRS Communications*, vol. 12, pp. 565–577, 2022. doi:10.1557/s43579-022-00269-3

10. K. Birmingham, V. Gradinaru, P. Anikeeva, et al., “Bioelectronic medicines: a research roadmap,” *Nature Reviews Drug Discovery*, vol. 13, pp. 399–400, 2014. doi:10.1038/nrd4351

11. S. Wang, X. Chen, C. Zhao, et al., “An organic electrochemical transistor for multi-modal sensing, memory and processing,” *Nature Electronics*, vol. 6, pp. 281–291, 2023. doi:10.1038/s41928-023-00950-y

12. P. Flowers, W. R. Robinson, R. Langley, and K. Theopold, *Chemistry*. Houston, Texas: OpenStax, 2015. https://openstax.org/books/chemistry/pages/1-introduction

13. N. Prasad, S. Tanwar, S. Mukhopadhyay, and T. Kundu, “Spatio-temporal analysis of the electric field-induced solid-state reduction dynamics of

graphene oxide thin films for controlled band-gap modulation," *The Journal of Physical Chemistry C*, vol. 124, pp. 21 874–21 885, 2020. doi: 10.1021/acs.jpcc.0c07139

14. Z. Zhu, Y. Guo, and Y. Liu, "Application of organic field-effect transistors in memory," *Mater. Chem. Front.*, vol. 4, pp. 2845–2862, 2020. doi:10.1039/D0QM00330A

15. S. Nam, Y.-G. Ko, S. Gyu Hahm, et al., "Organic nonvolatile memory transistors with self-doped polymer energy well structures," *NPG Asia Materials*, vol. 5, pp. e33–e33, 2013. doi:10.1038/am.2012.62

16. V. R. Rao and S. G. Surya, "Organic field effect transistors for explosive and radiation dosimetry applications," in *2016 IEEE SENSORS*, 2016, pp. 1–3. doi:10.1109/ICSENS.2016.7808602

17. Y. Zang, F. Zhang, D. Huang, X. Gao, C.-a. Di, and D. Zhu, "Flexible suspended gate organic thin-film transistors for ultra-sensitive pressure detection," *Nature Communications*, vol. 6, p. 6269, 2015. doi:10.1038/ncomms7269

18. A. J. Kronemeijer, E. Gili, M. Shahid, et al., "A selenophene-based low-bandgap donor–acceptor polymer leading to fast ambipolar logic," *Advanced Materials*, vol. 24, pp. 1558–1565, 2012. doi:https://doi.org/10.1002/adma.201104522

19. J. Zaumseil, R. H. Friend, and H. Sirringhaus, "Spatial control of the recombination zone in an ambipolar light-emitting organic transistor," *Nature Materials*, vol. 5, pp. 69–74, 2006. doi:10.1038/nmat1537

20. H. S. White, G. P. Kittlesen, and M. S. Wrighton, "Chemical derivatization of an array of three gold microelectrodes with polypyrrole: fabrication of a molecule-based transistor," *Journal of the American Chemical Society*, vol. 106, pp. 5375–5377, 1984. doi:10.1021/ja00330a070

21. C. Liu, Y. Xu, and Y.-Y. Noh, "Contact engineering in organic field-effect transistors," *Materials Today*, vol. 18, pp. 79–96, 2015. doi:https://doi.org/10.1016/j.mattod.2014.08.037

22. M. Fahlman, S. Fabiano, V. Gueskine, D. Simon, M. Berggren, and X. Crispin, “Interfaces in organic electronics,” *Nature Reviews Materials*, vol. 4, pp. 627–650, 2019. doi:10.1038/s41578-019-0127-y

23. H. Chen, W. Zhang, M. Li, G. He, and X. Guo, “Interface engineering in organic field-effect transistors: Principles, applications, and perspectives,” *Chemical Reviews*, vol. 120, pp. 2879–2949, 2020. doi:10.1021/acs.chemrev.9b00532

24. J. Zeng, D. He, J. Qiao, et al., “Ultralow contact resistance in organic transistors via orbital hybridization,” *Nature Communications*, vol. 14, p. 324, 2023. doi:10.1038/s41467-023-36006-0

25. J. T. Friedlein, R. R. McLeod, and J. Rivnay, “Device physics of organic electrochemical transistors,” *Organic Electronics*, vol. 63, pp. 398–414, 2018. doi:10.1016/j.orgel.2018.09.010

26. J. Rivnay, S. Inal, A. Salleo, R. M. Owens, M. Berggren, and G. G. Malliaras, “Organic electrochemical transistors,” *Nature Reviews Materials*, vol. 3, p. 17086, 2018. doi:10.1038/natrevmats.2017.86

27. B. D. Paulsen, K. Tybrandt, E. Stavrinidou, and J. Rivnay, “Organic mixed ionic–electronic conductors,” *Nature Materials*, vol. 19, pp. 13–26, 2020. doi:10.1038/s41563-019-0435-z

28. G. Schweicher, G. Garbay, R. Jouclas, F. Vibert, F. Devaux, and Y. H. Geerts, “Molecular semiconductors for logic operations: Dead-end or bright future?” *Advanced Materials*, vol. 32, p. 1905909, 2020. doi:10.1002/adma.201905909

29. F. Torricelli, D. Z. Adrahtas, Z. Bao, et al., “Electrolyte-gated transistors for enhanced performance bioelectronics,” *Nature Reviews Methods Primers*, vol. 1, p. 66, 2021. doi:10.1038/s43586-021-00065-8

30. Q. Zhang, F. Leonardi, S. Casalini, I. Temiño, and M. Mas-Torrent, “High performing solution-coated electrolyte-gated organic field-effect transistors for aqueous media operation,” *Scientific Reports*, vol. 6, p. 39623, 2016. doi:10.1038/srep39623

31. S. P. White, K. D. Dorfman, and C. D. Frisbie, “Operating and sensing mechanism of electrolyte-gated transistors with floating gates: Building a platform for amplified biodetection,” *The Journal of Physical Chemistry C*, vol. 120, pp. 108–117, 2016. doi:10.1021/acs.jpcc.5b10694
32. L. Huetter, A. Kyndiah, and G. Gomila, “Analytical physical model for electrolyte gated organic field effect transistors in the helmholtz approximation,” *Advanced Theory and Simulations*, vol. n/a, p. 2200696, 2023. doi:10.1002/adts.202200696
33. C. G. Sodini, “Lecture 8 - 6.012 electronic devices and circuits - fall 2000,” 2000. http://web.mit.edu/6.012/FALL00/www/handouts/lec8.pdf
34. L. Huetter, A. Kyndiah, and G. Gomila, “Analytical physical model for organic metal-electrolyte-semiconductor capacitors,” *Advanced Theory and Simulations*, vol. 6, p. 2200698, 2023. doi:10.1002/adts.202200698
35. C. G. Shuttle, R. Hamilton, J. Nelson, B. C. O’Regan, and J. R. Durrant, “Measurement of charge-density dependence of carrier mobility in an organic semiconductor blend,” *Advanced Functional Materials*, vol. 20, pp. 698–702, 2010. doi:https://doi.org/10.1002/adfm.200901734
36. A. Pivrikas, M. Ullah, H. Sitter, and N. S. Sariciftci, “Electric field dependent activation energy of electron transport in fullerene diodes and field effect transistors: Gill’s law,” *Applied Physics Letters*, vol. 98, 2011, 092114. doi:10.1063/1.3557503
37. S. K. Shukri and L. D. Deja, “Charge carriers density, temperature, and electric field dependence of the charge carrier mobility in disordered organic semiconductors in low density region,” *Condensed Matter*, vol. 6, 2021. doi:10.3390/condmat6040038
38. T. Mori, T. Oyama, H. Komiyama, and T. Yasuda, “Solution-grown unidirectionally oriented crystalline thin films of a u-shaped thienoacene-based semiconductor for high-performance organic field-effect transistors,” *J. Mater. Chem. C*, vol. 5, pp. 5872–5876, 2017. doi:10.1039/C7TC01836C
39. T. He, X. Zhang, J. Jia, Y. Li, and X. Tao, “Three-dimensional charge transport in organic semiconductor single crystals,” *Advanced Materials*, vol. 24, pp. 2171–2175, 2012. doi:10.1002/adma.201200525

40. V. C. Sundar, J. Zaumseil, V. Podzorov, et al., “Elastomeric transistor stamps: Reversible probing of charge transport in organic crystals,” *Science*, vol. 303, pp. 1644–1646, 2004. doi:10.1126/science.1094196

41. A. F. Paterson, S. Singh, K. J. Fallon, et al., “Recent progress in high-mobility organic transistors: A reality check,” *Advanced Materials*, vol. 30, p. 1801079, 2018. doi:10.1002/adma.201801079

42. U. Zschieschang, J. W. Borchert, M. Giorgio, et al., “Roadmap to gigahertz organic transistors,” *Advanced Functional Materials*, vol. 30, p. 1903812, 2020. doi:10.1002/adfm.201903812

43. D. Choi, P.-H. Chu, M. McBride, and E. Reichmanis, “Best Practices for Reporting Organic Field Effect Transistor Device Performance,” *Chemistry of Materials*, vol. 27, pp. 4167–4168, 2015. doi:10.1021/acs.chemmater.5b01982

44. I. McCulloch, A. Salleo, and M. Chabinyc, “Avoid the kinks when measuring mobility,” *Science*, vol. 352, pp. 1521–1522, 2016. doi:10.1126/science.aaf9062

45. Z. Cheng, C.-S. Pang, P. Wang, et al., “How to report and benchmark emerging field-effect transistors,” *Nature Electronics*, vol. 5, pp. 416–423, 2022. doi:10.1038/s41928-022-00798-8

46. D. Khodagholy, J. Rivnay, M. Sessolo, et al., “High transconductance organic electrochemical transistors,” *Nature Communications*, vol. 4, p. 2133, 2013. doi:10.1038/ncomms3133

47. J. Rivnay, P. Leleux, M. Ferro, et al., “High-performance transistors for bioelectronics through tuning of channel thickness,” *Science Advances*, vol. 1, p. e1400251, 2015. doi:10.1126/sciadv.1400251

48. C. R. Newman, C. D. Frisbie, D. A. da Silva Filho, J.-L. Brédas, P. C. Ewbank, and K. R. Mann, “Introduction to organic thin film transistors and design of n-channel organic semiconductors,” *Chemistry of Materials*, vol. 16, pp. 4436–4451, 2004. doi:10.1021/cm049391x

49. M. Sanaullah and M. H. Chowdhury, “Subthreshold swing characteristics of multilayer mos2 tunnel fet,” in *2015 IEEE 58th International Midwest Symposium on Circuits and Systems (MWSCAS)*, 2015 IEEE 58th International

Midwest Symposium on Circuits and Systems (MWSCAS), 2015, pp. 1–4. doi:10.1109/MWSCAS.2015.7282101

50. S. Inal, G. G. Malliaras, and J. Rivnay, "Benchmarking organic mixed conductors for transistors," *Nature Communications*, vol. 8, p. 1767, 2017. doi:10.1038/s41467-017-01812-w

51. R. Li, J. W. Ward, D.-M. Smilgies, et al., "Direct structural mapping of organic field-effect transistors reveals bottlenecks to carrier transport," *Advanced Materials*, vol. 24, pp. 5553–5558, 2012. doi:10.1002/adma.201201856

52. M. Demelas, S. Lai, A. Spanu, et al., "Charge sensing by organic charge-modulated field effect transistors: application to the detection of bio-related effects," *J. Mater. Chem. B*, vol. 1, pp. 3811–3819, 2013. doi:10.1039/C3TB20237B

53. S. P. White, S. Sreevatsan, C. D. Frisbie, and K. D. Dorfman, "Rapid, selective, label-free aptameric capture and detection of ricin in potable liquids using a printed floating gate transistor," *ACS Sensors*, vol. 1, pp. 1213–1216, 2016. doi:10.1021/acssensors.6b00481

54. M. S. Thomas, S. P. White, K. D. Dorfman, and C. D. Frisbie, "Interfacial charge contributions to chemical sensing by electrolyte-gated transistors with floating gates," *The Journal of Physical Chemistry Letters*, vol. 9, pp. 1335–1339, 2018. doi:10.1021/acs.jpclett.8b00285

55. M. Magliulo, A. Mallardi, M. Y. Mulla, et al., "Electrolyte-gated organic field-effect transistor sensors based on supported biotinylated phospholipid bilayer," *Advanced Materials*, vol. 25, pp. 2090–2094, 2013. doi:https://doi-org.sire.ub.edu/10.1002/adma.201203587

56. M. Y. Mulla, E. Tuccori, M. Magliulo, et al., "Capacitance-modulated transistor detects odorant binding protein chiral interactions," *Nature Communications*, vol. 6, p. 6010, 2015. doi:10.1038/ncomms7010

57. G. Palazzo, D. De Tullio, M. Magliulo, et al., "Detection beyond debye's length with an electrolyte-gated organic field-effect transistor," *Advanced Materials*, vol. 27, pp. 911–916, 2015. doi:https://doi.org/10.1002/adma.201403541

58. E. Macchia, K. Manoli, B. Holzer, et al., “Single-molecule detection with a millimetre-sized transistor,” *Nature Communications*, vol. 9, p. 3223, 2018. doi:10.1038/s41467-018-05235-z

59. C. Di Franco, E. Macchia, L. Sarcina, et al., “Extended work function shift of large-area biofunctionalized surfaces triggered by a few single-molecule affinity binding events,” *Advanced Materials Interfaces*, vol. 10, p. 2201829, 2023. doi:https://doi.org/10.1002/admi.202201829

60. G. Giorgi, N. Lago, S. Tonello, et al., “Rl-egofet cell biosensors: A novel approach for the detection of action potentials,” in *2021 IEEE International Symposium on Medical Measurements and Applications (MeMeA)*, 2021, pp. 1–6. doi:10.1109/MeMeA52024.2021.9478747

61. A. Kyndiah, F. Leonardi, C. Tarantino, et al., “Bioelectronic recordings of cardiomyocytes with accumulation mode electrolyte gated organic field effect transistors,” *Biosensors and Bioelectronics*, vol. 150, p. 111844, 2020. doi:https://doi.org/10.1016/j.bios.2019.111844

62. C. A. Bortolotti, M. Berto, M. Sensi, M. D. Lauro, and F. Biscarini, “Biosensing with electrolyte gated organic field effect transistors,” in *Organic Bioelectronics for Life Science and Healthcare*. Materials Research Foundations, 2019, vol. 56, pp. 71–96. doi:10.21741/9781644900376-2

63. B. Burtscher, P. A. Manco Urbina, C. Diacci, et al., “Sensing inflammation biomarkers with electrolyte-gated organic electronic transistors,” *Advanced Healthcare Materials*, vol. 10, p. 2100955, 2021. doi:https://doi.org/10.1002/adhm.202100955

64. C. Pitsalidis, A.-M. Pappa, A. J. Boys, et al., “Organic bioelectronics for in vitro systems,” *Chemical Reviews*, vol. 122, pp. 4700–4790, 2022. doi:10.1021/acs.chemrev.1c00539

65. A. Spanu, L. Martines, and A. Bonfiglio, “Interfacing cells with organic transistors: a review of in vitro and in vivo applications,” *Lab on a Chip*, vol. 21, pp. 795–820, 2021. doi:10.1039/d0lc01007c

66. Y. He, N. A. Kukhta, A. Marks, and C. K. Luscombe, “The effect of side chain engineering on conjugated polymers in organic electrochemical transistors for bioelectronic applications,” *Journal of Materials Chemistry C*, vol. 10, pp. 2314–2332, 2022. doi:10.1039/D1TC05229B

67. D. Moia, A. Giovannitti, A. A. Szumska, et al., “Design and evaluation of conjugated polymers with polar side chains as electrode materials for electrochemical energy storage in aqueous electrolytes,” *Energy & Environmental Science*, vol. 12, pp. 1349–1357, 2019. doi:10.1039/c8ee03518k

68. P. C. Harikesh, C.-Y. Yang, H.-Y. Wu, et al., “Ion-tunable antiambipolarity in mixed ion–electron conducting polymers enables biorealistic organic electrochemical neurons,” *Nature Materials*, vol. 22, pp. 242–248, 2023. doi:10.1038/s41563-022-01450-8

69. S. T. M. Tan, A. Gumyusenge, T. J. Quill, et al., “Mixed ionic–electronic conduction, a multifunctional property in organic conductors,” *Advanced Materials*, vol. 34, p. 2110406, 2022. doi:10.1002/adma.202110406

70. S. T. Keene, T. P. A. van der Pol, D. Zakhidov, et al., “Enhancement-mode pedot:pss organic electrochemical transistors using molecular de-doping,” *Advanced Materials*, vol. 32, p. 2000270, 2020. doi:10.1002/adma.202000270

71. W. Huang, J. Chen, Y. Yao, et al., “Vertical organic electrochemical transistors for complementary circuits,” *Nature*, vol. 613, pp. 496–502, 2023. doi:10.1038/s41586-022-05592-2

72. P. Andersson Ersman, R. Lassnig, J. Strandberg, et al., “All-printed large-scale integrated circuits based on organic electrochemical transistors,” *Nature Communications*, vol. 10, p. 5053, 2019. doi:10.1038/s41467-019-13079-4

73. H. Sun, M. Vagin, S. Wang, et al., “Complementary logic circuits based on high-performance n-type organic electrochemical transistors,” *Advanced Materials*, vol. 30, p. 1704916, 2018. doi:https://doi.org/10.1002/adma.201704916

74. X. Ji, B. D. Paulsen, G. K. K. Chik, et al., “Mimicking associative learning using an ion-trapping non-volatile synaptic organic electrochemical transistor,” *Nature Communications*, vol. 12, p. 2480, 2021. doi:10.1038/s41467-021-22680-5

75. X. Ji, X. Lin, and J. Rivnay, “Organic electrochemical transistors as on-site signal amplifiers for electrochemical aptamer-based sensing,” *Nature Communications*, vol. 14, p. 1665, 2023. doi:10.1038/s41467-023-37402-2

76. K. Guo, S. Wustoni, A. Koklu, et al., “Rapid single-molecule detection of covid-19 and mers antigens via nanobody-functionalized organic electrochemical transistors,” *Nature Biomedical Engineering*, vol. 5, pp. 666–677, 2021. doi:10.1038/s41551-021-00734-9

77. A. Williamson, M. Ferro, P. Leleux, et al., “Localized neuron stimulation with organic electrochemical transistors on delaminating depth probes,” *Advanced Materials*, vol. 27, pp. 4405–4410, 2015. doi:https://doi.org/10.1002/adma.201500218

78. A. Marks, S. Griggs, N. Gasparini, and M. Moser, “Organic electrochemical transistors: An emerging technology for biosensing,” *Advanced Materials Interfaces*, vol. 9, p. 2102039, 2022. doi:https://doi.org/10.1002/admi.202102039

79. R. B. Rashid, X. Ji, and J. Rivnay, “Organic electrochemical transistors in bioelectronic circuits,” *Biosensors and Bioelectronics*, vol. 190, p. 113461, 2021. doi:https://doi.org/10.1016/j.bios.2021.113461

80. M. Sophocleous, L. Contat-Rodrigo, E. García-Breijo, and J. Georgiou, “Organic electrochemical transistors as an emerging platform for bio-sensing applications: A review,” *IEEE Sensors Journal*, vol. 21, pp. 3977–4006, 2021. doi:10.1109/JSEN.2020.3033283

81. R. Wu, M. Matta, B. D. Paulsen, and J. Rivnay, “Operando characterization of organic mixed ionic/electronic conducting materials,” *Chemical Reviews*, vol. 122, pp. 4493–4551, 2022. doi:10.1021/acs.chemrev.1c00597

82. S. Jiang, Q. Dai, J. Guo, and Y. Li, “In-situ/operando characterization techniques for organic semiconductors and devices,” *Journal of Semiconductors*, vol. 43, p. 041101, 2022. doi:10.1088/1674-4926/43/4/041101

83. “Recommendations for terms relating to materials characterization: Latin and other introduced terms,” *Chemistry International*, vol. 43, pp. 32–33, 2021. doi:doi:10.1515/ci-2021-0417

84. V. Palermo, M. Palma, and P. Samorì, “Electronic characterization of organic thin films by kelvin probe force microscopy,” *Advanced Materials*, vol. 18, pp. 145–164, 2006. doi:10.1002/adma.200501394

85. L. Collins, S. Jesse, J. I. Kilpatrick, et al., “Probing charge screening dynamics and electrochemical processes at the solid–liquid interface with electrochemical force microscopy,” *Nature Communications*, vol. 5, p. 3871, 2014. doi:10.1038/ncomms4871

86. T. Hackl, G. Schitter, and P. Mesquida, “Ac kelvin probe force microscopy enables charge mapping in water,” *ACS Nano*, vol. 16, pp. 17 982–17 990, 2022. doi:10.1021/acsnano.2c07121

87. E. Stavrinidou, P. Leleux, H. Rajaona, et al., “Direct measurement of ion mobility in a conducting polymer,” *Advanced Materials*, vol. 25, pp. 4488–4493, 2013. doi:https://doi-org.sire.ub.edu/10.1002/adma.201301240

88. S. Inal, G. G. Malliaras, and J. Rivnay, “Optical study of electrochromic moving fronts for the investigation of ion transport in conducting polymers,” *J. Mater. Chem. C*, vol. 4, pp. 3942–3947, 2016. doi:10.1039/C5TC04354A

89. J. T. Friedlein, J. Rivnay, D. H. Dunlap, et al., “Influence of disorder on transfer characteristics of organic electrochemical transistors,” *Applied Physics Letters*, vol. 111, 2017, 023301. doi:10.1063/1.4993776

90. F. Mariani, F. Conzuelo, T. Cramer, et al., “Microscopic determination of carrier density and mobility in working organic electrochemical transistors,” *Small*, vol. 15, p. 1902534, 2019. doi:https://doi.org/10.1002/smll.201902534

91. D. Lyu, Y. Jin, P. C. M. M. Magusin, et al., “Operando nmr electrochemical gating studies of ion dynamics in pedot:pss,” *Nature Materials*, vol. 22, pp. 746–753, 2023. doi:10.1038/s41563-023-01524-1

92. B. D. Paulsen, A. Giovannitti, R. Wu, et al., “Electrochemistry of thin films with in situ/operando grazing incidence x-ray scattering: Bypassing electrolyte scattering for high fidelity time resolved studies,” *Small*, vol. 17, p. 2103213, 2021. doi:https://doi-org.sire.ub.edu/10.1002/smll.202103213

93. R. Giridharagopal, L. Q. Flagg, J. S. Harrison, et al., “Electrochemical strain microscopy probes morphology-induced variations in ion uptake and performance in organic electrochemical transistors,” *Nature Materials*, vol. 16, pp. 737–742, 2017. doi:10.1038/nmat4918

94. A. N. Morozovska, E. A. Eliseev, N. Balke, and S. V. Kalinin, “Local probing of ionic diffusion by electrochemical strain microscopy: Spatial resolution and signal formation mechanisms,” *Journal of Applied Physics*, vol. 108, 2010, 053712. doi:10.1063/1.3460637

95. L. Q. Flagg, R. Giridharagopal, J. Guo, and D. S. Ginger, “Anion-dependent doping and charge transport in organic electrochemical transistors,” *Chemistry of Materials*, vol. 30, pp. 5380–5389, 2018. doi:10.1021/acs.chemmater.8b02220

96. R. Giridharagopal, J. Guo, J. Kong, and D. S. Ginger, “Nanowire architectures improve ion uptake kinetics in conjugated polymer electrochemical transistors,” *ACS Applied Materials & Interfaces*, vol. 13, pp. 34 616–34 624, 2021. doi:10.1021/acsami.1c08176

97. J. Guo, L. Q. Flagg, D. K. Tran, et al., “Hydration of a side-chain-free n-type semiconducting ladder polymer driven by electrochemical doping,” *Journal of the American Chemical Society*, vol. 145, pp. 1866–1876, 2023. doi:10.1021/jacs.2c11468

98. S. Benaglia, S. Drakopoulou, F. Biscarini, and R. Garcia, “In operando nanomechanical mapping of PEDOT:PSS thin films in electrolyte solutions with bimodal AFM,” *Nanoscale*, vol. 14, pp. 14 146–14 154, 2022. doi:10.1039/d2nr02177c

99. C. A. Amo, A. P. Perrino, A. F. Payam, and R. Garcia, “Mapping elastic properties of heterogeneous materials in liquid with angstrom-scale resolution,” *ACS Nano*, vol. 11, pp. 8650–8659, 2017. doi:10.1021/acsnano.7b04381

100. V. G. Gisbert, S. Benaglia, M. R. Uhlig, R. Proksch, and R. Garcia, “High-speed nanomechanical mapping of the early stages of collagen growth by bimodal force microscopy,” *ACS Nano*, vol. 15, pp. 1850–1857, 2021. doi:10.1021/acsnano.0c10159

101. V. G. Gisbert and R. Garcia, “Accurate wide-modulus-range nanomechanical mapping of ultrathin interfaces with bimodal atomic force microscopy,” *ACS Nano*, vol. 15, pp. 20 574–20 581, 2021. doi:10.1021/acsnano.1c09178

102. S. Benaglia, V. G. Gisbert, A. P. Perrino, C. A. Amo, and R. Garcia, “Fast and high-resolution mapping of elastic properties of biomolecules and polymers

with bimodal afm," *Nature Protocols*, vol. 13, pp. 2890–2907, 2018. doi: 10.1038/s41596-018-0070-1

103. I. Traxler, T. D. Singewald, G. Schimo-Aichhorn, S. Hild, and M. Valtiner, "Scanning electrochemical microscopy methods (SECM) and ion-selective microelectrodes for corrosion studies," *Corrosion Reviews*, vol. 40, pp. 515–542, 2022. doi:doi:10.1515/corrrev-2021-0104

104. I. Beaulieu, S. Kuss, J. Mauzeroll, and M. Geissler, "Biological scanning electrochemical microscopy and its application to live cell studies," *Analytical Chemistry*, vol. 83, pp. 1485–1492, 2011. doi:10.1021/ac101906a

105. A. J. Bard, F.-R. F. Fan, D. T. Pierce, P. R. Unwin, D. O. Wipf, and F. Zhou, "Chemical imaging of surfaces with the scanning electrochemical microscope," *Science*, vol. 254, pp. 68–74, 1991. doi:10.1126/science.254.5028.68

106. G. Denuault, M. H. T. Frank, and L. M. Peter, "Scanning electrochemical microscopy: potentiometric probing of ion fluxes," *Faraday Discuss.*, vol. 94, pp. 23–35, 1992. doi:10.1039/FD9929400023

107. M. H. T. Frank and G. Denuault, "Scanning electrochemical microscopy: Probing the ingress and egress of protons from a polyaniline film," *Journal of Electroanalytical Chemistry*, vol. 354, pp. 331–339, 1993, an International Journal Devoted to all Aspects of Electrode Kinetics, Interfacial Structure, Properties of Electrolytes, Colloid and Biological Electrochemistry. doi: https://doi.org/10.1016/0022-0728(93)80347-K

108. M. Arca, M. V. Mirkin, and A. J. Bard, "Polymer films on electrodes. 26. study of ion transport and electron transfer at polypyrrole films by scanning electrochemical microscopy," *The Journal of Physical Chemistry*, vol. 99, pp. 5040–5050, 1995. doi:10.1021/j100014a026

109. D. Mandler and P. R. Unwin, "Measurement of lateral charge propagation in polyaniline layers with the scanning electrochemical microscope," *The Journal of Physical Chemistry B*, vol. 107, pp. 407–410, 2003. doi:10.1021/jp021623x

110. V. Syritski, R. Gyurcsányi, A. Öpik, and K. Tóth, "Synthesis and characterization of inherently conducting polymers by using scanning electrochemical microscopy and electrochemical quartz crystal microbalance,"

Synthetic Metals, vol. 152, pp. 133–136, 2005, proceedings of the International Conference on Science and Technology of Synthetic Metals. doi:https://doi.org/10.1016/j.synthmet.2005.07.097

111. N. Yang and C. G. Zoski, "Polymer films on electrodes: Investigation of ion transport at poly(3,4-ethylenedioxythiophene) films by scanning electrochemical microscopy," *Langmuir*, vol. 22, pp. 10 338–10 347, 2006. doi:10.1021/la061167u

112. D. Polcari, P. Dauphin-Ducharme, and J. Mauzeroll, "Scanning electrochemical microscopy: A comprehensive review of experimental parameters from 1989 to 2015," *Chemical Reviews*, vol. 116, pp. 13 234–13 278, 2016. doi:10.1021/acs.chemrev.6b00067

113. L. Fumagalli, D. Esteban-Ferrer, A. Cuervo, J. L. Carrascosa, and G. Gomila, "Label-free identification of single dielectric nanoparticles and viruses with ultraweak polarization forces," *Nature Materials*, vol. 11, pp. 808–816, 2012. doi:10.1038/nmat3369

114. M. Van Der Hofstadt, R. Fabregas, R. Millan-Solsona, A. Juarez, L. Fumagalli, and G. Gomila, "Internal hydration properties of single bacterial endospores probed by electrostatic force microscopy," *ACS Nano*, vol. 10, pp. 11 327–11 336, 2016. doi:10.1021/acsnano.6b06578

115. H. Lozano, R. Fabregas, N. Blanco-Cabra, et al., "Dielectric constant of flagellin proteins measured by scanning dielectric microscopy," *Nanoscale*, vol. 10, pp. 19 188–19 194, 2018. doi:10.1039/C8NR06190D

116. M. Checa, R. Millan-Solsona, N. Blanco, E. Torrents, R. Fabregas, and G. Gomila, "Mapping the dielectric constant of a single bacterial cell at the nanoscale with scanning dielectric force volume microscopy," *Nanoscale*, vol. 11, pp. 20 809–20 819, 2019. doi:10.1039/C9NR07659J

117. H. Balakrishnan, R. Fabregas, R. Millan-Solsona, L. Fumagalli, and G. Gomila, "Spatial Resolution and Capacitive Coupling in the Characterization of Nanowire Nanocomposites by Scanning Dielectric Microscopy," *Microscopy and Microanalysis*, vol. 27, pp. 1026–1034, 2021. doi:10.1017/S1431927621012319

118. H. Balakrishnan, R. Millan-Solsona, M. Checa, R. Fabregas, L. Fumagalli, and G. Gomila, “Depth mapping of metallic nanowire polymer nanocomposites by scanning dielectric microscopy,” *Nanoscale*, vol. 13, pp. 10 116–10 126, 2021. doi:10.1039/D1NR01058A

119. M. Checa, R. Millan-Solsona, A. G. Mares, S. Pujals, and G. Gomila, “Fast label-free nanoscale composition mapping of eukaryotic cells via scanning dielectric force volume microscopy and machine learning,” *Small Methods*, vol. 5, p. 2100279, 2021. doi:https://doi.org/10.1002/smtd.202100279

120. H. T. S. Boschker, P. L. M. Cook, L. Polerecky, et al., “Efficient long-range conduction in cable bacteria through nickel protein wires,” *Nature Communications*, vol. 12, p. 3996, 2021. doi:10.1038/s41467-021-24312-4

121. M. Checa, X. Jin, R. Millan-Solsona, et al., “Revealing fast cu-ion transport and enhanced conductivity at the cuinp2s6–in4/3p2s6 heterointerface,” *ACS Nano*, vol. 16, pp. 15 347–15 357, 2022. doi:10.1021/acsnano.2c06992

122. G. Gramse, M. A. Edwards, L. Fumagalli, and G. Gomila, “Dynamic electrostatic force microscopy in liquid media,” *Applied Physics Letters*, vol. 101, 2012, 213108. doi:10.1063/1.4768164

123. L. Fumagalli, A. Esfandiar, R. Fabregas, et al., “Anomalously low dielectric constant of confined water,” *Science*, vol. 360, pp. 1339–1342, 2018. doi: 10.1126/science.aat4191

124. M. D. Muzio, R. Millan-Solsona, J. H. Borrell, L. Fumagalli, and G. Gomila, “Cholesterol effect on the specific capacitance of submicrometric dopc bilayer patches measured by in-liquid scanning dielectric microscopy,” *Langmuir*, vol. 36, pp. 12 963–12 972, 2020. doi:10.1021/acs.langmuir.0c02251

125. R. Millan-Solsona, M. Checa, L. Fumagalli, and G. Gomila, “Mapping the capacitance of self-assembled monolayers at metal/electrolyte interfaces at the nanoscale by in-liquid scanning dielectric microscopy,” *Nanoscale*, vol. 12, pp. 20 658–20 668, 2020. doi:10.1039/D0NR05723A

126. M. Di Muzio, R. Millan-Solsona, A. Dols-Perez, J. H. Borrell, L. Fumagalli, and G. Gomila, “Dielectric properties and lamellarity of single liposomes measured by in-liquid scanning dielectric microscopy,” *Journal of Nanobiotechnology*, vol. 19, p. 167, 2021. doi:10.1186/s12951-021-00912-6

127. M. Checa, R. Millan-Solsona, A. Glinkowska Mares, S. Pujals, and G. Gomila, “Dielectric imaging of fixed hela cells by in-liquid scanning dielectric force volume microscopy,” *Nanomaterials*, vol. 11, 2021. doi:10.3390/nano11061402

128. A. Kyndiah, M. Checa, F. Leonardi, et al., “Nanoscale mapping of the conductivity and interfacial capacitance of an electrolyte-gated organic field-effect transistor under operation,” *Advanced Functional Materials*, vol. 31, p. 2008032, 2021. doi:10.1002/adfm.202008032

129. A. B. Naden, J. Loos, and D. A. MacLaren, “Structure–function relations in dif-tes-adt blend organic field effect transistors studied by scanning probe microscopy,” *Journal of Materials Chemistry C*, vol. 2, pp. 245–255, 2014. doi:10.1039/C3TC31783H

PART II

METHODS

Chapter 2

In-Liquid Scanning Dielectric Microscopy on EGTs

Abstract This chapter presents the improvements and key developments made in the earlier implementation of in-Liquid SDM on electrolyte-gated transistors, which was discussed previously in subsection 1.6.4. The data acquisition and analysis of in-Liquid SDM implementation on EGTs is automated for a comprehensive exploration of devices in various operating regimes. An easy and efficient approach for data analysis, representation, and curation of nanoscale electrical data is introduced that corrects high-frequency artefacts in the measurements. The data representation of mechanical data is also discussed. A new potential mapping method is introduced based on in-liquid SDM applied to EGTs that provides quantitative local electric potential maps in different operating regimes directly from raw experimental data without any need for calibration or finite element simulations.

2.1. Improved & Advanced in-Liquid SDM Implementation on EGTs

Electrolyte-gated transistors present a challenge for their integration into a conventional atomic force microscopy (AFM) setup for characterization due to specific spatial and technical requirements. Therefore, they demand special attention on instrument and technique development.

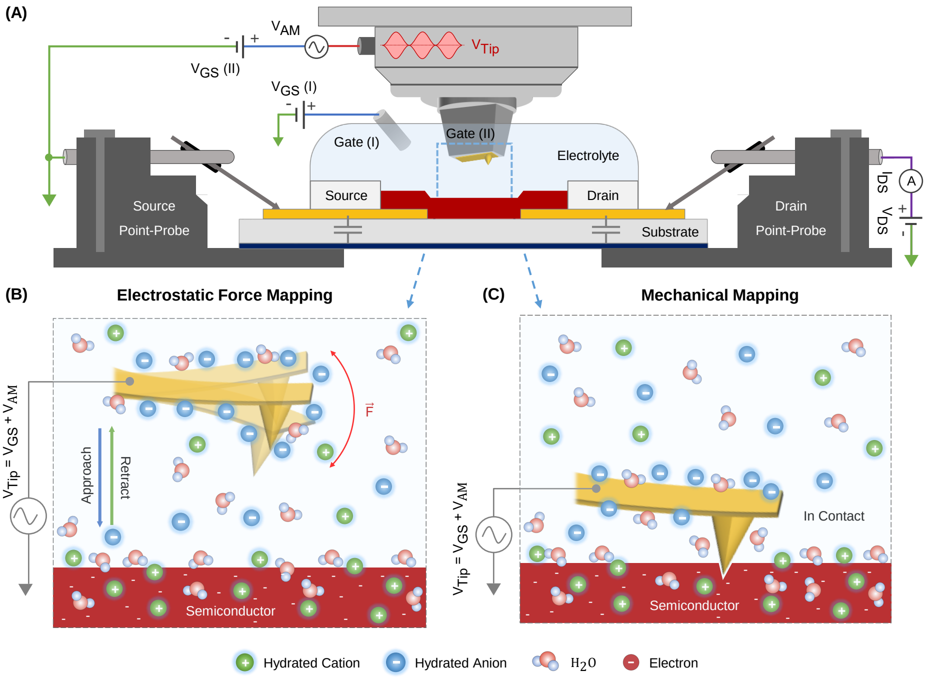

Figure 2.1: Schematic of (A) In-Liquid SDM implementation on electrolyte-gated transistor performing (B) electrical, and (C) mechanical mapping.

In the work of this thesis, we further developed an existing adaptation of in-Liquid SDM on EGOFET which was discussed earlier in subsection 1.6.4. A standard AFM system (JPK Nanowizard BioAFM) is coupled with external power sources and instruments to bias the transistor during imaging with a newly developed custom sample holder containing point probes for stable and reproducible connections, as schematically shown in Figure 2.1A and photographically in Appendix A (Figure A.1 and Figure A.2A). Using the standard point probes with appropriate modifications in the design for connections instead of silver paste and adhesives has made the measurements more stable and plug-and-play style connections, which is the foremost requirement for long-time reproducible AFM measurements; also, these connections are more immune to interferences from external electrical noises like the 50Hz AC line. Here we have avoided using the silver paste or other adhesives for making connections to the contact pad on the transistor device as was done earlier (see Appendix A Figure A.3) since it could lead to contamination and also would not allow performing the cleaning/washing of the transistor surface easily if required once such permanent connections are made.

The high-frequency electrical connection to the AFM tip is also optimized by creating customized solutions for wires and connectors while minimizing the ground loops as much as possible, as shown in Appendix A Figure A.2B, which enabled very stable and robust connections up to few 100s of MHz frequencies (extending the existing range that achieved only upto 30 MHz).

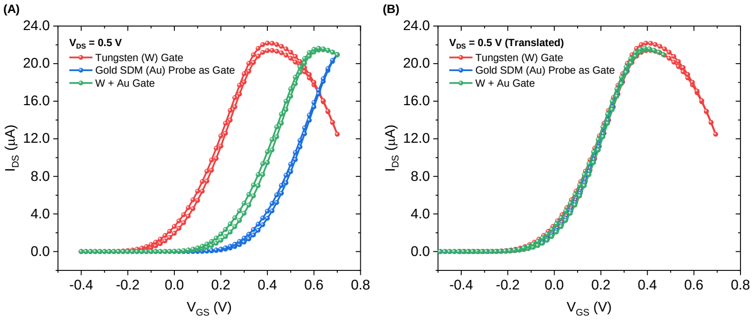

Figure 2.2: (A) Transfer characteristics of an EGT with an external gate (Tungsten), another with the gold SDM probe and another with both of these gates simultaneously where the DC gate voltage is applied from the same power source to the junction connecting both SDM probe and external gate electrode together. (B) The transfer curves shown in (A) are translated horizontally to show that the intrinsic performance is the same only the threshold is shifted.

Another difference with respect to the previous implementation discussed in subsection 1.6.4 is that in the current setup, as shown in Figure 2.1, we have introduced an external gate as well along with using SDM probe as a gate. The rationale behind this approach is to allow the flexibility of using the external gate electrode of any material to gate the transistor and not be limited by the availability of an appropriate AFM cantilever as in the previous implementation. The dual gate setup shifts the threshold voltage without affecting the intrinsic performance (or stability) of the semiconducting material, as shown with the help of transfer curves in Figure 2.2. The respective individual thresholds are determined by the difference in the gate metal electrode work function[1] and the semiconductor surface work function as well as their respective capacitances[2,3]. As we see, the dual gate combination settled the threshold somewhere in between, which probably also depends on their relative contributions.

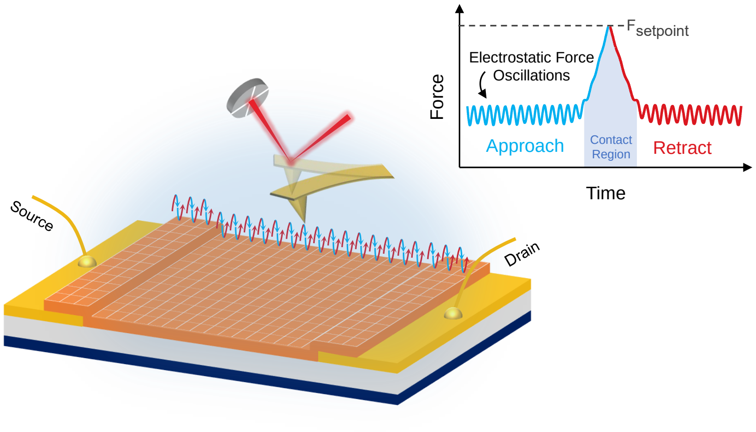

Figure 2.3: Schematic illustrating force volume data acquisition mode where at each pixel a force-distance approach-retract curve is taken. The approach and retract curves depicted show oscillations due to electrostatic forces between the tip and sample caused by applied amplitude-modulated waveform.

The in-Liquid SDM scanning is performed in force volume mode as illustrated in Figure 2.3 where at each pixel, a force-distance approach-retract curve is taken from which electrical images can be constructed by plotting them at a particular distance either in constant height mode (where the distance is maintained constant with respect to the substrate, i.e. the resulting image is taken in a plane parallel to the substrate) or lift mode (where the distance is maintained constant with respect to the sample surface, i.e. the resulting image is taken in a lifted surface which follows the topography of the sample surface). In the force recordings, the oscillation amplitude and deflection of the probe are measured simultaneously. When approaching the sample the oscillation amplitude increases as well as the static bending (not visible in the schematic approach curve since a zoomed region is shown to highlight the contact part), until contact is made with the sample, in which case the oscillation amplitude is quickly reduced and the static bending greatly increases as shown in the schematic.

The force volume mode presents a significant advantage that it can probe the local electrical properties when in non-contact while approaching (as shown in Figure 2.1B) and local mechanical properties when in contact with the semiconductor surface (as shown in Figure 2.1C). It gives the multimodal modal nature to the measurements and allows us to investigate the material's response from a broader perspective. The two modalities are probed approximately simultaneously at each pixel. The time difference is very small since the whole approach curve of 3000nm takes only 75ms, and we generally plot the electrical images at 100nm from the surface, which would translate to a time difference of only 2.5ms (not considering the indentation time as it varies depending on the set-point and sample).

2.1.1. Python Automation

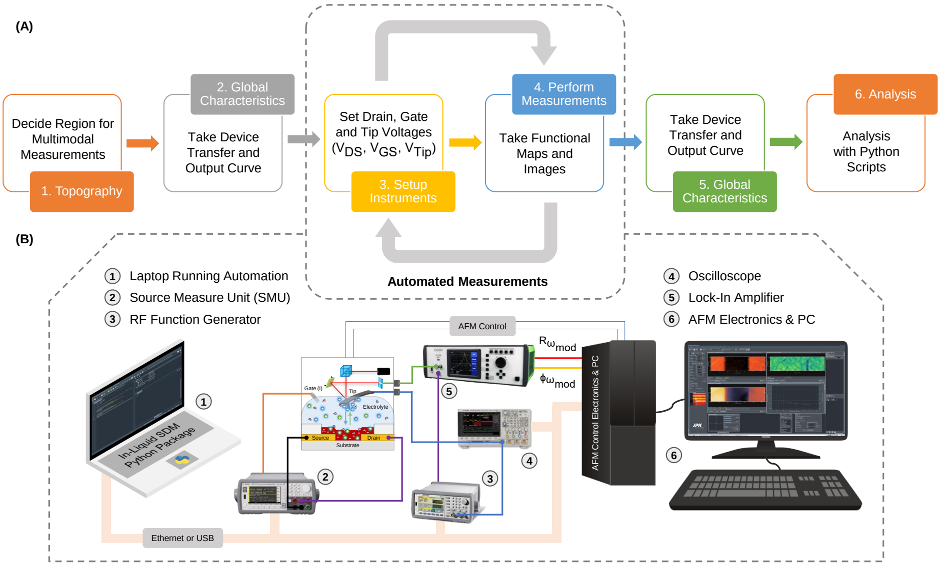

Figure 2.4: (A) A typical measurement protocol with automated data acquisition workflow for successive measurements at different drain and gate voltages. (B) The network indicating connections among various instruments, AFM PC and a laptop running Python automation scripts.

For comprehensive characterization of EGTs and also to establish in-liquid SDM as a preferred tool for multiscale and multimodal measurements, the experimental data acquisition and analysis is automated and standardized for reliable and reproducible work. Automation not only helps in comprehensive measurements but also enables the recording and documentation of various experimental parameters in a consistent fashion. With automation, we can document all measurement parameters and also other additional parameters by performing secondary measurements on external signals and thereby capturing the whole experiment in detail, and later it would also allow doing experimental checks on things which otherwise would go unnoticed, as highlighted later in subsection 2.1.2.

The sequence of operations involved in a typical in-operando SDM experiment acquiring a set of functional maps and images is highlighted in Figure 2.4 and described below (not considering the steps involved in the preparation of the experimental setup and adjustments in AFM) :

1. Decide the region where multimodal measurements need to be performed. This step usually involves performing some topographic and electrical images in different regions to make sure that the finalized region is representative of the whole device.
2. Take the transfer and output curve of the device before starting the electrical imaging. These curves are taken for comparison later with reconstructed curves from the drain current recording during operando measurements and also with the I-V curves taken at the end of all measurements to make sure that the device had stable characteristics during the whole measurement period. This step is sometimes skipped if the measurements are to be performed starting from the pristine conditions i.e. without any prior applications of voltages, such as the one done for OECTs in Chapter 4.
3. Perform automated measurements at different drain and gate voltages. The sub-sequence of automated operations are:
    i. Apply DC bias voltages (gate and drain voltage) to EGT and amplitude-modulated waveform with DC offset (gate) voltage to the SDM probe. Also, measure the applied voltages to the tip with the oscilloscope.
    ii. Wait a set time for the EGT to reach a steady state (this time is determined from other measurements of drain current time evolution at fixed biases)
    iii. Approach the SDM probe on the Surface of the EGT
    iv. Wait a set time
    v. Start the scanning to record approach curves at each pixel

   vi. Once finished retract the tip
   vii. Wait a set time
   viii. Turn off all voltages and save the drain current recorded in a file
   ix. Save the electrical image with the appropriate label
   x. Plot and perform preliminary data analysis

4. Take the transfer and output curve of the device
5. Perform comprehensive analysis of the whole data set with Python scripts.

Understanding the operating mechanism of devices across various regimes necessitates exploring a wide range of drain and gate voltages. Manually, a researcher can do so only at a few select voltages (a few 10s) in a workday due to the intense user operations and interventions required as described above to get one image, and it increases in multiples as the number of voltages to explore increases. The automated routines implemented in Python take care of all the user operations defined in step 3 except for occasional instances to adjust the scan region in case of drifts in the system, and now 100s of images can be taken in a day giving approximately a 10-fold increase in data and productivity.

The automation is implemented in Python instead of using any virtual instrument engineering workbench so to keep the development open-source and not rely on third-party proprietary software. A custom Python package named *"inLiquidSDM"* is developed, which handles the communication between different instruments (JPK BioAFM, SMU, RF Generator, Lock-In Amplifier and Oscilloscope) and saves the dataset with appropriate labels and plots it for preliminary analysis. The developed Python package has different modules for different operations and can be executed in any feasible order according to the experiment's requirement providing flexibility and reusability of codes. A set of dedicated data analysis scripts are also developed which performs extended data analysis to extract many parameters and pieces of information. The link to the GitHub repository hosting *inLiquidSDM* Python package with some further information is provided in Appendix B.

The development of such experimental setups and techniques is, therefore, indispensable for advancing the field of bioelectronics as it enables simultaneous probing of relevant nanoscale electrical and mechanical signatures of the operating electrolyte-gated transistors like EGOFET and OECT, as detailed in Chapter 3 and Chapter 4 respectively.

2.1.2. Correction of High-Frequency Artefacts

The EGT exhibits dynamic electrical behaviour as a function of applied drain and gate voltages, representing a dynamic impedance between the SDM probe and the whole transistor, and thus this behaviour must be taken into account when applying high frequencies (in the 10s of MHz range) as it can lead to variations in the total applied AC tip-sample voltage which is generally assumed constant. The AC tip-sample voltage can also have spatial variability as the probe traverses the source-channel-drain region, which leads to measurement artefacts that appear as a slope in the acquired image or highly asymmetric force on source and drain even for zero applied source-drain voltage.

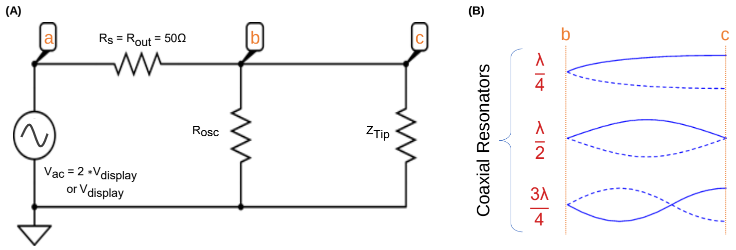

Figure 2.5: (A) Circuit schematic of connection from RF source (v_{ac}) to Tip (Z_{Tip}) via oscilloscope (R_{osc}). R_s or R_{out} is the RF source output impedance. (B) Illustration of coaxial Resonance in coax between oscilloscope and tip (considering R_{osc}=R_s).

To grasp why high-frequency tip-voltage change occurs, we look at the schematic of the electrical circuit of tip connection with the RF source, as shown in Figure 2.5A. As a side note, the approach used in this thesis puts an oscilloscope with 50Ω input impedance setting in between the tip and RF source so as to keep the DC offset (gate) voltage level the same as indicated on the display of the RF generator. Otherwise, without it, with a typical output impedance setting of 50Ω on the RF generator, the actual DC gate voltage will be almost double due to the design of these RF generators (see reference [4]), causing loading effects as the tip-sample junction is a high impedance load at DC. Coming back to our initial question, the Z_{Tip} is not 50Ω so the reflection of the electrical signal will happen due to operation at high frequencies leading to the formation of standing waves between the oscilloscope and tip, which finally modifies the potential reaching the tip. The standing wave pattern and the potential reaching the tip depend also on the tip-sample impedance and thereby, with dynamic tip-sample impedance the tip voltage will change.

There is also the role of what frequency is applied in relation to the cable lengths used and other parasitic capacitances[5]. At some special specific frequencies or wavelengths in multiples of one-fourth of the effective cable length ($\lambda/4$), resonance will occur as shown in Figure 2.5B. We can use these resonances ($\lambda/4$ and $3\lambda/4$) to maximize the high-frequency signal strength at the tip, which can be found either by doing electrical imaging at different frequencies or by looking at the oscilloscope signal, which in such cases will measure the lowest peak-to-peak amplitude around this resonance frequency as mentioned later in this section. Nonetheless, the voltage at the tip will change as the transistor channel conductivity changes as the RF source will see a changing effective load impedance, with the magnitude change depending on the transistor size and the ionic strength of the electrolyte solution.

Previous approaches of in-Liquid SDM such as the one discussed in subsection 1.6.4, addressed this issue through a renormalization factor determined by fitting an approach curve taken on the metal for far away distances and imposing the geometric parameters (especially the cone half angle) of the tip as indicated by the manufacturer[6]. However, the results and analysis which are shown below mandate different factors for each approach curve within an image and for every image, which makes the renormalization approach impractical as there are more than 300,000 curves (for a typical 64x16 pixel image and a total of 300 images taken in a single dataset using automation). However, while fitting the data with finite element simulations, the results are slightly immune as the variation is absorbed by other unimportant fitting parameters[6]. Nonetheless, qualitative analysis is impossible without correcting this factor.

To see this artefact in action, Figure 2.6 shows the changes in the recorded local electrical signal (electrostatic force - uncalibrated raw signal) on an EGT in different configurations of the electrical ground connection of the high-frequency signal. In case (A), the tip voltage is referenced with respect to the source electrode, and in this condition, the electrical profile shows that the signal at the

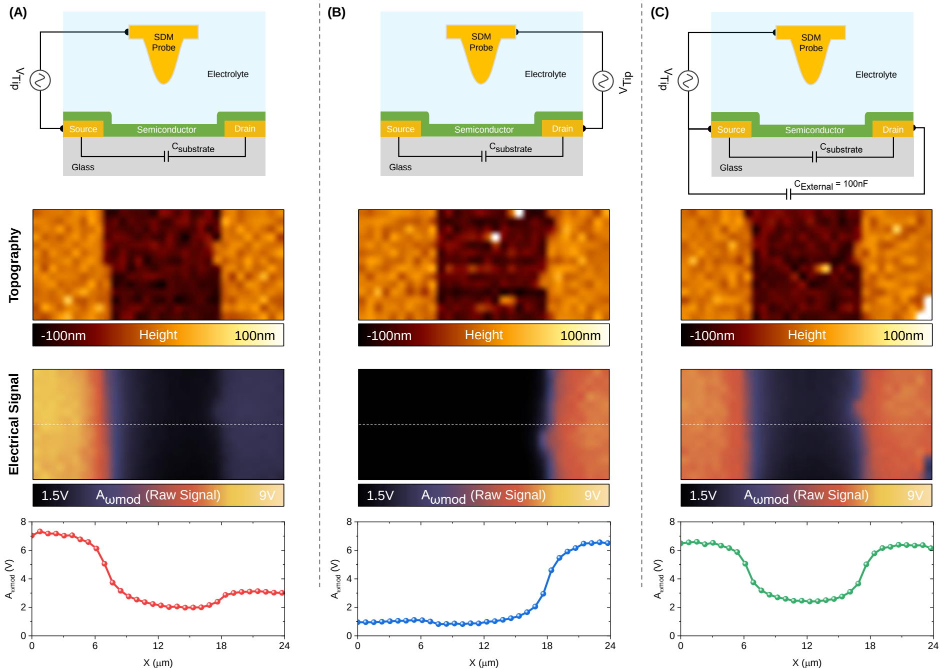

Figure 2.6: (A-C) Electrical images (electrostatic force - uncalibrated raw signal $A_{\omega mod}$) in different configurations of the ground connection of high-frequency signal along with profiles across the images. The corresponding topographies are also shown.

source is higher. When we move to the case in (B), the profile is approximately the mirror image of the one in (A), where the drain shows a higher signal. This asymmetry is because of the change in ground reference which impacts spatially the voltage drop of the high frequency in the electrolyte. Putting an external capacitor ($C_{External} = 100nF$) as shown in (C), effectively acts as a short between the source-drain electrodes at high frequencies (in 10s of MHz) which restores the symmetry. Putting an external capacitor makes the tip voltage the same for the locations on the source and drain but not for the channel, however, it will increase the signal-to-noise ratio by symmetrically distributing the high frequency as we can see from the channel region. So, we keep the external capacitor in our measurements, it does not affect the applied bias voltages as the measurements are done in steady DC voltage conditions.

The measurements shown previously are done at one frequency, but what happens when we change the high frequency systematically with our developed automation

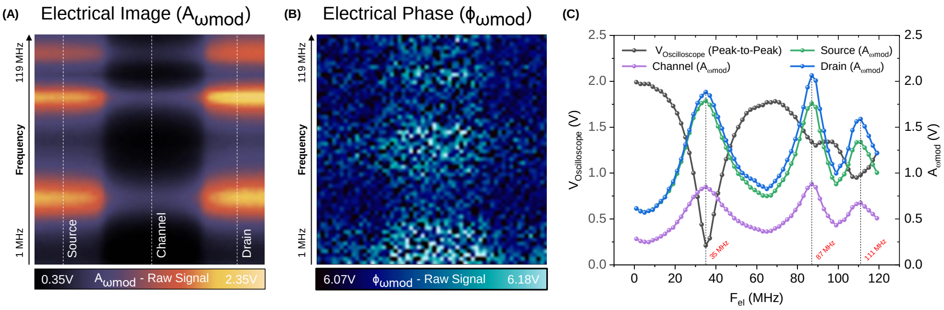

Figure 2.7: (A) Electrical image spectrum (raw $A_{\omega mod}$ signal) of a cross-section of the transistor where at each scan line the applied high frequency is changed by +2MHz starting from 1 MHz and ending at 119 MHz using the developed automation. (B) Electrical phase image (raw $A_{\phi mod}$ signal) for the same as in (A). Graph showing vertical profiles highlighted in (A) for the source, channel and drain region along with the recorded oscilloscope voltage (see Figure 2.5 for the location of the oscilloscope).

to capture the trend fully? Figure 2.7 shows the measurements done in the configuration shown in Figure 2.6C with changing high frequencies at each scan line from 1MHz upto 119MHz. As we can see from the images, the signal recorded is a function of frequency, where the signal maximizes at coaxial resonance frequencies as discussed earlier in Figure 2.5. The automation script additionally records the signal at the oscilloscope with its built-in peak-to-peak measure function, which allows performing an experimental check to determine whether our understanding is correct. The oscilloscope signal decreases when the local electrical signal peaks as shown in Figure 2.7C, which matches our expectation. So, for our measurements, we use one of the frequencies at which the signal peaks to maximize the signal-to-noise ratio.

As we saw, we maximized the signal spatially by putting an external capacitor and globally by using the appropriate high frequency but it did not correct the tip-voltage artefact. This will especially be an issue as we apply different drain and gate voltages, where each image will have a different tip-sample AC voltage when significant changes in tip-sample impedance happen, besides the spatial variation seen earlier. To tackle this, we go back to the basics and look at the equation of the electrostatic force ($F_{elec}(z,t)$) below:

$$F_{elec}(z,t) = \frac{1}{2}\frac{dC_{sol}(z)}{dz}v^2{}_{sol}(z,t) \tag{2.1}$$

where $v_{sol}(z,t)$ is the AC potential drop in the solution and $dC_{sol}(z)/dz$ is the capacitance gradient of the solution capacitance, which is the constant of the system. This should not be confused with typically plotted $dC(z)/dz$, where C(z) is the total tip-sample capacitance function, and in the above relation, instead of $v_{sol}(z,t)$ we use total tip-sample voltage v_{ac}, assuming the equivalence in the resulting force either way.

If an unintended change in voltage occurred such that one has a change in the voltage drop in the solution, $v'_{sol} = k \cdot v_{sol}$, where k is a constant assumed independent of z and t (at least at the timescale of taking an approach curve), then

$$F'_{elec}(z,t) = k^2 \cdot \frac{1}{2}\frac{dC_{sol}(z)}{dz} v^2{}_{sol}(z,t) \tag{2.2}$$

If we plot relative change in electrostatic force at a near tip-sample distance with respect to a far away tip-sample distance, then we have

$$\begin{aligned} \frac{\Delta F'}{F'} &= \frac{F'_{elec}(z_{near}) - F'_{elec}(z_{far})}{F'_{elec}(z_{far})} \\ &= \frac{\cancel{k^2} \cdot \frac{1}{2}\frac{dC_{sol}(z_{near})}{dz} v^2{}_{sol}(z_{near},t) - \cancel{k^2} \cdot \frac{1}{2}\frac{dC_{sol}(z_{far})}{dz} v^2{}_{sol}(z_{far},t)}{\cancel{k^2} \cdot \frac{1}{2}\frac{dC_{sol}(z_{far})}{dz} v^2{}_{sol}(z_{far},t)} \\ &= \left[\frac{\Delta F}{F}\right]_{True\ Value} \end{aligned} \tag{2.3}$$

As we see the relative change preserves the true relation and effectively removes the tip voltage change artefact. Therefore, considering the relative change instead presents a very easy and straightforward way to remove the tip-voltage artefact.

To demonstrate the power of this simple change, Figure 2.8A and Figure 2.8B shows the capacitance gradient of the dataset taken in the configuration shown in Figure 2.6A without an external capacitor for different drain and gate voltages to cover linear and saturation regime. Figure 2.8C and Figure 2.8D shows the corresponding delta capacitance gradient and Figure 2.8E and Figure 2.8F shows the corresponding relative capacitance gradient with a reference far away distance of $z_{far} = z_{ref} = 1500nm$. The trends shown are the averaged profiles in the vertical direction in a single image taken at the defined drain and gate voltage, whereas

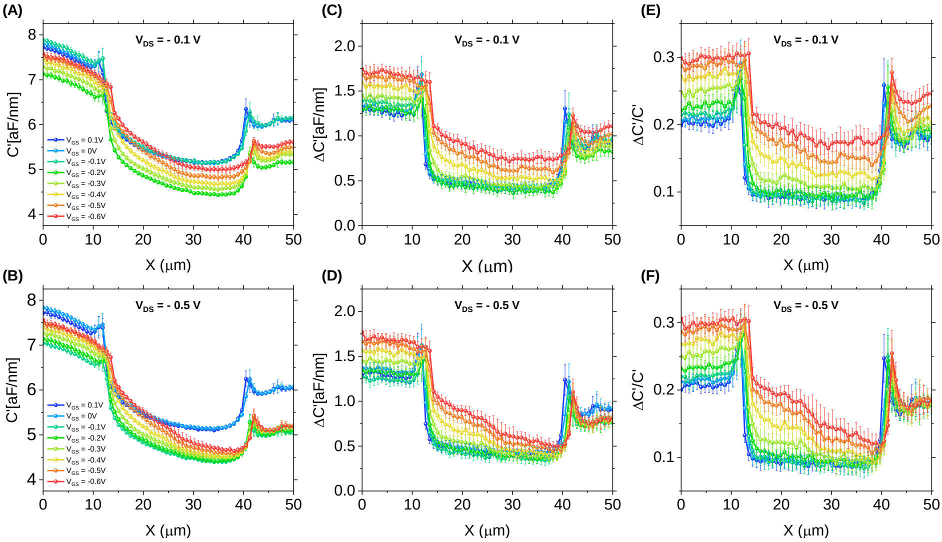

Figure 2.8: Another example showing how considering the relative variation removes the tip voltage change artefact. (A) Capacitance gradient (C'), (D) Delta capacitance gradient ($\Delta C'$), and (C) Relative capacitance gradient ($\Delta C'/C'$) at $Z_{lift} = 100nm$ profiles spanning source-channel-drain region at $V_{\text{DS}} = -0.1V$. Similarly (D-F) are for $V_{\text{DS}} = -0.5V$. The full dataset with images is shown in Chapter 3 Figure 3.9.

error bars are the standard deviation (see Figure 3.9 for images). As we see from this dataset, taking the delta change has taken the big portion of asymmetry but still has not corrected completely (notice the blue curve in Figure 2.8E), but by considering the relative change, the trends are what one would expect in a linear and saturation regime (refer Chapter 3). The relative change has effectively removed the tip voltage change artefact. As a side story, after seeing this raw data we thought I did some mistake in the experiment as this data was taken at the very beginning of my PhD and we have kind of discarded this dataset. Only after realizing the tip-voltage change artefact, and finding a very simple solution to correct it, I could reuse this dataset now as the supporting data for this whole process (an important lesson indeed; never discard your dataset!).

To show that even using the configuration shown in Figure 2.6A, the tip voltage artefact remains, Figure 2.9 shows the measurements and similar analysis for a wide range of drain and gate voltages (for the complete dataset refer Figure 3.7). Here instead of the image profiles, we have plotted trends in a transfer-curve fashion for source, channel and drain, giving us the local electrostatic force versus

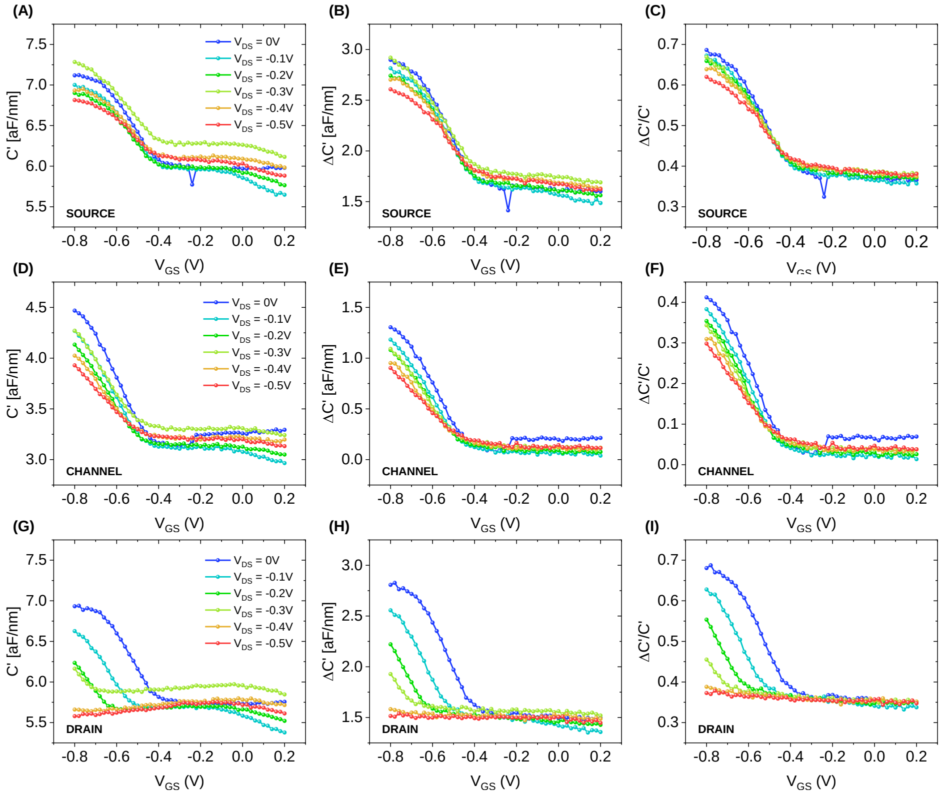

Figure 2.9: (A) Capacitance gradient (C'), (D) Delta capacitance gradient ($\Delta C'$), and (C) Relative capacitance gradient ($\Delta C'/C'$) at $Z_{lift} = 100nm$ (and $Z_{ref} = 2000nm$ for relative) for the location on Source. (D-F) shows the same for Channel and (G-I) shows the same for Drain. The full dataset with images is shown in Chapter 3 Figure 3.7.

gate voltage transfer curves. As we see, the capacitance gradient graphs do not show a particular trend, only when plotting the relative variation we see the trend very clearly, reiterating the observation made earlier. The corresponding oscilloscope voltage recordings are shown in Figure 2.10, we do see the variations which are indirectly reflecting the changes in the tip-voltage (there is an anti-correlation), but due to the complex nature of the system, they are not easy to decipher (the discrete nature of the data is due to the resolution of the measure function in the oscilloscope which depends on the voltage/division scale settings). As a remark, if we take the smoothed variation in this recording and try to model the system with the circuit in Figure 2.5 and use the corresponding functional relation between the oscilloscope recording and tip voltage, a correction to some degree can be achieved, but this is not practical at all to do for every approach curve and neither reliable as the recorded oscilloscope voltages give the global averaged trend only.

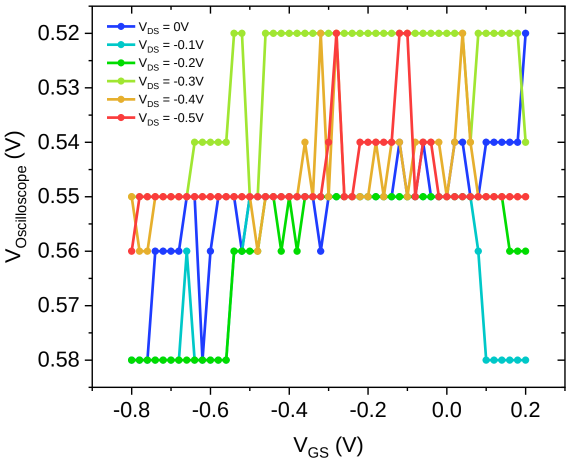

Figure 2.10: The recorded oscilloscope voltages at different drain and gate voltages for the measurements done at $\lambda/2$ coaxial resonance corresponding to the data shown in Figure 2.9. The discrete nature of the data is due to the resolution of the measure function in the oscilloscope which depends on the voltage/division scale settings.

There is another significant advantage in the use of the relative variation of the electrostatic force, namely, there is no need to perform any calibration of the electrical raw data. We can directly take the relative variation of the measured raw data ($A_{\Omega mod}$). This has effectively removed reliance on knowing many parameters/factors that go into calibrating the data, which are the cantilever spring constant (k), AFM optical system deflection sensitivity (s), lock-in amplifier gain (G), applied AC potential amplitude (v_{ac}), and the renormalization factor (α). The calibration equation generally used[6] is

$$\left.\frac{dC}{dz}\right|_{exp} = \alpha \frac{8k\left(A_{\Omega mod} - A_{\Omega mod,off}\right)s}{\left(v_{ac}\right)^{2}G} \tag{2.4}$$

where, $A_{\Omega mod,off}$ is the lock-in offset if present, which is a constant.

The list of advantages of considering the relative variation does not end here. Based on all the previous observations, we have come up with a method which enables direct quantitative local electric potential mapping in an operating device in liquid from the raw data without any use of finite element simulations, representing a huge advantage. This approach effectively circumvents the limitations of conventional KPFM in aqueous electrolytes for the case of materials showing a voltage-dependent variation of their conductivity and is discussed in section 2.3.

2.2. Multimodal Data Representation

This section describes the way of data representation for the electrical data (which follows from the observations made in the earlier section) and for the mechanical data recorded in a typical in-liquid SDM measurement.

2.2.1. Electrical Data Representation

After all the results and discussions presented in subsection 2.1.2, relative electrostatic force variation (same as the relative variation in the recorded raw data) are considered throughout the thesis, otherwise explicitly specified. The relative variation accurately captures the variation in the true signal, as follows from Equation 2.3, and thus defines a correct approach for electrical data representation.

2.2.2. Mechanical Data Representation

In a typical in-liquid SDM measurement both the static deflection of the cantilever and its oscillation amplitude at the frequency of the voltage amplitude modulation are measured simultaneously.

The static deflection approach curve (specifically the indentation part of the approach curve) taken during a typical in-liquid SDM measurement presented here provides access to the mechanical properties of the local state of the semiconductor. The mechanical properties are more relevant in the case of OECTs than EGOFET as they present dynamic changes as a function of applied bias potentials due to the penetration of ions into the bulk of the semiconductor, as discussed in Chapter 1 subsection 1.4.2. Therefore, they are discussed in detail only in the chapter corresponding to OECTs (Chapter 4).

An example approach curve during in-liquid SDM on an n-type BBL OECT at a high doping state ($V_{\mathrm{GS}} = 0.8V$) is shown in Figure 2.11 after performing the

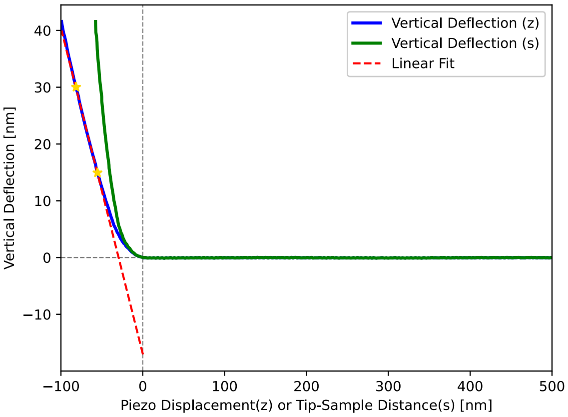

Figure 2.11: Approach curve on the source during in-liquid SDM on an n-type BBL OECT at a high doping state ($V_{GS} = 0.8V$). The same x-axis is used to plot the vertical deflection with respect to piezo distance (z: blue curve) and tip-sample distance (s: green curve). A slope in the linear part of the indentation region of the blue curve is extracted between two predetermined points (yellow stars). The vertical deflection is calibrated by multiplying the photodiode signal with the AFM cantilever deflection sensitivity (s) determined by the thermal noise-based contact-free calibration method in the AFM control software.

necessary processing steps such as baseline correction, contact point determination, removal of laser interference and electrostatic force oscillations using developed Python scripts. The deflection in nanometers is obtained after multiplying the raw photodiode vertical deflection signal (in volts) with the deflection sensitivity (s) of the cantilever (in nm/V) determined by the thermal noise-based contact-free calibration method in the AFM control software. The same x-axis is used to plot the vertical deflection with respect to piezo distance (z: blue curve) and tip-sample distance (s: green curve). The indentation part is fairly linear at intermediate deflections or setpoint forces (yellow stars). At these indentations, the sample can be considered a Hookean spring i.e. linear elastic. In this case, an effective spring constant (N/m) of the sample (k_{sample}) can be calculated from the slope of this linear region (dashed red line) of the vertical deflection (in nm) versus the piezo displacement (in nm) curve (blue curve), given by[7]

$$k_{sample} = k_{cantilever}\left(\frac{m}{1-m}\right) \tag{2.5}$$

where, $k_{cantilever}$ is the cantilever spring constant and m is the slope of the linear region (unitless: nm/nm).

The thickness of the semiconducting polymer studied changes significantly from the air ($\approx 25nm$) to pristine condition in the undoped state ($\approx 36nm$) and then to the doped state ($\approx 83nm$) as discussed later in Chapter 4. Also, as we see later, the top part of the polymer is more hydrated than the bottom bulk part in the initial hydration cycle of the polymer. In such a case, the top part is very soft, and the bottom part of the polymer is stiffer, as can be seen from the non-linear part in the low indentation region in Figure 2.11 for the vertical deflection versus tip-sample distance curve (green curve), where tip-sample distance is obtained after subtracting the vertical deflection from the piezo displacement. For such kind of dynamics, if we want to quantify based on Young's modulus, besides considering the thickness change, we also have to consider the so-called *Bottom-Effect Artifact*[8] of the hard substrate due to the comparable thickness of the polymer with the contact radius of the probe on the surface. The contact radius is given by $\sqrt{\delta R}$, where δ is the indentation and R is the tip radius[8]. The nominal value of the tip radius of the probe used (HQ:NSC19/Cr-Au) for in-liquid SDM is below 35nm. The bottom effect correction is applied on top of the standard Sneddon's model and for a paraboloidal tip geometry it reads[9]

$$F_{Sneddon} = \frac{4}{3} E_{eff} \sqrt{R} \delta^{3/2} \tag{2.6a}$$

$$F_{corrected} = F_{Sneddon} \left[1 + \frac{1.133\sqrt{\delta R}}{h} + \frac{1.497\delta R}{h^2} + \frac{1.469\delta R\sqrt{\delta R}}{h^3} + \frac{0.755(\delta R)^2}{h^4} \right] \tag{2.6b}$$

The thickness that goes into the above equation depends on whether we want to quantify the soft top part of the polymer or the hard bottom part. For the hard part, we can use the total thickness but for the soft top part of the polymer, the bottom hard part acts as the surface and enhances the bottom effect further, so, we have to take the thickness of only the top part. From the force curves, we can make a rough estimate based on the linear fitting of the high indentation part of the vertical deflection versus the tip-sample distance curve and take the (negative of) x-axis intercept of this linear fit as the thickness of the top part of the polymer for quantification.

However, following any of the methods described previously whether by calculating the effective spring constant of the sample or quantifying by the Hertz model or quantifying by correcting the bottom effect and considering the constant thickness or quantifying by considering the varying thickness of the top part or by just plot the slope of the vertical deflect versus piezo displacement (m), they all capture the underlying trend where the difference comes from the nature of quantification.

Therefore for simplicity, as a first approximation, we consider the simplest of these methods for the mechanical data representation which is by reporting the mechanical slope m along with the deflection sensitivity (s) of the cantilever for qualitative interpretation as the focus is on understanding the operating mechanism. The slope m is always less than or equal to 1 within the measurement noise level (if no repulsive interactions are present); less than one means the sample is soft and equal to one within the measurement noise level means that the same is hard for the given cantilever. The slope depends on the cantilever spring constant as well besides the sample effective stiffness, as expected from Equation 2.5, rewritten as $m = k_{sample}/(k_{sample} + k_{cantilever})$. Therefore, within the same dataset, comparison can be made directly, but for comparing different datasets, conversion to effective k_{sample} is needed.

2.3. Local Potential Mapping of Operating Semiconductor Devices

The local electrostatic force measured by in-liquid SDM in operating transistors shows a dependence on both the gate and drain voltages. The relative capacitance gradient variation plotted for the data showed earlier in Figure 2.9 clearly reveals this trend. A careful observation of Figure 2.9(C, F and I), gives an impression that the data seems to be dependent on the local potential. It is more clear for the drain that the data shifts almost by the same amount as the applied drain voltage. This opens the possibility of mapping the local electric potential in the operating semiconductor device.

The essence of the underlying approach is that the measured local (relative) electrostatic force depends on the local conductivity, which in turn depends on the local potential. By using this composite relation, we can quantify the local potential. Specifically, we assume

1. The local electrostatic force at a given (x,y) position is univocally determined by the local semiconductor sheet conductivity to a good approximation, i.e.,
$$F_{elec}(x,y,z;V_{\mathrm{GS}},V_{\mathrm{DS}}) = F[\sigma(x,y;V_{\mathrm{GS}},V_{\mathrm{DS}}),z] \tag{2.7}$$
2. The local conductivity in the on-state at non-zero V_{DS} can be related to a good approximation to the conductivity function at zero source-drain voltage evaluated at the local effective gate voltage, $V'_{\mathrm{GS}} = V_{\mathrm{GS}} - V(x,y)$, i.e.,
$$\sigma(x,y;V_{\mathrm{GS}},V_{\mathrm{DS}}) = \sigma_0(x,y;V_{\mathrm{GS}} - V(x,y;V_{\mathrm{DS}})) \quad V_{\mathrm{DS}} \neq 0; \tag{2.8}$$

where, $V(x,y)$ is the local potential drop along the channel at position (x,y) for the given V_{GS} and V_{DS}, and for $V_{\mathrm{DS}} = 0$, $V(x,y) = 0$.

Under these assumptions, we have

$$F_{elec}(x,y,z;V_{\mathrm{GS}},V_{\mathrm{DS}}) = F_{elec,V_{\mathrm{DS}}=0}(x,y,z;V_{\mathrm{GS}} - V(x,y;V_{\mathrm{DS}})) \tag{2.9}$$

i.e., the local electrostatic force measured at a given position (x,y) and bias potentials (V_{GS} and V_{DS}) is equal to the local electrostatic force measured at the same position for $V_{\mathrm{DS}} = 0$ and at the local effective gate potential $V'_{\mathrm{GS}} = V_{\mathrm{GS}} - V(x,y)$. Therefore, the local electric potential $V(x,y)$ at a given V_{GS} and V_{DS} can be obtained by comparing the (relative) electrostatic force measured at these voltages with those measured for $V_{\mathrm{DS}} = 0$ and identifying the gate potential shift that makes them equal. A Python algorithm is implemented to find this potential shift for all pixels in the device, which is available with the developed *inLiquidSDM* Python package in Appendix B. This algorithm can be implemented for the local relative electrostatic force versus gate voltage transfer curves obtained for a fixed z and defined z_{ref} such as in Figure 2.9 or considering the full relative electrostatic force approach curve at varying z created for a defined z_{ref}. The full approach curve method is more robust against experimental noise. Nonetheless, Figure 2.12 shows the working of the algorithm for local relative electrostatic force transfer curves. For the implementation using the full approach curves, refer Chapter 3 subsection 3.2.3.

Figure 2.12 shows the process for finding the local potential at $V_{\mathrm{GS}} = -0.6V$ and $V_{\mathrm{DS}} = -0.1V$ (operating point) from the local electrostatic force versus gate

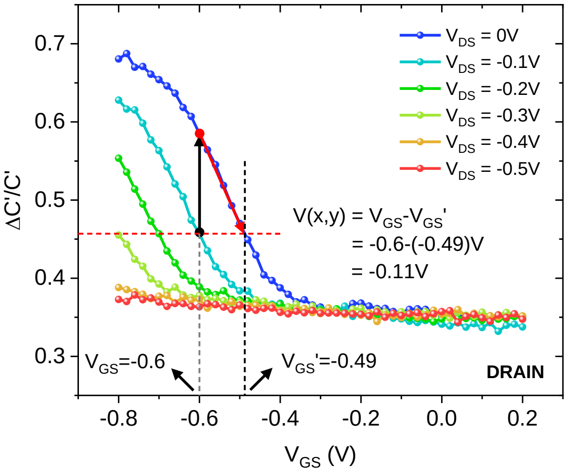

Figure 2.12: Illustration of the working of the potential mapping algorithm at $V_{GS} = -0.6V$ and $V_{DS} = -0.1V$ implemented using the local electrostatic force versus gate voltage transfer curves for the drain pixel taken from Figure 2.9I.

voltage transfer curves for the drain pixel taken from Figure 2.9I. The value of the relative electrostatic force at the given operating point is matched with the values from the $V_{DS} = 0V$ curve. If at the operating point, we remove the drain voltage, we move up following the black arrow, then from there, we go down following the red arrow with decreasing magnitude of gate voltage till we match with the relative electrostatic force obtained at the starting operating point (dashed red line). The gate voltage at $V_{DS} = 0$ at which we find the match is the local effective gate potential (dashed black arrow at $V_{GS} = -0.49V$). From this, we can find the local potential by $V(x,y) = V'_{GS} - V_{GS} = -0.6 - (-0.49)V = -0.11V$. This way we can find the local electric potential for all pixels in the device.

The approach we presented here has enabled the quantitative local electric potential mapping directly from raw experimental data without requiring any prior calibration or numerical simulations, which represents significant improvements in the accessibility of in-Liquid SDM technique as now, at least for EGTs, quantitative information can be extracted directly. The local electric potential mapping using the conventional Kelvin Probe Force Microscopy (KPFM) technique is forbidden in aqueous electrolytes due to various fundamental and technical challenges owing to strong DC and low-frequency AC bias-induced charge screening dynamics prohibiting direct access to local electrical properties[10], which our approach successfully circumvented for the case of laterally biased semiconducting devices in electrolytes like EGTs. The KPFM implementation in the air environment has enabled several key studies on potential distribution and charge-trapping dynamics in OFET devices and has been an indispensable tool in advancing the fundamental understanding of organic materials and devices[11]. We hope our approach for electric potential mapping in the liquid environment proves to be beneficial for a wide range of applications.

In the next chapter on EGOFETs, we extensively use this new approach of electric potential mapping and extracted information about charge transport bottlenecks, like contact access resistances, inter- and intra-domain charge transport, microstructural inhomogeneities and conduction anisotropy, that were inaccessible earlier in these devices.

2.4. References

1. L. Kergoat, L. Herlogsson, B. Piro, et al., “Tuning the threshold voltage in electrolyte-gated organic field-effect transistors,” *Proceedings of the National Academy of Sciences*, vol. 109, pp. 8394–8399, 2012. doi: 10.1073/pnas.1120311109

2. L. Huetter, A. Kyndiah, and G. Gomila, “Analytical physical model for organic metal-electrolyte-semiconductor capacitors,” *Advanced Theory and Simulations*, vol. 6, p. 2200698, 2023. doi:10.1002/adts.202200698

3. L. Huetter, A. Kyndiah, and G. Gomila, “Analytical physical model for electrolyte gated organic field effect transistors in the helmholtz approximation,” *Advanced Theory and Simulations*, vol. n/a, p. 2200696, 2023. doi:10.1002/adts.202200696

4. “Why your function generator outputs twice the programmed voltage,” https://web.archive.org/web/20220127082701/https://edadocs.software.keysight.com/kkbopen/why-your-function-generator-outputs-twice-the-programmed-voltage-589745012.html, accessed: 2023-06-07.

5. “Resonance in short transmission line,” https://web.archive.org/web/20210614095411/http://www.sigcon.com/Pubs/news/6_06.htm, accessed: 2023-06-07.

6. R. Millan-Solsona, M. Checa, L. Fumagalli, and G. Gomila, “Mapping the capacitance of self-assembled monolayers at metal/electrolyte interfaces at the nanoscale by in-liquid scanning dielectric microscopy,” *Nanoscale*, vol. 12, pp. 20 658–20 668, 2020. doi:10.1039/D0NR05723A

7. J. Schäpe, S. Prauße, M. Radmacher, and R. Stick, “Influence of lamin a on the mechanical properties of amphibian oocyte nuclei measured by atomic force microscopy,” *Biophysical Journal*, vol. 96, pp. 4319–4325, 2009. doi:10.1016/j.bpj.2009.02.048

8. S. Chiodini, S. Ruiz-Rincón, P. D. Garcia, et al., “Bottom effect in atomic force microscopy nanomechanics,” *Small*, vol. 16, p. 2000269, 2020. doi: https://doi-org.sire.ub.edu/10.1002/smll.202000269

9. P. D. Garcia and R. Garcia, “Determination of the elastic moduli of a single cell cultured on a rigid support by force microscopy,” *Biophysical Journal*, vol. 114, pp. 2923–2932, 2018. doi:https://doi.org/10.1016/j.bpj.2018.05.012

10. L. Collins, S. Jesse, J. I. Kilpatrick, et al., “Probing charge screening dynamics and electrochemical processes at the solid–liquid interface with electrochemical force microscopy,” *Nature Communications*, vol. 5, p. 3871, 2014. doi:10.1038/ncomms4871

11. V. Palermo, M. Palma, and P. Samorì, “Electronic characterization of organic thin films by kelvin probe force microscopy,” *Advanced Materials*, vol. 18, pp. 145–164, 2006. doi:https://doi.org/10.1002/adma.200501394

PART III

RESULTS

Chapter 3

Operando Characterisation of EGOFETs

Abstract Comprehensive nanoscale operando characterization of Electrolyte-Gated Organic Field-Effect Transistors (EGOFETs) is crucial to pinpoint various charge transport bottlenecks for rational and targeted optimization of devices. Here, we leverage the implementation of in-Liquid Scanning Dielectric Microscopy with added automated functionality and technical improvements, as described in Chapter 2, to systematically probe the electrical properties of EGOFETs and provide the first direct comprehensive picture of their functional mechanism at the nanoscale across all operational regimes - from sub-threshold, linear to saturation - until the onset of pinch-off. Surprisingly, the apparent extension of pinch-off into the channel depends on the multiscale structural characteristics of the thin film semiconductor. We observed heterogeneous suppression of measured local electrostatic forces that are found to be correlated with the semiconductor microstructure and the properties of grain boundaries, implicating inferior charge transport overall during operation. We use the interpretation framework developed in Chapter 2 (section 2.3) that enables quantitative local electric potential mapping to perform a nanoscale assessment of various charge transport bottlenecks, like contact access resistances, inter- and intra-domain charge transport, microstructural inhomogeneities and conduction anisotropy, that were inaccessible earlier at the nanoscale. The results discussed in this chapter contribute to an improved fundamental understanding of charge transport in EGOFETs and promote the development of direct structure-property-function relationships to guide future design rules.

3.1. Introduction

As described in Chapter 1 (subsection 1.4.1), Electrolyte-Gated Organic Field-Effect Transistors (EGOFETs) are widely regarded as a basic building block for emerging bioelectronic technologies[1]. Despite being the foundational architecture, our fundamental understanding of the nanoscale charge carrier transport governing the device operation remains poor, which hinders further progress in the rational and target optimization of devices for various applications.

EGOFETs are generally fabricated using cost-effective and low-temperature solution-phase thin-film processing methods to enable the possibility of large-scale production. However, the resulting semiconducting thin film exhibit polycrystallinity depicting diverse arrangements of crystalline micrometric domains across the millimetre scale of the device. The polycrystallinity introduces complexities in the charge transport that give rise to non-idealities, thereby causing significant deviations in the device physics compared to single-crystal counterparts. In solid-state OFETs, many studies have focused on understanding the structure-property relationship in operating devices to pinpoint charge transport bottlenecks[2,3]. Kelvin Probe Force Microscopy (KPFM) is a widely used characterization method for measuring local electric potential distribution and charge trapping dynamics and has been an indispensable tool in advancing the fundamental understanding of organic materials and devices[4]. However, EGOFETs fundamentally involve different interfaces for charge transport than OFETs, making it challenging to reliably translate the findings from air to liquid environment. At the same time, KPFM cannot operate in aqueous electrolytes due to fundamental and technological challenges, as explained earlier in Chapter 2 (section 2.3).

Recently, in-liquid electrical scanning probe techniques, such as Scanning Electrochemical Microscopy (SECM)[5] and in-liquid Scanning Dielectric Microscopy (in-liquid SDM)[6], have been proposed as viable options where the probe is located above the semiconducting channel at the electrolyte/semiconductor interface and directly probes the local electrical properties, see Chapter 1 (subsection 1.6.3 and subsection 1.6.4) for discussion on these techniques and their reported implementations. As we have mentioned there, Mariani et al. used SECM to measure the electrochemical potential relative to the quasi-reference electrode in millimetre-sized operating Organic Electrochemical Transistors (OECTs), enabling microscopic determination of charge carrier density and mobility[5]. However, the size of the micrometric SECM probe limits the resolution and the device physics that can be explored. Also, the imaging capabilities are cumbersome as the SECM measurement reported required re-polishing the microelectrode before probing a different location of the polymer surface. On the other hand, Kyndiah et al. implemented in-Liquid SDM for nanoscale mapping of the electrical properties (conductivity and interfacial capacitance) via measurement of local electrostatic forces in operating EGOFETs[6]. The measured electrostatic forces are converted to maps of local conductivity and interfacial capacitances using finite element modelling (FEM) approaches. However, the potential of these techniques to gain a comprehensive understanding of charge carrier transport at the nanoscale under different operating conditions and microstructural thin film arrangements remains largely unknown, primarily mainly because of fundamental and technical challenges in accessing certain electrical properties like local electric potential and secondarily due to difficulty in gaining quantitative information quickly, until now. These objectives (mentioned earlier also in Chapter 1 section 1.7) are achieved in the context of the present thesis.

This chapter provides a comprehensive nanoscale understanding of structure-property-function relationships in operating EGOFETs through the developments described earlier in Chapter 2. We explored all operating regimes, namely sub-threshold, linear and saturation. We also explored different microstructural signatures of the semiconducting thin film and their impact on the multiscale evolution of electrical properties. Using the interpretation framework introduced in Chapter 2 (section 2.3), we created quantitative local electric potential maps that allowed nanoscale assessment of various charge transport bottlenecks, like contact access resistances, inter- and intra-domain charge transport, microstructural inhomogeneities and conduction anisotropy.

3.2. Results and Discussions

We performed comprehensive investigations of EGOFETs based on a blend of organic semiconducting material diF-TES-ADT* and the insulating polymer polystyrene (PS), which we used earlier as a test platform to demonstrate the capabilities of in-Liquid SDM[6]. The transistors were fabricated by Sara Ruiz-Molina in the group of Prof. Marta Mas-Torrent at ICMAB†. The structure-property rela-

---

*2,8-difluoro-5,11-bis(triethylsilylethynyl)anthradithiophene

†Lab website: https://molecularelectronics.icmab.es/

tionships in its solid-state OFETs are well-studied with many techniques[7,8], thus providing the foundation for corroborating our results discussed in this chapter.

3.2.1. Macroscale Characterization of EGOFETs

The schematic for post-operando and in-operando characterization of the EGOFETs is shown in Figure 3.1A and Figure 3.1B. The rationale behind incorporating two gate electrodes is to allow the flexibility of using the external gate electrode of any material to gate the transistor and not be limited by the availability of an appropriate AFM cantilever, as justified previously in Chapter 2 (section 2.1). The optical microscopy image of the device (in dry and unbiased conditions) with and without a polarizer is shown in Figures Figure 3.1C and Figure 3.1D, respectively. The device consists of interdigitated source-drain electrodes with a channel length of L=30μm, an effective channel width of W=19680μm (W/L=656) and the nominal thickness of h_{sem}=30nm of the semiconductor. The contrast in the polarised optical microscopy image resulting from the birefringence of the semiconducting material is clearly evident, depicting the heterogeneity due to different orientations of the crystalline domains that originate from the PFBT-coated electrode surface and interleave in the channel area, as reported earlier in such devices[8]. The contrast due to underlying source-drain electrodes is also visible. The presence of well-defined domain boundaries in the channel area implies that understanding their impact on the device's performance is necessary.

Figure 3.2 shows the transfer and output characteristics of the device measured in 1mM NaCl solution under in-operando and post-operando configuration shown in Figure 3.1 earlier. The transfer characteristics show the typical behaviour of an accumulation mode field-effect transistor. Whereas from the output characteristics different operating regimes, namely sub-threshold, linear and saturation, can be identified easily. Using a recently introduced theoretical Helmholtz model considering the series resistance effect by Huetter et al[9], the output I-V curves can be quantitatively analyzed. The model perfectly fits the output characteristics, as shown in Figure 3.2B with dot-dash black lines, with parameters: $V_{\text{TH}} = -0.51V$, mobility-capacitance product $\mu_p c_H = 1.9\mu S/V$ and series resistance $R_s = 5k\Omega$. The mobility-capacitance product agrees well with the values reported in the literature[10], indicating an acceptable level of intrinsic performance despite a relatively large threshold voltage. The large threshold could be the consequence of using two gate electrodes which shifts the threshold to a value that is determined

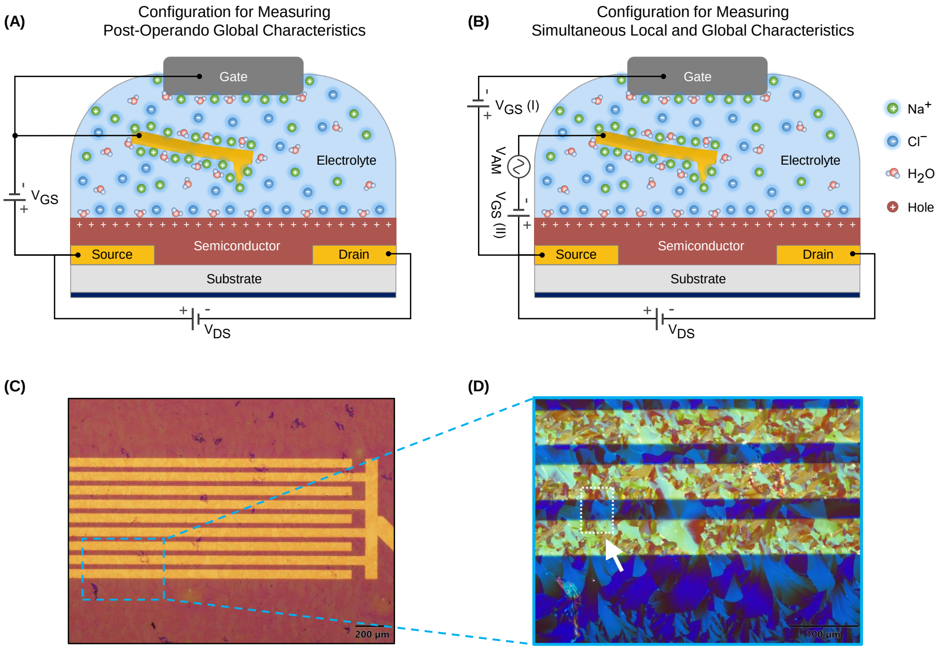

Figure 3.1: (A) Experimental configuration for post-operando device I-V characterization, only DC gate voltage (V_{GS}) is applied to the junction connecting both gold SDM probe and external platinum gate electrode from the same power source, and V_{DS} is applied between source and drain electrodes. (B) In-operando experimental configuration for simultaneous local and global characterization where the gold SDM probe is biased with the DC gate voltage (V_{GS}) offset to amplitude-modulated (V_{AM}) waveform, and the external platinum gate electrode is biased with just DC gate voltage (V_{GS}). (C) Optical microscopy image of the interdigitated device with nominal channel length L=30μm, width W=19680μm (W/L=656), and thickness h_{sem}=30nm. (D) Polarized light microscopy image of the region marked with a blue rectangle in (B). The region marked with a white rectangle and white arrow indicates the location where in-Liquid SDM local measurements are done.

by the work function of the electrodes and respective interfacial capacitances as discussed in Chapter 2 (section 2.1). The series resistance probably stems from the staggered configuration of the device[9], the polycrystalline thin film nature of the semiconducting material and the low transversal conductivity of this material owing to inferior out-of-plane π-orbital overlap[7] leading to high access resistance.

The effective device conductivity is also calculated from the output characteristics at $V_{\text{DS}} = 0V$ using:

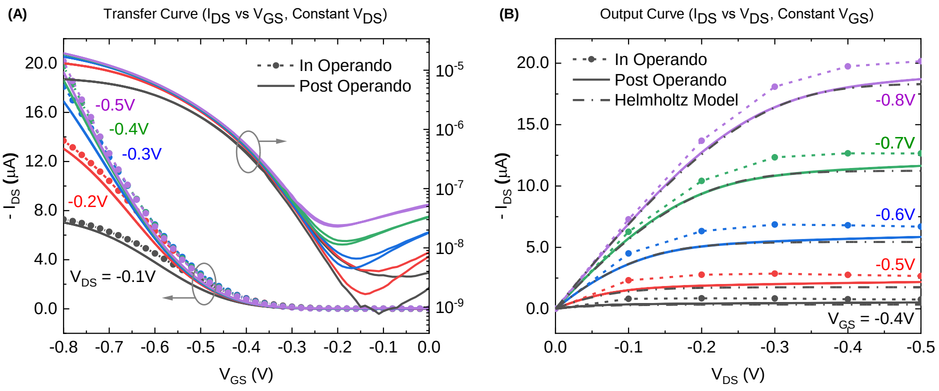

Figure 3.2: (A) Transfer and (B) Output I-V characteristics of one of the EGOFET analyzed. The symbols with dotted lines correspond to the average drain current measured during in-liquid SDM while the continuous lines refer to post-operando I-V measurements performed after the full set of in-liquid SDM measurements. The dot-dash line in output curves shows fitting with the Helmholtz model considering series resistance effects.

$$\sigma_0(V_{\mathrm{GS}}) = \left(\frac{L}{Wh_{sem}}\right)\cdot\frac{\partial I_{\mathrm{DS}}}{\partial V_{\mathrm{DS}}}\bigg|_{V_{\mathrm{DS}}=0V} \tag{3.1}$$

which is shown in Figure 3.3 by the black dots. The continuous red line represents the prediction of the Helmholtz model considering the series resistance effect in excellent agreement, while the dashed red line indicates the overall semiconductor conductivity after removing the series resistance contribution reaching >10S/m. The analysis illustrates that series resistance effects severely limit the device's performance; however, notably, these EGOFETs have shown remarkably robust performance despite this limitation[11,12].

3.2.2. Probing Operating Regimes of EGOFETs at Nanoscale

In-liquid SDM measurements following the approach described in Chapter 2 were performed on a region marked with a white colour dashed-rectangle in Figure 3.1D. The topography and polarised light micrograph of this region ($64 \times 45 \mu m^2$) spanning source-channel-drain area are shown in Figure 3.4(A-B) respectively, where different crystalline domains of the semiconductor thin film are distinctly visible in the polarised light micrograph although not so much in the topography. The relative electrostatic force images with $Z_{lift} = 100nm$ and $Z_{ref} = 2000nm$ of this

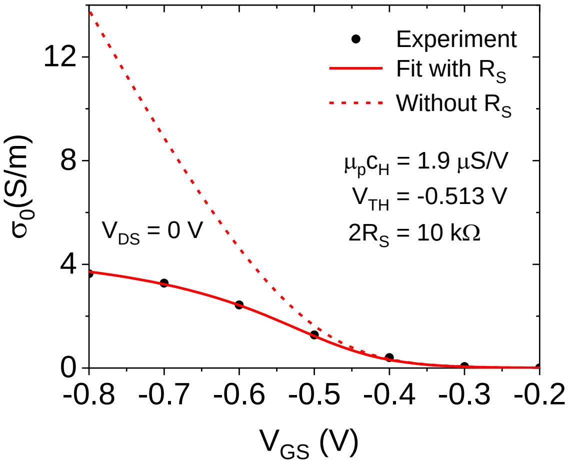

Figure 3.3: (symbols) Device conductivity at $V_{\mathrm{DS}} = 0V$ obtained from the I-V output curves as a function of V_{GS}. (continuous line) Prediction of the Helmholtz model including series resistance with the parameters: $V_{\mathrm{TH}} = -0.51V$, mobility-capacitance product $\mu_p c_H = 1.9\mu S/V$ and series resistance $R_s = 5k\Omega$. (dashed line) Overall semiconductor conductivity at $V_{\mathrm{DS}} = 0V$ after subtracting the effect of series resistance.

region in the off-state ($|V_{\mathrm{GS}}| < |V_{\mathrm{TH}}|$) and on-state ($|V_{\mathrm{GS}}| > |V_{\mathrm{TH}}|$) are shown in Figure 3.4(C-D), respectively. As mentioned in Chapter 2, the changes in electrostatic force at a specific pixel are directly linked to the local conductivity changes at that point, assuming conductivity is the sole electrical property affected by bias voltages. In high-frequency measurements, the variation in diffuse double-layer capacitance has no role, with Stern interfacial capacitance generally remaining constant as a function of bias voltages. Figure 3.4C shows a noticeable contrast between the source/drain and channel regions, attributed to a metal electrode versus an insulating substrate beneath the semiconducting film, as described in Chapter 1 (subsection 1.6.4). In the off-state (Figure 3.4C), the electrostatic forces are low whereas in the on-state (Figure 3.4D), they increase everywhere. There are slight correlations with the polarised optical micrograph as marked with a black arrow and red circle. Also, very subtle variations in the force exist in the channel region that could be traced to the corresponding broad features in the polarised image.

We explore further a small region marked with a white rectangle in the topographic image shown in Figure 3.4A at different drain voltages in the on-state to see if the microstructure has any impact in operating conditions when drain current is

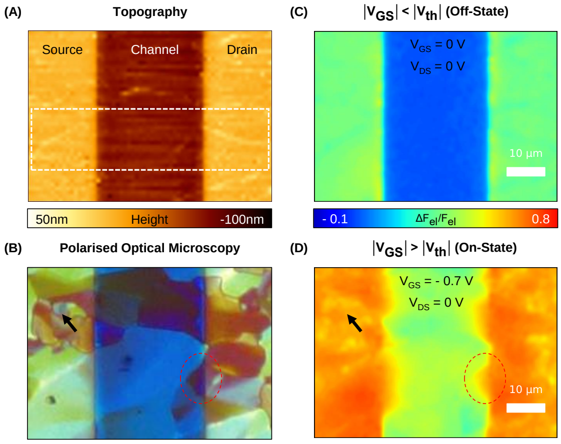

Figure 3.4: (A) Topographic image of a $64 \times 45\mu m^2$ region of the EGOFET transistor (dashed white rectangle region in Figure 3.1D), including parts of source, channel, and drain. (B) Polarization light micrograph of the same region in (A). (C-D) Relative electrostatic force lift-mode images ($Z_{lift} = 100nm$ and $Z_{ref} = 2000nm$) for $V_{\mathrm{DS}} = 0V$ and $V_{\mathrm{GS}} = 0$ and $-0.7V$ corresponding to off-state and on-state respectively. The scale bar is $10\mu m$. Experimental parameters for in-liquid SDM measurements: Electrolyte: 1mM NaCl, Gate: Au SDM probe (HQ:NSC19/Cr-Au) + Pt external electrode, $f_{el} = 25MHz$, $f_{mod} = 10kHz$, $V_{ac} = 2VPP$, pixels 64×45, $k = 1.097N/m$, $f_{res} = 34.90kHz$ (cantilever).

flowing in the channel. The choice of this specific region for further measurements is based on its composition, which includes a homogeneous section comprising a single crystalline domain linking the source and drain electrode (upper segment of the image) and a region where multiple domains intersect (lower segment of the image). Although the homogeneous region sparingly occurs, as apparent in Figure 3.1D, it provides an opportunity to probe such an arrangement later at different drain and gate voltages to see if it leads to any difference in nanoscale electrical properties (which we later found is indeed the case).

This region ($64 \times 16\mu m^2$) spanning source-channel-drain area is shown in Figure 3.5(A-B) with polarised optical micrograph and topographic image respectively. The topography shows relatively uniform thin-film morphology with few matching structural features highlighted by black, red and white arrows; notably, not all features match since not all of them will give rise to topographic variations. The height difference between the channel and electrodes is $\sim 55 \pm 10nm$, as depicted by the superimposed cross-section profile, and is in reasonably good agreement with the nominal thickness of the electrodes ($\sim 45nm$). Figures Fig-

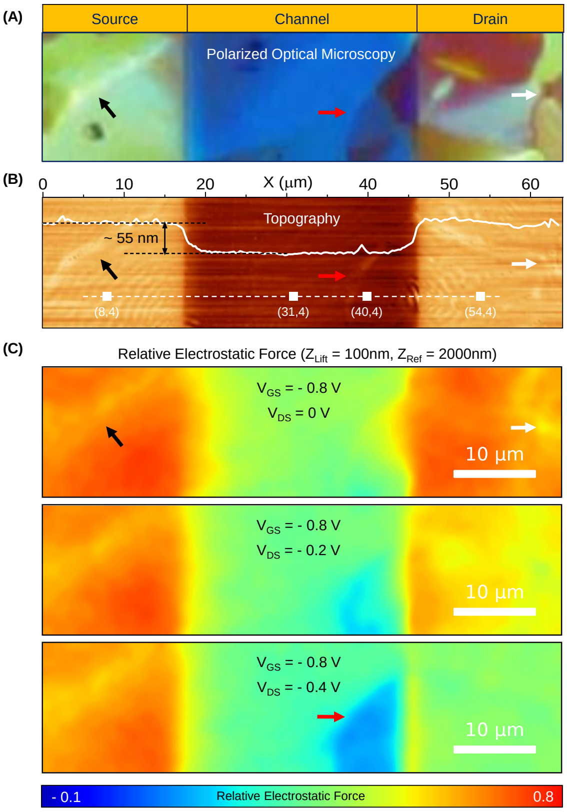

Figure 3.5: Correlating Microstructure with Local Electrostatic Force (A) Polarization light micrograph of a $64 \times 16 \mu m^2$ region of the EGOFET transistor (dashed white rectangle region in Figure 3.1D), including parts of source, channel, and drain. (B) AFM topography of the same region in (A) with the superimposed topographic profile. (c) Relative electrostatic force lift-mode images ($Z_{lift} = 100nm$ and $Z_{ref} = 2000nm$) for $V_{\text{GS}} = -0.8V$ and $V_{\text{DS}} = 0$, $-0.2V$ and $-0.4V$. The scale bar is $10\mu m$. Experimental parameters for in-liquid SDM measurements: Electrolyte: 1mM NaCl, Gate: Au SDM probe (HQ:NSC19/Cr-Au) + Pt external electrode, $f_{el} = 25MHz$, $f_{mod} = 10kHz$, $V_{ac} = 2VPP$, pixels 64×16, $k = 1.097N/m$, $f_{res} = 34.90kHz$ (cantilever).

ure 3.5C show the lift-mode relative electrostatic force images with $Z_{lift} = 100nm$ and $Z_{ref} = 2000nm$, for $V_{\text{GS}} = -0.8V$ and $V_{\text{DS}} = 0$, $-0.2V$ and $-0.4V$. When the drain voltage is zero, the electrostatic force appears symmetrical, as both the source and the drain display similar colours. Contrarily, increasing the drain voltage introduces asymmetry, resulting in lower values at the drain representing low local conductivity. Additionally, there is some correlation between the electrical image and the features highlighted in Figure 3.5A, particularly in the channel region where specific features only manifest at high drain voltages and are associated with the grain boundary. This represents that under applied drain voltages, the microstructure of the underlying thin film starts playing an important role.

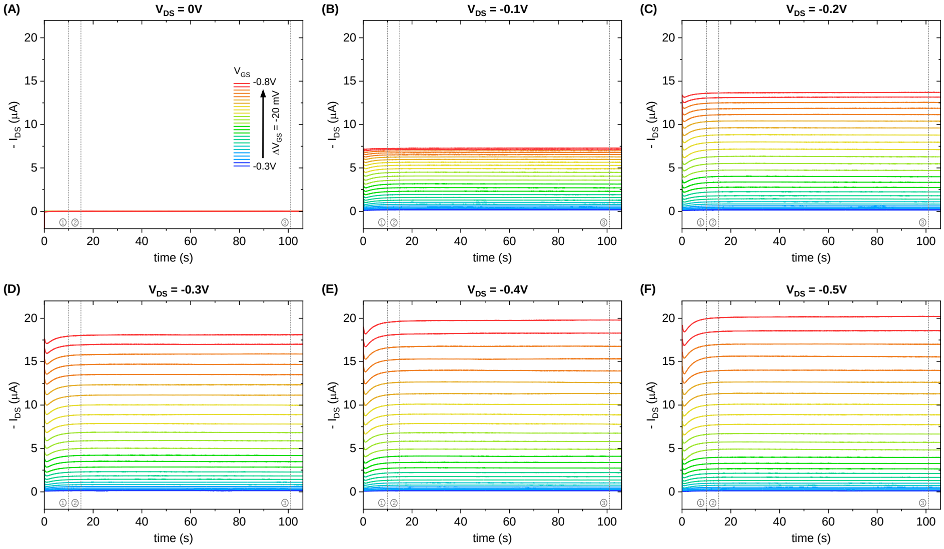

Figure 3.6: I_{DS} vs time evolution during operando in-Liquid SDM measurements (A) I_{DS} vs time traces for V_{GS} from $-0.3V$ to $-0.8V$ and V_{DS} (A) $0V$, (B) $-0.1V$, (C) $-0.2V$, (D) $-0.3V$, (E) $-0.4V$, and (F) $-0.5V$. Originally the measurements are done starting from $V_{GS} = 0.2V$, however, since the transistor is in the off-state in the range $V_{GS} = 0.2V$ to $V_{GS} = -0.3V$, the curves are displayed starting from $V_{GS} = -0.3V$ onwards. The legends are the same for all graphs, so they are displayed only for the case of $V_{DS} = 0V$. For each measurement, at $time = 0s$, the bias voltages (V_{GS} and V_{DS}) are applied, and after a wait of $10s$ (denoted by the dotted line ① in the graph) the SDM probe is approached to the surface, thereafter it waits for $5s$ more (denoted by the dotted line ② in the graph) before starting the imaging. The single image takes $86s$, and then the tip is retracted (denoted by the dotted line ③ in the graph), and then the bias voltages are kept for $5s$ more before turning them off.

To investigate it further, similar measurements are performed for many (*thanks to Automation*) drain and gate voltages. The stable gate voltage window is from $+0.2V$ to $-0.8V$ (step size = $0.02V$, $\# = 51$) and drain voltage from $0V$ to $-0.5V$ (step size = $0.1V$, $\# = 6$) covering all transport regimes, giving rise to 306 different operating points and electrical images. We observed that voltages outside the above stability window lead to irreversible topographic changes in the transistor, especially near the source edge. These changes coincided with a decrease in the AFM photodiode sum signal, which might be attributed to simultaneous irreversible electrochemical reactions occurring on the SDM probe; see **Appendix C** for gate voltage stability measurements. The simultaneously recorded drain current versus time traces during operando in-Liquid SDM for all the measured operating points are shown in Figure 3.6, along with the time window where imaging is done. These traces are used to reconstruct the in-operando transfer and output curves shown earlier in Figure 3.2 with dotted lines and symbols. Remarkably, these reconstructed curves are consistent with post-operando device characterization performed after operating the transistor for more than nine hours for 306 in-Liquid SDM measurements (1min 46sec each), demonstrating the high stability of the device.

Figure 3.7 shows the nanoscale evolution of electrostatic force as a function of drain and gate voltages, encompassing sub-threshold, linear, and saturation regimes. As mentioned earlier, the measurements are done starting from $V_{\mathrm{GS}} = 0.2V$. However, since the transistor is in the off-state in the range $V_{\mathrm{GS}} = 0.2V$ to $V_{\mathrm{GS}} = -0.3V$, the images are displayed starting from $V_{\mathrm{GS}} = -0.3V$ onwards only. Different transport regimes are denoted with thick dashed lines overlaying the images according to the output I-V characteristics shown in Figure 3.2B.

Figure 3.8 shows relative electrostatic force profiles along scan line 4 in (A)-(F) and scan line 15 in (G)-(L), for images shown in Figure 3.7 to comprehend the trends easily as a function of drain and gate voltages. The location of these scan lines is shown in Figure 3.7 for the case of $V_{\mathrm{DS}} = -0.1V$ and $V_{\mathrm{GS}} = -0.6V$. Scan line 4 traverses an area containing intersecting crystalline domains, while scan line 15 traverses the region where a single crystalline domain bridges the source and drain.

In the sub-threshold regime, the conductivity is too low to be detected; therefore, the measured electrostatic force reflects the interaction of the conductive tip with an insulating material and thus stays low. As the gate voltage surpasses the threshold voltage, the conductivity is high enough to be detected by the SDM probe (refer Chapter 1 subsection 1.6.4 for the discussion on the sensitivity of in-Liquid SDM). For $V_{\mathrm{DS}} = 0V$, the force starts increasing uniformly across the device with increasing gate voltage, as shown by the images in the first column

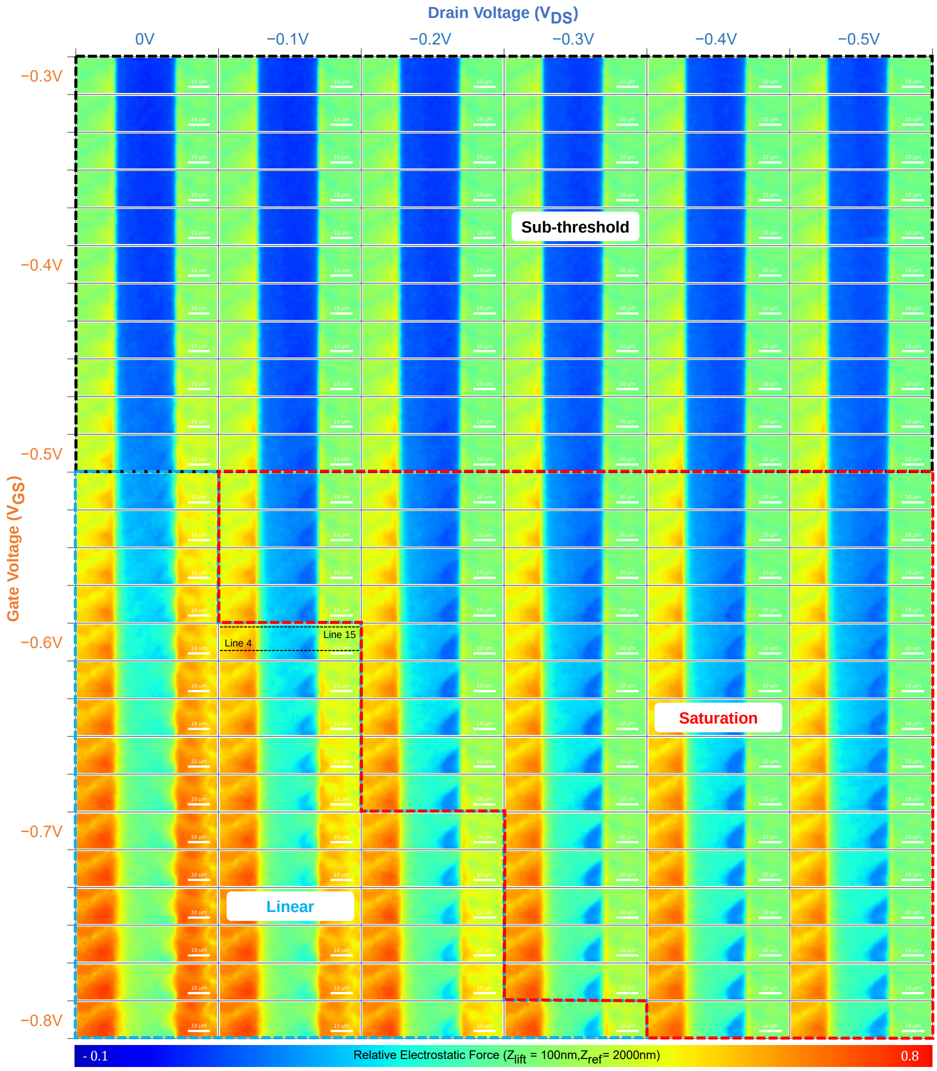

Figure 3.7: Nanoscale Probing of Different Operating Regimes of EGOFET. Lift-mode relative electrostatic force images ($Z_{lift} = 100nm$ and $Z_{ref} = 2000nm$) for V_{GS} ($\Delta V_{\text{GS}} = 20mV$) and V_{DS} ($\Delta V_{\text{GS}} = 100mV$) voltages covering all operating regimes, which are highlighted by the thick dashed lines (black for subthreshold, blue for linear, and red for saturation regime). The scale bar is $10\mu m$. Experimental parameters same as in Figure 3.5.

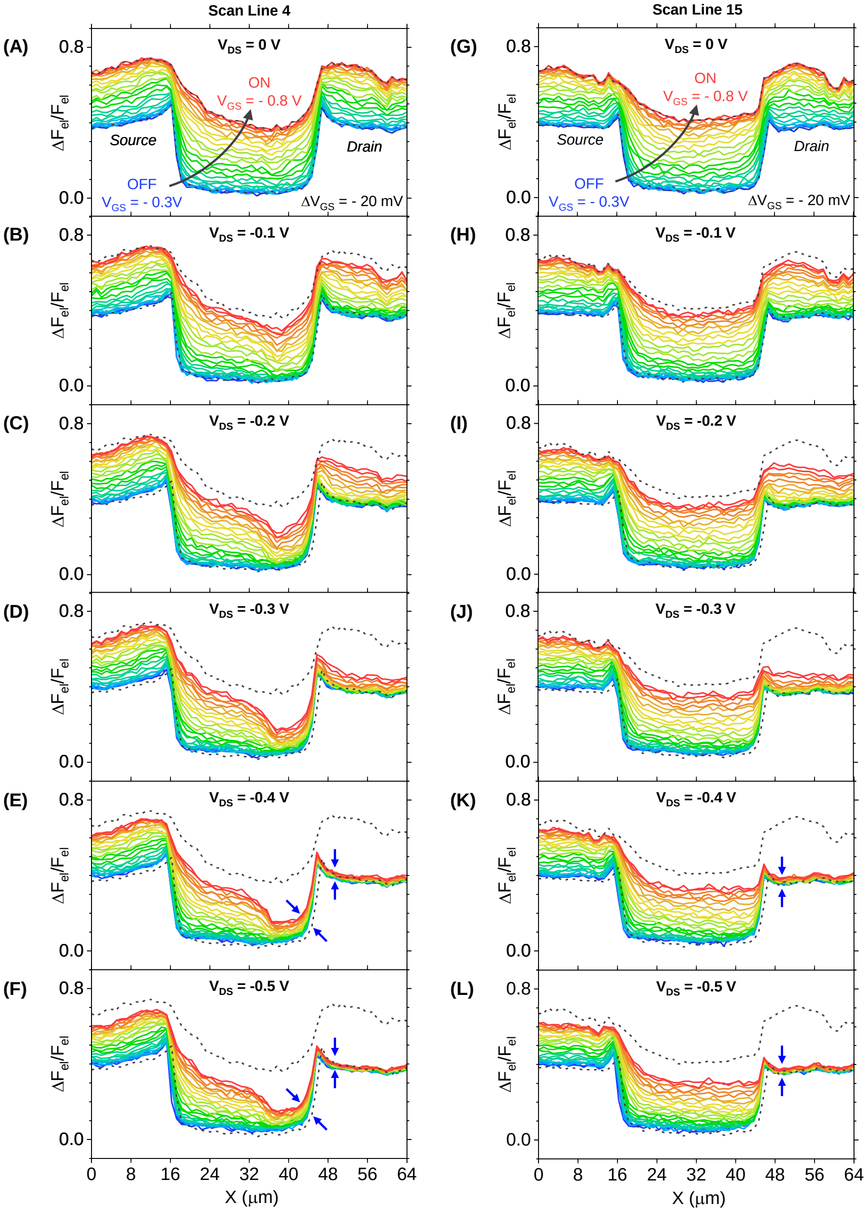

Figure 3.8: Nanoscale Probing of Different Operating Regimes of EGOFET. Relative electrostatic force profiles along (A)-(F) scan line 4 and (G)-(L) scan line 15 for images shown in Figure 3.7. The location of the scan lines 4 and 15 is shown in Figure 3.7 for the case of $V_{DS} = -0.1V$ and $V_{GS} = -0.6V$. The grey dashed profile represents the sensitivity limits of the electrostatic force on the local conductivity.

in Figure 3.7 and by profiles in Figure 3.8A and 3.8G. The grey dashed lines in Figure 3.8 correspond to the condition where electric force becomes insensitive to local conductivity, either because it is too high (top dashed line) or too low (bottom dashed line). In the linear regime, the application of drain voltage leads to asymmetry in the spatial distribution with force decreasing over the drain electrode, see Figure 3.8(B-D) and 3.8(H-J). For high enough drain voltages, the force over the drain is not modulated by the gate voltage any further, indicating locally off-state and denoting the occurrence of Pinch-off in the saturation regime, as shown in Figure 3.8(E-F) and 3.8(K-L).

An important observation easily evident from the images in Figure 3.7 is that features correlating with the polycrystalline microstructure (shown in Figure 3.5A) start appearing in the channel with increasing drain voltages and are especially pronounced in the saturation regime. Regarding pinch-off, we also observe a surprising difference between profiles for scan lines 4 and 15. Scan line 4 passes through the region where different crystalline domains intersect, and this microstructure seems to promote the apparent extension of the pinch-off in the channel, as indicated by blue arrows in Figure 3.8(E-F). In contrast, for scan line 15 in Figure 3.8(K-L), the pinch-off is restricted only over the drain electrode.

To comprehensively assess the diversity of influence these microstructures could have on the evolution of local electrical properties, measurements were performed on various devices and regions exhibiting unique multiscale structural features.

Figure 3.9 represents a case where the AFM topography of the grain boundary consists of a pattern of open gaps and closed smooth boundaries between adjacent grains, topographically similar to the one reported for diF-TES-ADT:PTAA blend thin-film[13]. In this case, the microstructure is clearly visible at high drain voltage, although subtle compared to the one in Figure 3.7, representing a moderately restricting grain boundary. The pinch-off does extend into the channel due to this microstructure.

Figure 3.10 shows a subtle grain boundary effect at intermediate gate voltages; however, a pronounced impact is observed at high gate voltages with a sudden massive drop at the grain boundary, even for $V_{\mathrm{DS}} = 0V$. Such a behaviour if present dominantly in the device could impact its global performance at high charge carriers or current densities.

Finally, Figure 3.11 illustrates a case where part of the channel is decorated with 3D textured crystallites, suspected in the literature to be detrimental to charge

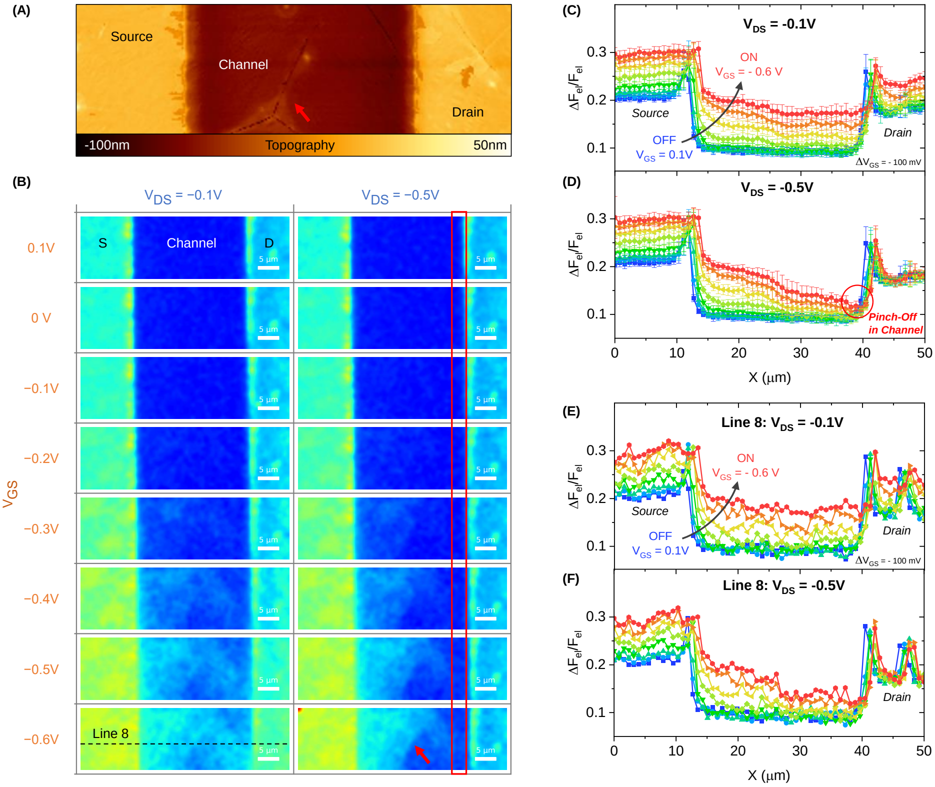

Figure 3.9: (A) AFM topography of the EGOFET region analyzed showing a grain boundary consisting of a pattern of open gaps and closed smooth boundaries between adjacent grains. (B) Lift-mode relative electrostatic force images ($Z_{lift} = 100nm$ and $Z_{ref} = 1500nm$) for different V_{GS} ($\Delta V_{\text{GS}} = 100mV$) and $V_{\text{DS}} = -0.1V$ (linear regime), $-0.5V$ saturation regime. (C) and (D) Averaged profile of all scan lines in an electrical image as a function of the gate voltages and for $V_{\text{DS}} = -0.1V$ and $-0.5V$, respectively. (E) and (F) Line profile of electrical images along scan line 8 as a function of the gate voltage and for $V_{\text{DS}} = -0.1V$ and $-0.5V$, respectively. The scale bar is $5\mu m$. Experimental parameters for in-liquid SDM measurements: Electrolyte: milli-Q, Gate: Only Platinum SDM probe (PPP-CONTSCPt), $f_{el} = 10MHz$, $f_{mod} = 2kHz$, $V_{ac} = 2.2VPP$, pixels 64×19, $k = 0.603N/m$, $f_{res} = 9.547kHz$ (cantilever).

transport[8]; indeed, we observed that the electrostatic force evolution in this region is limited as a function of gate voltage compared to the homogenous region. The slope of the relative electrostatic force versus V_{GS} in Figure 3.11D clearly illustrates that the region decorated with 3D textured crystallites (red) has the lower mobility-capacitance product than the homogenous region (green) correspondingly.

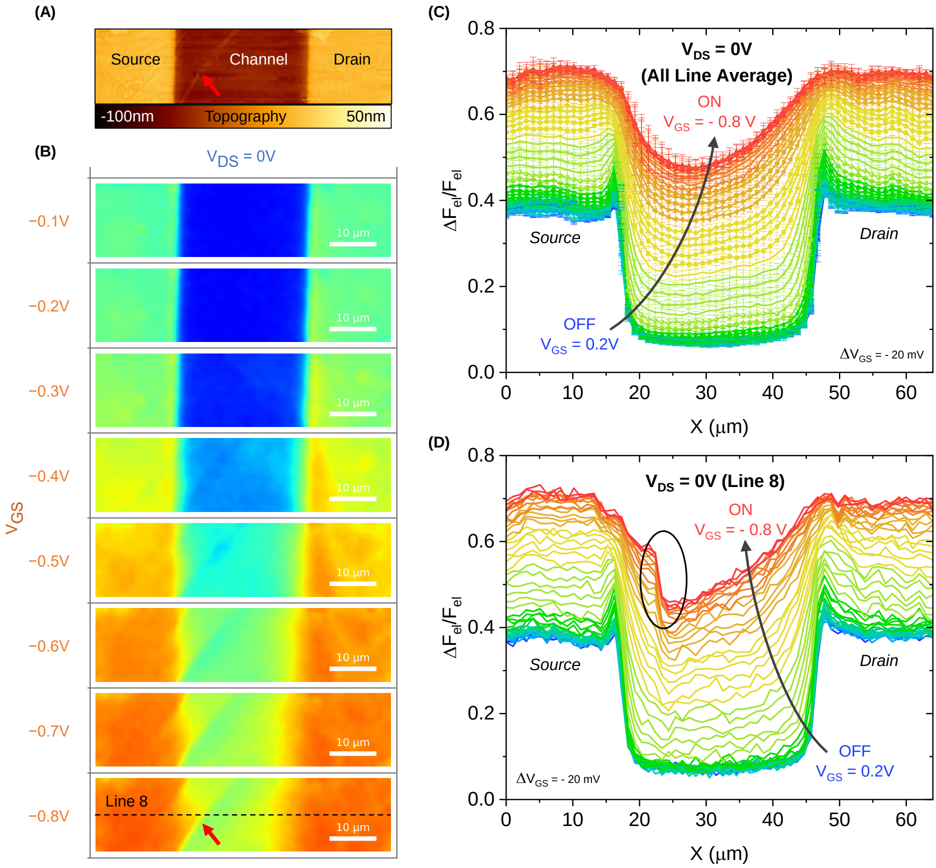

Figure 3.10: (A) AFM topography of the EGOFET region analyzed with (B) Lift-mode relative electrostatic force images ($Z_{lift} = 100nm$ and $Z_{ref} = 2000nm$) exhibiting a subtle grain boundary effect at intermediate gate voltages; however, a pronounced impact at high gate voltages with a sudden massive drop at the grain boundary. (C) Averaged profiles of the electrical images as a function of gate voltages. (D) Line profile of electrical images along scan line 8 as a function of the gate voltage. The scale bar is $10\mu m$. All the measurements shown are for $V_{DS} = 0V$. Experimental parameters for in-liquid SDM measurements: Electrolyte: 1mM NaCl, Gate: Au SDM probe (HQ:NSC19/Cr-Au) + Pt external electrode, $f_{el} = 25MHz$, $f_{mod} = 10kHz$, $V_{ac} = 2VPP$, pixels 64×16, $k = 1.11N/m$, $f_{res} = 34.94kHz$ (cantilever).

Also, the slope of the curve corresponding to the source (black) matches the one in 3D textured crystallites (red) indicating that the region over the source is also electrically inferior in performance. Similarly, the slope of the curve for the drain (blue) matches the one in the homogeneous region (green). This similarity is

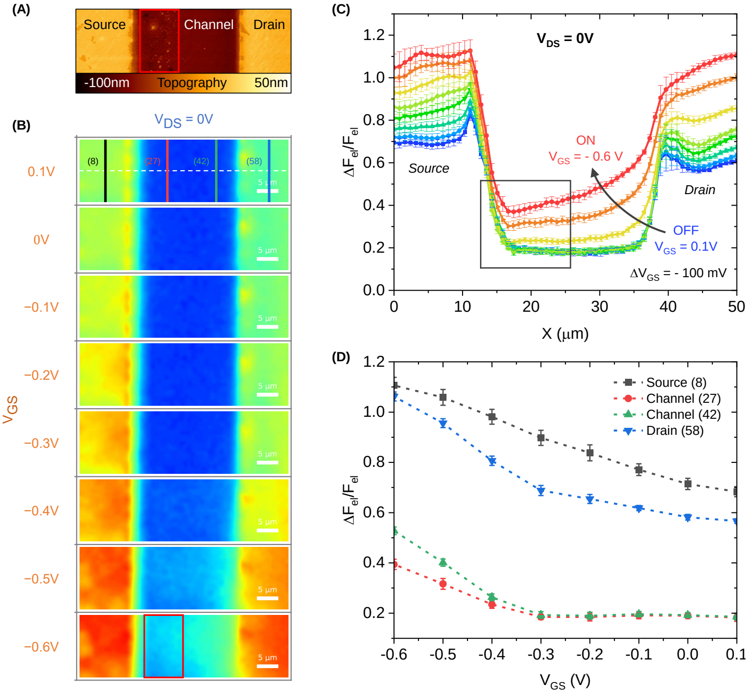

Figure 3.11: (A) AFM topography of the EGOFET region where part of the channel is decorated with 3D textured crystallites (red rectangle). (B) Lift-mode relative electrostatic force images ($Z_{lift} = 100nm$ and $Z_{ref} = 1300nm$) as a function of gate voltage. (C) Averaged profiles of the electrical images as a function of gate voltages. (D) The evolution of relative electrostatic force as a function of gate voltage at the locations marked in the image shown in (B) for the case of $V_{\text{GS}} = 0.1V$ with the matching colours. The trends are taken from the averaged profiles with error bars so they are averaged in the vertical direction in the image. All the measurements shown are for $V_{\text{DS}} = 0V$. The scale bar is $5\mu m$. Experimental parameters for in-liquid SDM measurements: Electrolyte: milli-Q, Gate: Only Platinum SDM probe (PPP-CONTSCPt), $f_{el} = 10MHz$, $f_{mod} = 2kHz$, $V_{ac} = 1.5VPP$, pixels 64×19, $k = 0.537N/m$, $f_{res} = 9.566kHz$ (cantilever).

expected since the crystallites during the thin film formation start growing from the respective electrodes and interleave in the channel region.

In a nutshell, the diverse structural signatures that are studied impact differently the evolution of local electrical properties. As we have seen, the thin film's structure also influences at a multiscale the extension of the pinch-off into the channel. If a single domain exists between the source-drain electrode, the pinch-off is limited to the drain electrode. However, if there are multiple domains, the pinch-off extends to the channel, with the extension depending on the distribution of grains. In order to quantify the influence of microstructure and device imperfections, it would be desirable to map the electric potential distribution within the source-channel-drain region, as it will give access to crucial charge transport parameters such as contact access resistances, inter-and intra-domain charge transport and anisotropy.

3.2.3. Local Potential Mapping of Operating EGOFETs

We use the method developed in Chapter 2 (section 2.3) for the quantitative electric potential mapping directly from the raw experimental data (relative electrostatic force dataset) shown in Figure 3.7 and Figure 3.8. The working demonstration of the algorithm for this dataset is shown in Figure 3.12.

Figure 3.12(A-D) show the relative electrostatic force approach curves for $V_{\mathrm{DS}} = 0V$ and different V_{GS} from $-0.3V$ to $-0.8V$ (in steps of $20mV$) at four different locations on scan line 4 as highlighted in Figure 3.5B, namely source (8,4), channel (31,4), channel-grain (40,4) and drain (54,4). Figure 3.12(E-H) shows the same but for $V_{\mathrm{DS}} = -0.5V$. Evidently, the electrostatic forces have reduced owing to the local electric potential setup by the drain voltage, thereby decreasing the effective gate potential, and so does the conductivity and, therefore, the electrostatic force. For every curve in Figure 3.12(E-H), we can find the matching curve from Figure 3.12(A-D), respectively. For instance, consider the $V_{\mathrm{DS}} = -0.5V$ and $V_{\mathrm{GS}} = -0.8V$ curves highlighted by the black line with black symbols in Figure 3.12(A-D) for the respective locations; the corresponding local effective gate potentials are $V_{\mathrm{GS}} = -0.63V$ (8,4), $-0.65V$ (31,4), $-0.53V$ (40,4), and $-0.37V$ (54,4). Therefore, the local potential at these pixels for $V_{\mathrm{DS}} = -0.5V$ and $V_{\mathrm{GS}} = -0.8V$ is $V(x,y) = V_{\mathrm{GS}} - V_{\mathrm{GS}} = -0.17V$ (8,4), $-0.15V$ (31,4), $-0.27V$ (40,4), and $-0.43V$ (54,4). A Python algorithm as described in Chapter 2 (section 2.3) is used to find the potential distribution similarly for all pixels in the device.

First, we look at the influence of the drain voltage on the local electric potential to understand how the microstructure impacts the pinch-off extension into the channel.

Figure 3.13A shows the local electric potential maps for constant $V_{\mathrm{GS}} = -0.8V$ and varying V_{DS} from $-0.1V$ to $-0.5V$, spanning linear to saturation regime as defined in the associated output I-V curve. Interestingly, most of the potential

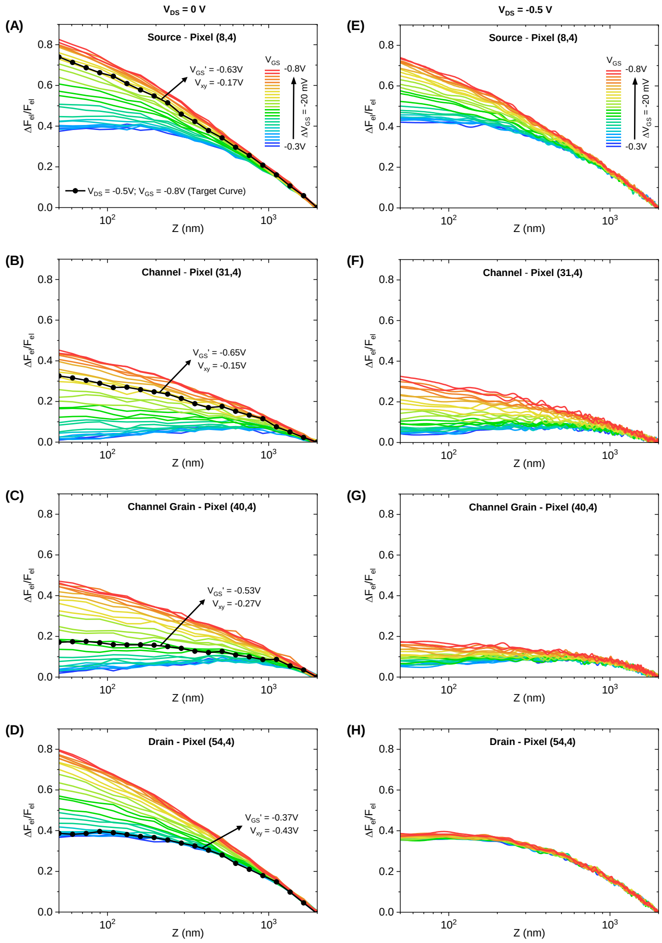

Figure 3.12: (A)-(D) Relative Electrostatic force ($Z_{ref} = 1300nm$) versus tip-sample distance approach curves at $V_{\mathrm{DS}} = 0V$ for different source-gate voltage at four different pixels along scan line 4 (highlighted in Figure 3.5B). The black line corresponds to the electric force for $V_{\mathrm{GS}} = -0.8V$ and $V_{\mathrm{DS}} = -0.5V$. By comparing with the $V_{\mathrm{DS}} = 0V$ curves one can obtain the local effective gate potential and then from it the local electric potential drop. (E)-(H) Represents approach curves for $V_{\mathrm{DS}} = -0.5V$ at the same corresponding locations. These approach curves corresponds to data shown in Figure 3.7 and Figure 3.8

drops at the contact or grain boundary as depicted by the sudden change of colour at their interfaces, whereas the crystalline domain shows minimal drop within them, indicating superior intra-domain charge transport with inferior inter-domain electrical connectivity. The potential on the source almost equals the adjacent channel area, and its absolute value increases with the drain voltage. On the other

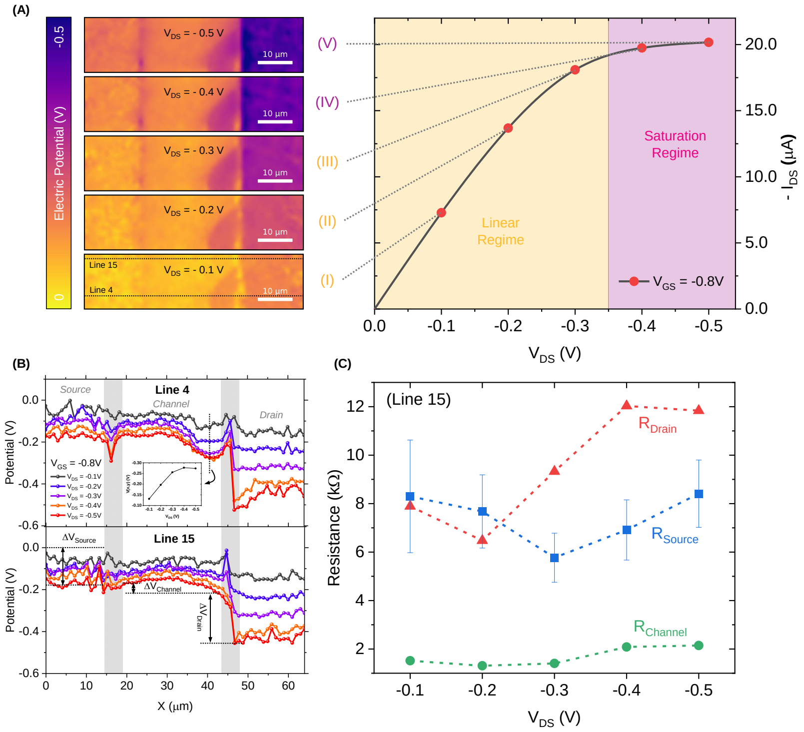

Figure 3.13: Local Potential Mapping of Operating EGOFET (A) Electric potential maps $V(x,y)$ corresponding to $VGS = -0.8V$ and VDS varying from $-0.1V$ to $-0.5V$ with $\Delta V_{DS} = 100mV$. Each map is linked to the corresponding point in the associated output I-V curve for $VGS = -0.8V$ (taken from Figure 3.2B). (B) Potential profiles along the scan lines 4 and 15, highlighted by dashed lines in (A). Inset in scan line 4 graph shows the local potential evolution in the crystalline domain attached to the drain electrode at the location highlighted by the dotted black line. The stripped grey region in the background represents the source/channel and channel/drain interface. (C) Resistances associated with source, channel and drain are calculated ($R = \Delta V / I_{DS}$) as a function of drain voltage from the potential profiles for the scan line 15 in (B) with ΔV highlighted for source, channel, and drain. The error bars for the source curve are derived from the standard deviation of potential over the source region for scan line 15. In the channel and drain case, the calculation is done using only two data points across their respective lengths/interfaces, so error bars are not plotted.

hand, the potential on the drain nearly follows that of the applied drain voltage, and the channel-drain interface absorbs a significant potential drop with increasing drain voltage.

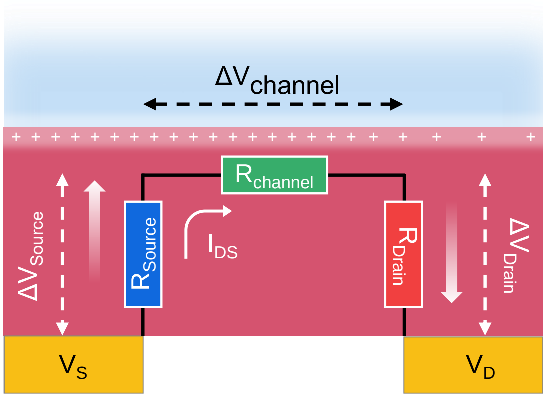

Figure 3.14: Schematic of the charge carrier transport path from source to drain with different resistances and voltage drops broadly identified.

These observations can be broadly explained through the schematic shown in Figure 3.14. For zero drain and increasing gate voltages, the channel is formed at the electrolyte/semiconductor interface that also occupies the area above the electrodes. As the drain voltage increases, the area above the drain starts depleting. To reach the same charge carrier concentration level prior to the application of a non-zero drain voltage, the gate voltage has to compensate for the local potential, which in this case will be the applied drain voltage, and thus V_{DS} defines the local potential over the drain electrode. As shown in the schematic, the charge carriers travel from the source to the conduction channel and face the source resistance (R_{source}) that includes source/semiconductor interface charge injection resistance and the semiconductor bulk access resistance; then it traverses the channel ($R_{channel}$) and reaches the drain electrode edge following the least resistance path (R_{drain}). The voltage drop at the source depends on the source resistance value relative to other resistances. In contrast, at the drain, the local potential follows that of the applied drain voltage as it directly depletes the charge carrier in the semiconducting thin film over the drain surface, as mentioned earlier. Another observation is that the potential at the source surface matches almost the one at the adjacent channel surface whose value increase with drain voltage. This can be explained based on how the voltage is distributed laterally. There is a very low potential drop in the crystalline domain in the channel as indicated by the same colour in the map across the domain. This suggests that the longitudinal conductivity is very high. But since the source potential changes substantially with the drain voltage, it indicates that the transversal conductivity over the source is very low compared to the longitudinal one and thus defines the potential over the source surface. This points towards the conduction anisotropy.

In these particular transistors that we studied, the source-drain electrodes treated with pentafluorobenzene thiol (PFBT) and are known to enforce $< 001 >$ crystallites of the diF-TES-ADT, where molecules pack co-facially with their aliphatic sidechains oriented perpendicular to the substrate[7,13]. The $< 001 >$-textured film exhibit optimal in-plane π-stacking, benefiting longitudinal charge carrier transport in the transistor channel. However, this arrangement reduces out-of-plane π-orbital overlap and thus suppresses transversal charge carrier transport over the electrodes. This could explain the conduction anisotropy we pointed out earlier. The presence of conduction anisotropy is further confirmed through finite element simulations of the interaction of the SDM probe with the sample. These simulations are out of the scope of this thesis, so they are not discussed here, for more information refer to [6].

Figure 3.13B shows the potential profiles along the scan lines 4 and 15 and can quantitatively describe the behaviour we observed regarding pinch-off in Figure 3.8. As shown in the inset of Figure 3.13B (line 4), the voltage drop in the channel grain connected to the drain electrode increases and then saturates with increasing drain voltage, thus leading to the extension of pinch-off into the channel region. In contrast, for scan line 15, the voltage at an equidistant location from the drain does not saturate with increasing drain voltage. Also, its value is less negative than the one in grain indicating that the effective gate potential is higher thus the upper homogenous region is more conductive and doesn't exhibit pinch-off in the channel region. Notably, a non-linearity in the channel potential for scan line 15 emerges at high drain voltages, which is consistent with the development of space charge transport in the semiconductor.

We can derive different resistances indicated schematically in Figure 3.14 as a function of bias voltages based on the voltage drop across them calculated from the potential profiles (ΔV) and the recorded drain current (I_{DS}) values (Figure 3.6), using the Ohm's law:

$$R = \frac{\Delta V}{I_{\mathrm{DS}}} \tag{3.2}$$

For the calculation of the mean value of ΔV, we will consider the average of the scan profiles of the image in the vertical direction for each bias point. Since over the source electrode, at the semiconductor surface, a conduction channel always exists, we will use all the points on the source from the leftmost side in the image to the source edge touching the channel (X_{pixel} from 1 to 15; $X_{total} = 64$) for the calculation of source potential difference with respect to ground (0V). In the case of the channel, we will take the pixel from the right side of the source-channel interface ($X_{pixel} = 20$) and the left side of the channel-drain interface ($X_{pixel} = 43$). Finally, for the drain, we will consider the left side of the channel-drain interface ($X_{pixel} = 43$) and the right side of the channel-drain interface ($X_{pixel} = 49$). A similar procedure is used when calculating the values from a single scan profile at a particular location.

About the error bars, the standard deviation of all the points considered will be used. If a single scan line profile is used, then for the channel and drain no error bars based on standard deviations are defined as they are the difference between two point pixels only. The standard deviation of the drain current measured is calculated from the middle 10% of the total data points in Figure 3.6 traces. The error is properly propagated when taking the potential difference ($\Delta V_{xy} = V_y - V_x$) or calculating the resistance ($R = \Delta V / I_{\mathrm{DS}}$) from them, as per the below convention:

$$[\Delta V_{xy}]_{error} = \sqrt{([V_x]_{error})^2 + ([V_y]_{error})^2} \tag{3.3}$$

$$[R]_{error} = R \cdot \sqrt{\left(\frac{[\Delta V]_{error}}{\Delta V}\right)^2 + \left(\frac{[I_{\mathrm{DS}}]_{error}}{I_{\mathrm{DS}}}\right)^2} \tag{3.4}$$

For the calculation of the channel conductivities and corresponding error, we use the below relations:

$$\sigma_{channel} = \frac{L_{channel}}{R_{channel} \cdot W_{channel} \cdot h_{sem}} \tag{3.5}$$

$$[\sigma]_{error} = \sigma \cdot \left(\frac{R_{error}}{R}\right) \tag{3.6}$$

The calculation of ΔV is shown schematically for source, channel and drain resistances in Figure 3.13B for the case of scan line 15. Figure 3.13C shows the trends of corresponding resistances for the same scan line. The source resistance remains relatively constant as a function of drain voltage. On the other hand, the drain resistance shows significant drain voltage dependence, thereby absorbing most of the potential drop at high drain voltages. This dependence of drain resistance on drain voltage can also explain why the pinch-off doesn't extend into the channel, as observed in Figure 3.8(K-L). A similar lack of pinch-off in the channel due to the strong dependence of the drain resistance on drain voltage is reported in the n-type OFETs based on $PDI-FCN_2$ in the limiting case of a thin (6nm) semiconducting layer using gated four-probe measurements[14]. Another important point to note is that the relatively low channel resistance in the homogeneous section (scan line 15) suggests efficient intra-domain charge transport. However, significant voltage drops at the contacts and grain boundaries (scan line 4) act as a bottleneck for charge transport.

To explore further in detail and comprehensively, we created the electric potential maps for all drain and gate voltages noted in the relative electrostatic force image maps shown earlier in Figure 3.7. Figure 3.15 shows the electric potential maps, from where we straightaway see that the gate voltage at which the channel forms (track approximately the yellow-gold colour) is dependent on the drain voltage. This can be explained based on the lowering of overall channel capacitance that is coupled to the gate with increasing drain voltage, as the surface above the drain electrodes occupies increasing lower concentrations of charge carriers as drain voltage increases. Also, we see that the upper part of the image which contains the region where a single domain connects the source and drain turns on sooner than the one below where intersecting domains are present.

Anyway, from these potential maps, we can determine the dependence of different resistances as was done earlier in Figure 3.13, but now for all bias voltages. First, we look at the average dependence of different resistances calculated from the averaged/mean potential profiles, as explained earlier. In the following analysis, for the data points which are in the sub-threshold regime ($|V_{\mathrm{GS}}| < |VTH|$), the error bars will be huge, and the mean behaviour bit unclear, as can be expected from the potential maps shown in Figure 3.15.

Figure 3.16 shows the behaviour of the mean R_{source}. As we can see the average resistance for low drain voltages matches very well the series resistance ($R_s = 5k\Omega$) calculated from the Helmholtz model fitting at $V_{\mathrm{DS}} = 0V$ in Figure 3.3. At the high drain voltages, the pinch-off occurs for all the gate voltages considered as

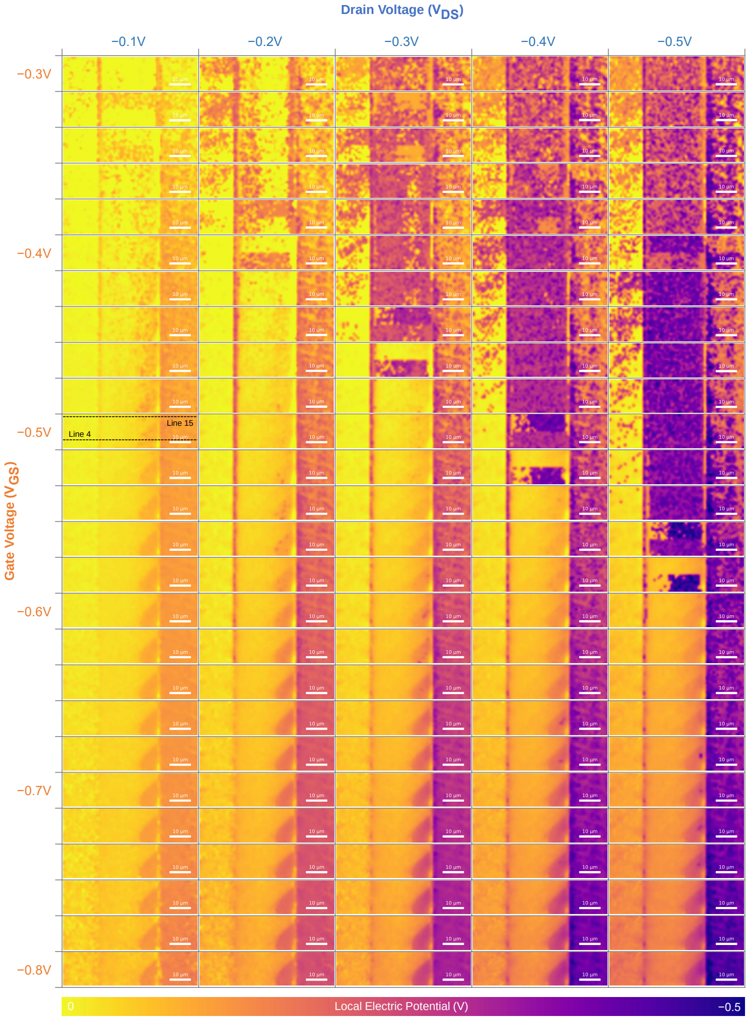

Figure 3.15: Electric Potential Maps for Bias Points shown in Figure 3.8. The scale bar is $10\mu m$. Experimental parameters same as in Figure 3.5.

shown earlier in Figure 3.8 which could affect the charge injection at the source and thus correspondingly, the source resistance is increased at high drain voltages (see Figure 3.16B).

Figure 3.17 shows the behaviour of the mean R_{Drain}. As we can see, the drain resistance is strongly dependent on both the gate and drain voltages in comparison to the source resistance shown earlier in Figure 3.16. The drain resistance

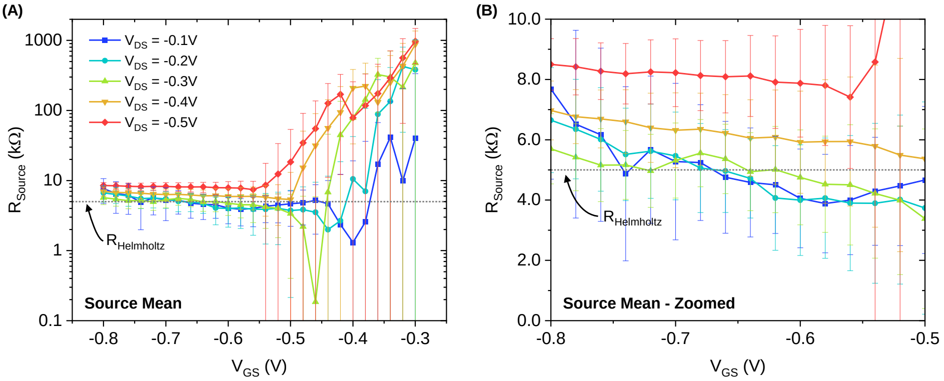

Figure 3.16: (A) Average source resistance as the function of drain and gate voltages, calculated from the averaged profiles of the potential maps shown in Figure 3.15. (B) Zoom of the graph in (A) of the section from $V_{GS} = -0.5V$ to $V_{GS} = -0.8V$. The dotted grey line in both graphs represents the series resistance calculated with the Helmholtz model fitting shown earlier in Figure 3.3.

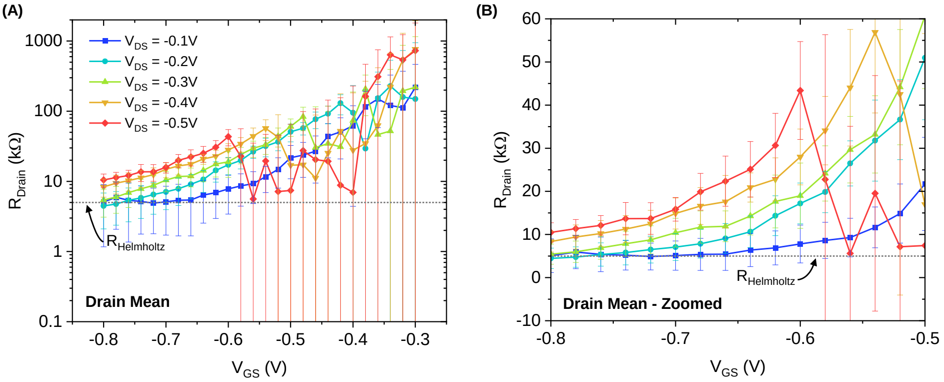

Figure 3.17: (A) Average drain resistance as the function of drain and gate voltages, calculated from the averaged profiles of the potential maps shown in Figure 3.15. (B) Zoom of the graph in (A) of the section from $V_{GS} = -0.5V$ to $V_{GS} = -0.8V$. The dotted grey line in both graphs represents the series resistance calculated with the Helmholtz model fitting shown earlier in Figure 3.3.

increases with drain voltage while decreases with increasing gate voltage. The drain resistance is always higher for non-zero drain voltages in comparison to the series resistance obtained at zero V_{DS} from the Helmholtz model. This is expected as the drain voltage directly decreases the charge carrier density over the drain electrode, as mentioned earlier.

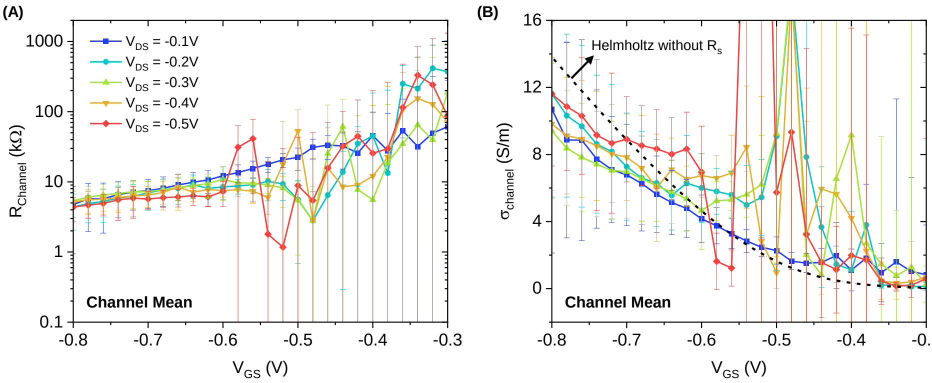

Figure 3.18: (A) Average channel resistance as the function of drain and gate voltages, calculated from the averaged profiles of the potential maps shown in Figure 3.15. (B) Average channel conductivity calculated using Equation 3.5. The dashed black line represents the average conductivity predicted by the Helmholtz model after removing the series resistance contribution as shown earlier in Figure 3.3.

Figure 3.18 shows the behaviour of the mean channel resistance ($R_{channel}$) and conductivity ($\sigma_{channel}$). The channel resistance is a function of gate voltage. However, in these averaged curves, the dependence of the drain voltage is not quite clear, that could be due to the presence of grain boundaries in the channel, which might lead to a complex behaviour. As we see later, for scan line 15 (Figure 3.19) which corresponds to the homogeneous section of the source-channel-drain region, the role of drain voltage becomes more clear. Anyway, the averaged channel conductivity calculated matches quite well with the one predicted from the Helmholtz model without series resistance effect (Figure 3.3), as shown in Figure 3.18B.

A similar analysis can be done for the homogenous section of the image, i.e. for the scan line 15. To assess what the behaviour would be for similar current densities if all the transistor area is uniform without grain boundaries, we assume that all the measured drain current (I_{DS}) flows through the scan line 15 for the calculation of resistances (Equation 3.2) or conductivities (Equation 3.5). Figure 3.19 shows the behaviour of various resistances and the channel conductivity. The behaviour of the source and drain resistances is similar to the average behaviour seen earlier. The

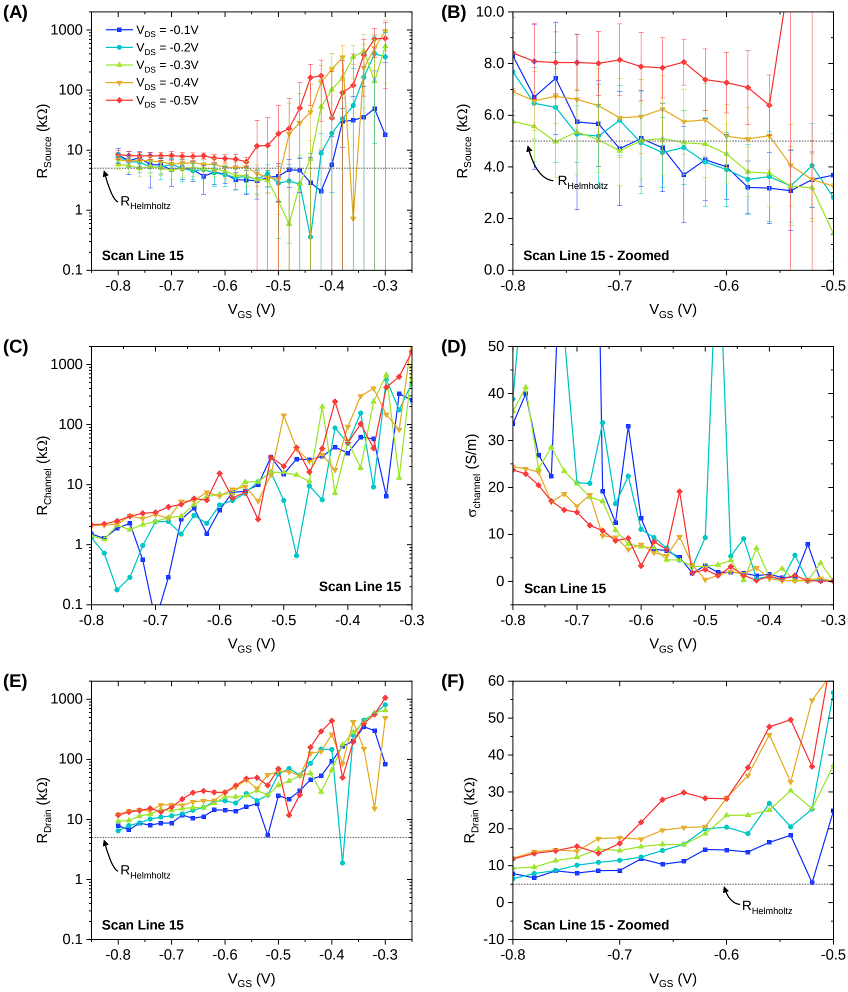

Figure 3.19: (A) Source resistance as the function of drain and gate voltages, calculated for the scan line 15 from the potential maps shown in Figure 3.15. (B) Zoom of the graph in (A) of the section from $V_{GS} = -0.5V$ to $V_{GS} = -0.8V$. (C) Channel resistance and (D) conductivity calculated for the scan line 15. (E) Drain resistance for the scan line 15 with its zoom in (F). The dotted grey line in the graphs represents the series resistance calculated with the Helmholtz model fitting shown earlier in Figure 3.3.

interesting behaviour is for the channel resistance which is 3-4 times lower than the averaged one and correspondingly the channel conductivity is 3-4 higher. Here, the behaviour of the channel conductivity with drain voltage is clear, which changes from $\sim 40\ S/m$ to $\sim 25\ S/m$ as the drain voltage increases. This is substantially higher than the averaged conductivity calculated earlier in Figure 3.18, which includes the effect of grain boundaries. These results again point to the fact that individual grain support superior charge transport properties, and the grain boundaries are one of the main causes of charge transport bottleneck. A fabrication or chemical modification strategy that could lead to a more conductive grain boundary can eliminate this bottleneck and make the charge transport morphology independent, which will be of tremendous importance for the development of high-performance large-area devices[13].

3.3. Conclusions

The impact of semiconducting thin-film microstructure on the local electrical properties is investigated and correlated with the crystalline domain microstructure visible from the polarised optical microscopy. Using the automated experimental setup developed earlier in Chapter 2, we performed comprehensive nanoscale operando characterization of EGOFETs in different operating regimes and under different microstructural signatures of the semiconducting thin film, providing direct detailed insights into their functional mechanism. The microstructural characteristics of the semiconducting thin-film control the multiscale evolution of electrical properties that are distinguished based on the pinch-off characteristics. In the presence of multiple intersecting grain boundaries along the charge carrier transport path from the source to the drain electrode, the pinch-off is extended and promoted inside the channel. In contrast, if a single domain bridges the source-drain electrode, the pinch-off is limited only over the drain electrode due to superior intra-domain charge transport and strong dependence of the drain access resistance on the drain and gate voltage. However, despite the differences in the nanoscale evolution of electrical properties, the overall effect is the same as that resulting in the drain current's saturation.

We used the interpretation framework developed earlier in Chapter 2 to obtain quantitative local electric potential maps of the EGOFET under different biasing conditions and extracted information about source, channel and drain resistances. It enabled quantifying the impact of contact access resistances and grain boundaries on the performance of the charge transport and pinpointing various charge transport bottlenecks. We observed that contact access resistance substantially reduces the conductivity of the overall semiconducting channel from $\sim 14\ S/m$ to

$\sim 4\ S/m$, while the microstructured nature of the semiconducting thin-film prevents the overall channel conductivity from reaching the level of a single domain conductivity of $\sim 40\ S/m$ (a total reduction by a factor of 10 in the performance). This indicates superior intra-domain charge transport with inferior inter-domain connectivity and electrical access to the contacting electrodes. Besides, the potential maps also consistently explained the unusual pinch-off characteristics observed earlier and provided quantitative rationales.

Our approach reported here opens new routes to obtain comprehensive quantitative insights into the charge carrier transport in electrolyte-gated transistors and pinpoint various bottlenecks. The straightforward approach to obtaining quantitative electric potential mapping is expected to make in-Liquid SDM an essential standard characterization tool for electrolyte-gated transistors.

3.4. References

1. F. Torricelli, D. Z. Adrahtas, Z. Bao, et al., “Electrolyte-gated transistors for enhanced performance bioelectronics,” *Nature Reviews Methods Primers*, vol. 1, p. 66, 2021. doi:10.1038/s43586-021-00065-8

2. A. Salleo, “Charge transport in polymeric transistors,” *Materials Today*, vol. 10, pp. 38–45, 2007. https://www.sciencedirect.com/science/article/pii/S1369702107700184

3. L. Balhorn, Q. MacPherson, K. C. Bustillo, C. J. Takacs, A. J. Spakowitz, and A. Salleo, “Closing the loop between microstructure and charge transport in conjugated polymers by combining microscopy and simulation,” *Proceedings of the National Academy of Sciences*, vol. 119, p. e2204346119, 2022. doi: 10.1073/pnas.2204346119

4. V. Palermo, M. Palma, and P. Samorì, “Electronic characterization of organic thin films by kelvin probe force microscopy,” *Advanced Materials*, vol. 18, pp. 145–164, 2006. doi:10.1002/adma.200501394

5. F. Mariani, F. Conzuelo, T. Cramer, et al., “Microscopic determination of carrier density and mobility in working organic electrochemical transistors,” *Small*, vol. 15, p. 1902534, 2019. doi:10.1002/smll.201902534

6. A. Kyndiah, M. Checa, F. Leonardi, et al., “Nanoscale mapping of the conductivity and interfacial capacitance of an electrolyte-gated organic field-effect transistor under operation,” *Advanced Functional Materials*, vol. 31, p. 2008032, 2021. doi:10.1002/adfm.202008032

7. R. Li, J. W. Ward, D.-M. Smilgies, et al., “Direct structural mapping of organic field-effect transistors reveals bottlenecks to carrier transport,” *Advanced Materials*, vol. 24, pp. 5553–5558, 2012. doi:10.1002/adma.201201856

8. A. B. Naden, J. Loos, and D. A. MacLaren, “Structure–function relations in dif-tes-adt blend organic field effect transistors studied by scanning probe microscopy,” *Journal of Materials Chemistry C*, vol. 2, pp. 245–255, 2014. doi:10.1039/C3TC31783H

9. L. Huetter, A. Kyndiah, and G. Gomila, “Analytical physical model for electrolyte gated organic field effect transistors in the helmholtz approximation,” *Advanced Theory and Simulations*, vol. 6, p. 2200696, 2023. doi:10.1002/adts.202200696

10. Q. Zhang, A. Tamayo, F. Leonardi, and M. Mas-Torrent, “Interplay between electrolyte-gated organic field-effect transistors and surfactants: A surface aggregation tool and protecting semiconducting layer,” *ACS Applied Materials & Interfaces*, vol. 13, pp. 30 902–30 909, 2021. doi:10.1021/acsami.1c05938

11. A. Kyndiah, F. Leonardi, C. Tarantino, et al., “Bioelectronic recordings of cardiomyocytes with accumulation mode electrolyte gated organic field effect transistors,” *Biosensors and Bioelectronics*, vol. 150, p. 111844, 2020. https://www.sciencedirect.com/science/article/pii/S0956566319309236

12. Q. Zhang, F. Leonardi, S. Casalini, I. Temiño, and M. Mas-Torrent, “High performing solution-coated electrolyte-gated organic field-effect transistors for aqueous media operation,” *Scientific Reports*, vol. 6, p. 39623, 2016. doi:10.1038/srep39623

13. S. Hunter and T. D. Anthopoulos, “Observation of unusual, highly conductive grain boundaries in high-mobility phase separated organic semiconducting blend films probed by lateral-transport conductive-afm,” *Advanced Materials*, vol. 25, pp. 4320–4326, 2013. doi:10.1002/adma.201300020

14. Rödel, Reinhold, “Contact resistance effects in organic n-channel thin-film transistors,” PhD thesis, Lausanne, EPFL, 2016. doi:10.5075/EPFL-THESIS-6805

Chapter 4

Multimodal Characterisation of Operating OECTs

Abstract In contrast to EGOFETs (introduced earlier in Chapter 1 and investigated thoroughly in Chapter 3), OECT involves the penetration of ions in the bulk of the semiconductor in response to applied gate voltage to modulate the conductivity of the channel causing appreciable bias-dependent physical changes and consequently represents a more complex system. The operating mechanism of OECT relies on the interplay between both ionic and electronic transport, which is uniquely tied to the semiconductor's morphological and mechanical response, as mentioned earlier in Chapter 1. Such correlated electrical-mechanical behaviour in conventional device architecture spanning source-channel-drain region and under operating conditions are not yet reported. Using automated in-Liquid Scanning Dielectric Microscopy as described in Chapter 2, we demonstrate bias-voltage-dependent correlated electrical and mechanical behaviour in an operating n-type OECT based on poly(benzimidazobenzophenanthroline) (BBL) in an aqueous electrolyte environment. The interest in studying this polymer stems from the fact that despite the absence of polar side chains, the electrical performance of BBL OECTs outperforms other OECTs based on polymers with hydrophilic side chains. Also, the remarkable operational stability of the BBL OECT is favourable for comprehensive long-term experimental probing. In this investigation, we correlated the spatial variability in local stiffness represented by the mechanical slope (m) with the measured local electrostatic forces in different operating regimes. The occurrence of a stable operating regime (negative transconductance

or anti-ambipolarity) is identified at high doping concentrations, and the resulting current-voltage characteristics in this operating regime are explained. A peculiar sudden phase change is noticed that always transpires at maximum transconductance points whenever it occurs. The present results represent significant advances in multimodal and multiscale operando characterization of OECTs and aid in deciphering the spatially resolved bias-dependent local structure-property-function relationships in functional devices.

4.1. Introduction

As detailed in Chapter 1 subsection 1.4.2, Organic Electrochemical Transistors (OECTs) have received significant attention due to their unique way of coupling ionic and electronic charges and their transport phenomena, attracting diverse applications ranging from neuromorphic computing to bioelectronics, sensors, and circuit elements[1].

Besides the favourable characteristics common with EGOFETs, OECT's tunable mechanical characteristics in response to applied bias potentials offer another dimension for efficient interfacing with cells and tissues. Although, this makes them slow in comparison to EGOFETs generally. Nonetheless, they are the most popular class of electrolyte-gated transistors at present, and significant attention is paid to mixed ionic-electronic conducting polymers, commonly known as OMIECs[2]. This is not surprising as they offer another degree of freedom to explore, namely, the mechanical properties.

In spite of this shared interest, there is a serious lack of understanding of local structure-property-function relationships as very limited techniques can work in liquid environments and probe different modalities which are necessary to accurately evaluate the device operating mechanism. Many recent literature reviews[2–4] have put forth the need for developing new multimodal techniques, which this thesis aims to address, as also mentioned earlier in Chapter 1 (section 1.7).

This chapter starts with the macroscale device current-voltage characterization and identification of different operating regimes, with a special focus on the negative transconductance regime, also known as anti-ambipolarity[5], which occurs stably in the studied OECTs. Then we move to the morphological characterization with standard AFM and see how the polymer thickness, roughness and mechanical properties change as a function of gate voltage. Thereafter, we explore the

OECT during operation with the automated in-Liquid SDM technique, correlate the electrical and mechanical behaviour and explain the macroscale device IV characteristics with a focus on negative transconductance regime and maximum transconductance points. Finally, we conclude with open questions to address in future studies.

4.2. Results and Discussion

We investigated OECT based on poly(benzimidazobenzophenanthroline) (BBL), which is a state-of-the-art n-type homogeneous π-conjugated redox polymer where ionic and electronic processes are not phase separated and thus demands probing of individual and coupled processes simultaneously, making it a perfect testbed for our studies. The BBL-based devices have shown remarkable volumetric capacitance and stability even at high doping concentrations, with overall performance reaching that of the state-of-the-art p-type devices. The transistors studied in this chapter were fabricated by Han-Yan Wu and Chi-Yuan Yang in the group of Prof. Simone Fabiano at Linköping University, Sweden[†].

4.2.1. Macroscale Characterization of OECTs

The schematic for post-operando and in-operando characterization of the OECTs is shown in Figure 4.1A and Figure 4.1B. The schematic is similar to the one for EGOFETs shown earlier in Figure 3.1, except for a few changes. A Tungsten (W) external gate electrode is used here instead of Platinum (Pt). The polarity of the voltages is different since n-type OECT is used. The architecture of the transistor is also different (not interdigitation), as shown in Figure 4.1C and Figure 4.1D corresponding to $W/L = 100\mu m/10\mu m$ and $W/L = 20\mu m/10\mu m$ respectively with a nominal channel thickness of $h_{sem} = 20nm$. Also, as mentioned earlier, the penetration of ions takes place in response to applied gate potential, which is shown schematically in the figures.

Figure 4.2 shows the transfer and output characteristics of the device measured in 10mM NaCl solution under in-operando and post-operando configuration shown in Figure 4.1 earlier. The transfer characteristics show the typical behaviour of an

---

[†] Lab website: https://liu.se/en/research/laboratory-of-organic-electronics

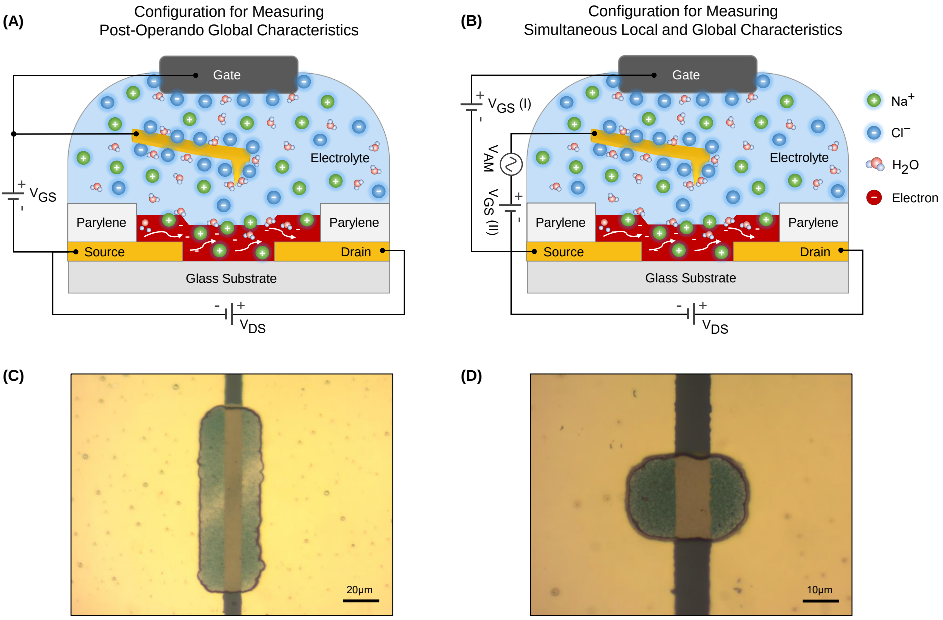

Figure 4.1: (A) Experimental configuration for post-operando device I-V characterization, only DC gate voltage (V_{GS}) is applied to the junction connecting both gold SDM probe and external tungsten gate electrode from the same power source, and V_{DS} is applied between source and drain electrodes. (B) Experimental configuration for simultaneous local and global characterization where the gold SDM probe is biased with the DC gate voltage (V_{GS}) offset to amplitude-modulated (V_{AM}) waveform, and the external tungsten gate electrode is biased with just DC gate voltage (V_{GS}). (C) Optical microscopy image of the device with nominal channel length L=10μm, width W=100μm (W/L=10), and thickness h_{sem}=20nm. (D) Optical microscopy image of the device with nominal channel length L=10μm, width W=20μm (W/L=2), and thickness h_{sem}=20nm.

accumulation mode transistor up to intermediate gate voltages, thereafter the drain current starts decreasing, giving an inverted-V-shape drain current response and are consequently termed either as a negative transconductance regime[6] or an anti-ambipolar behaviour[7]. An ambipolar transistor exhibits a V-shaped drain curves response and transports both electrons and holes, it is the opposite behaviour here. The output characteristics show typical operating regimes, namely sub-threshold, linear and saturation, with an addition of a new negative transconductance regime. As can be seen from Figure 4.2B for $V_{\mathrm{GS}} = 0.6V$, $0.7V$ and $0.8V$, the negative transconductance regime results in a shift of drain current onset that increases with increasing gate voltage.

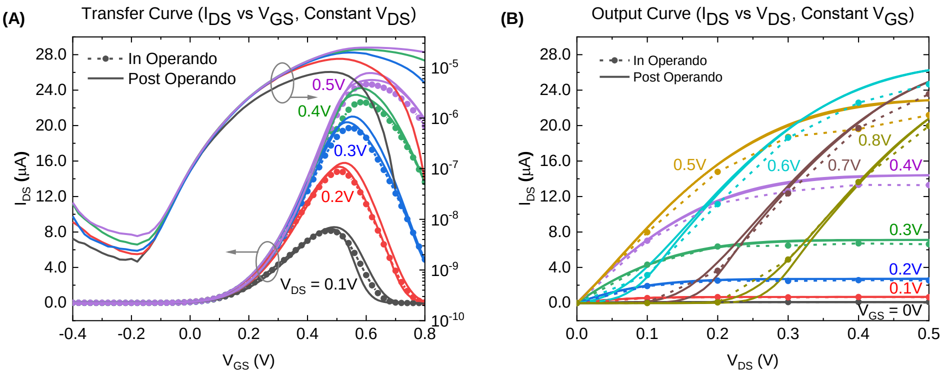

Figure 4.2: (A) Transfer and (B) Output I-V characteristics of one of the OECT analyzed with $W/L = 100/10\mu m$ in 10mM NaCl solution. The symbols with dotted lines correspond to the average drain current measured during in-liquid SDM while the continuous lines refer to an post-operando I-V measurement performed after the full set of in-liquid SDM measurements.

With the addition of this operating regime, it would be interesting to see how the local electrical and mechanical properties change. Before that, we first look at how the polymer thickness, roughness and stiffness change in response to applied gate voltage, using the standard AFM force-volume quantitative (QI) imaging method (it is basically the same as the one used for in-Liquid SDM except that no voltages are applied during imaging).

4.2.2. Morphological Characterization of OECTs

For appropriate quantification of the thickness of the semiconductor with changing gate voltage, we need access to the substrate region which can be imaged simultaneously, otherwise, the drifts of the AFM system will not allow accurate quantification of the thickness. To do so, we identified a region where the polymer film was ripped off the surface which could happen either during the fabrication or during imaging accidentally as shown in Figure 4.3. Nevertheless, it provides the perfect opportunity to probe the change in thickness of the polymer as a function of gate voltage.

The transistor was in pristine condition (i.e. dried sufficiently) before the start of thickness vs gate voltage measurements. The first measurement was done in dry, and then the second was when exposed to 10 mM NaCl solution without any prior

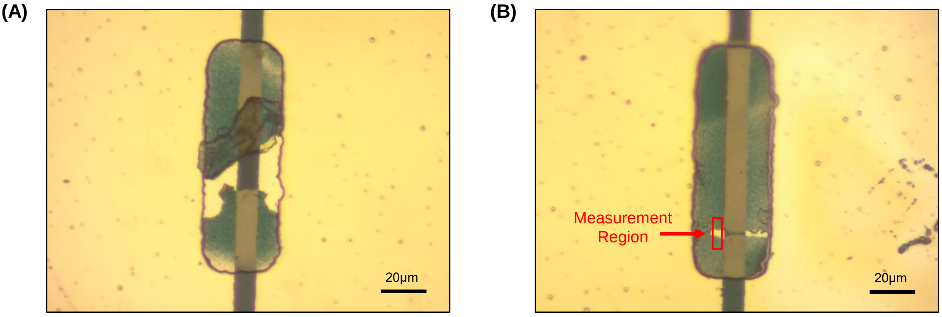

Figure 4.3: Transistors showing ripped-off polymer thin-film that accidentally happened during (A) fabrication and (B) imaging. The ripped-off region provides the perfect opportunity for thickness measurement as a function of gate voltages. The red rectangle shows the region where measurements are done.

electrical connection with the source-measure unit (SMU), then the third after making the electrical connections and finally, the measurements were done with increasing gate voltage or doping state of the polymer with the automated python-based experimental setup as described earlier in Chapter 2. In these measurements, only the AFM tip is used as the gate electrode and only the source electrode is connected to the ground while the drain is floating since the measurement region lies solely on one electrode which is set as the source. At each gate voltage, the transistor is stressed for 60 seconds, and then after a wait of 15 seconds, the imaging starts in the force-volume mode without any voltage application. The gate (V_{GS}) voltage is changed from $-0.4V$ to $0.8V$ in steps of $\Delta V_{\mathrm{GS}} = 50mV$, giving rise to 25 measurements with gate voltage applied and a total of 3+25=28 measurements in different conditions (the three extra measurements are the one defined earlier: one in dry, one with exposure to 10mM NaCl and one after making electrical connections).

Figure 4.4(A-D) shows a few of the topographic images in different conditions and their corresponding histograms in Figure 4.4E. The images are flattened with respect to the polymer surface on the right and left side of the image, so it is kept at $0nm$. As evident, we do see significant changes in different conditions. The exposure to electrolytes causes noticeable changes in the thickness; however, putting the device in the bias circuitry with turned-off power sources also significantly increases the polymer thickness, probably due to the triggering of energy level alignments. Because of this observation, we remark that utmost caution

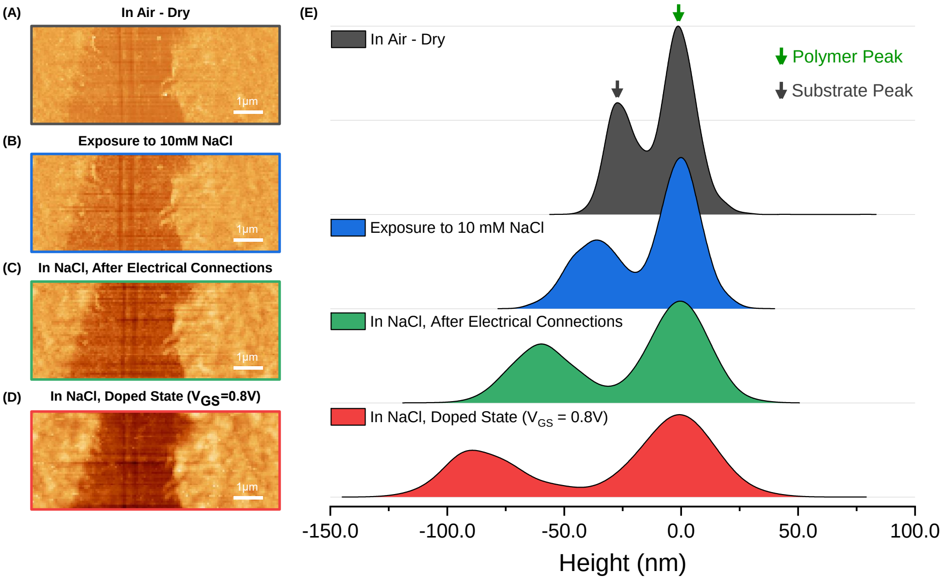

Figure 4.4: Topography of the region marked with a red rectangle in Figure 4.3 in (A) dry conditions, (B) when exposed to the 10mM NaCl solution, (C) in 10mM NaCl solution after making electrical connections and (D) in doped state at $V_{GS} = 0.8V$ in 10mM NaCl solution. (E) The corresponding histograms of the topographies with the substrate (grey arrow) and the polymer (green arrow) peaks marked. The images are flattened with respect to the polymer surface on the right and left side of the image, so it is kept at $0nm$.

needs to be taken in quantifying the water and ion uptake leading to polymer thickness change with mere electrolyte exposure as the bias circuitry needs to be disconnected entirely, especially when using other standard techniques like electrochemical quartz crystal microbalance (eQCM) gravimetry.

To quantify, the histograms of the topography for different conditions are fitted with a bimodal of two normal distributions using the relation:

$$f(x) = A_1 \cdot e^{-\frac{1}{2}\left(\frac{x-\mu_{h_{sem}}}{\sigma_{h_{sem}}}\right)^2} + A_2 \cdot e^{-\frac{1}{2}\left(\frac{x-\mu_{h_{subs}}}{\sigma_{h_{subs}}}\right)^2} \tag{4.1}$$

with one Gaussian distribution representing the polymer peak and another the substrate peak. To not confuse with the mobility (μ) and conductivity (σ) symbols, h_{sem} or h_{subs} are used with these symbols to represent that they are the mean and standard deviations of the semiconductor and substrate height respectively. The difference in the fitted peak positions from the histograms ($\mu_{h_{subs}} - \mu_{h_{sem}}$) will tell the change of thickness of the polymer and the polymer peak's standard deviation ($\sigma_{h_{sem}}$) will tell about the polymer surface roughness. Figure 4.5 shows the bimodal fitting of the histogram of topography for one of the gate voltages ($V_{\text{GS}} = 0.8V$).

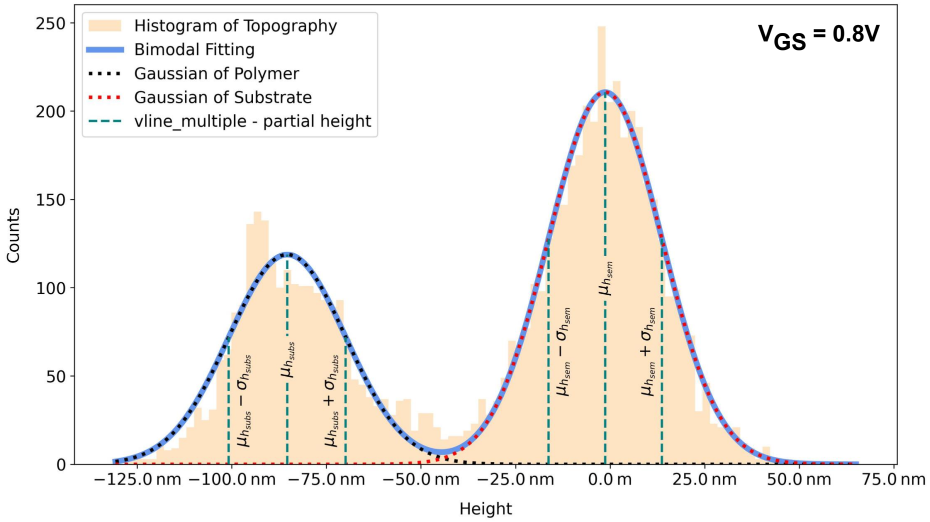

Figure 4.5: Bimodal fitting of the histogram of topography for $V_{\text{GS}} = 0.8V$, used for calculating the polymer thickness ($\mu_{h_{subs}} - \mu_{h_{sem}}$) and roughness ($\sigma_{h_{sem}}$).

Figure 4.6 graphs how the thickness changes in different conditions and at different gate voltages measured. The standard deviation of the polymer peak ($\sigma_{h_{sem}}$) is plotted as error bars. As we can see, the roughness of the polymer thickness increases substantially from the dry state. In the case of increasing gate voltage dataset, the thickness stays constant from the start of gate voltage application up to a threshold gate voltage, thereafter it increases gradually as the doping state of the polymer increases. The thickness increases to more than three times the original thickness in the dry state from $25nm$ to $83nm$, representing a rich and emerging behaviour of BBL OECTs.

In the next section, we explore the electrical and mechanical behaviour simultaneously across various regimes.

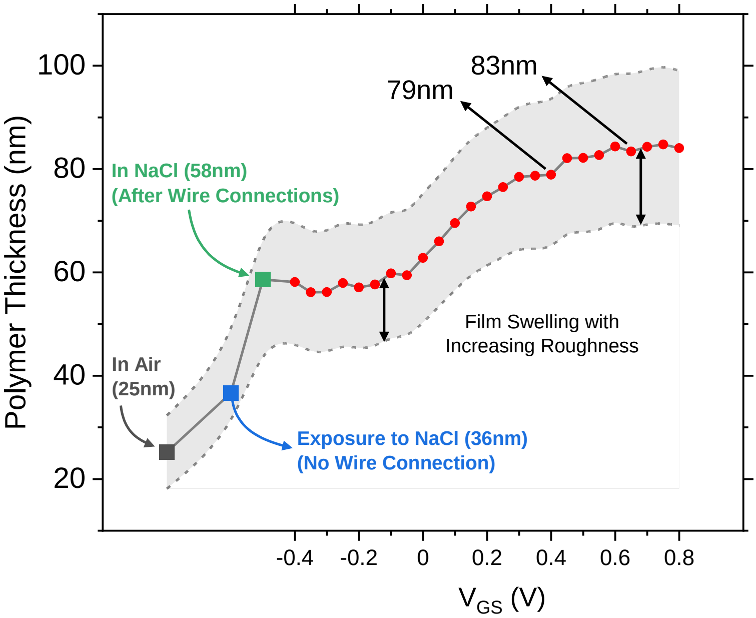

Figure 4.6: The polymer thickness in different conditions and at different gate voltages measured.

4.2.3. Nanoscale Multimodal Characterization of OECTs

In-liquid SDM measurements following the approach described in Chapter 2 were performed on a $30 \times 5.625 \mu m^2$ region spanning source-channel-drain area, shown by its topography in Figure 4.7. The measurements are performed starting from the pristine conditions (i.e. the OECT is dried sufficiently and with no prior bias application after putting in the solution). The thickness of the polymer as determined from the topography profile in Figure 4.7B due to the presence of a small hole is $35nm$, which is very close to what is expected from the graph (blue datapoint: $36nm$) in Figure 4.6.

The in-Liquid SDM measurements span for gate voltages (V_{GS}) from $-0.4V$ to $0.8V$ with $\Delta V_{\mathrm{GS}} = 20mV$ and drain voltages (V_{DS}) from $0V$ to $0.5V$ in steps of $\Delta V_{\mathrm{DS}} = 100mV$, covering all the operating regimes of interest, namely, sub-threshold, linear, saturation and negative transconductance regime. The simultaneously recorded drain current versus time traces during operando in-Liquid SDM for all the measured operating points are shown in Figure 4.8, along with

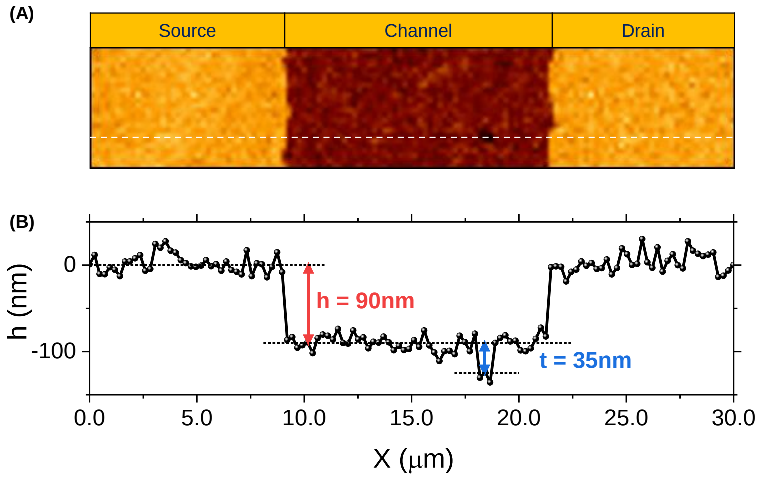

Figure 4.7: (A) OECT topography of the $30 \times 5.625 \mu m^2$ region spanning source-channel-drain area. (B) Topography profile along the dashed white line shown in (A). The semiconducting polymer thickness ($35 nm$) and electrode thickness ($90 nm$) are highlighted.

the time window where imaging is done. These traces are used to reconstruct the in-operando transfer and output curves shown earlier in Figure 4.2 with dotted lines and symbols. Remarkably, these reconstructed curves are consistent with post-operando device characterization performed after operating the transistor for approximately nine hours for 366 in-Liquid SDM measurements (1min 25sec each), demonstrating the high stability of the device. Figure 4.9 shows relative electrostatic force images and Figure 4.10 shows the corresponding mechanical stiffness maps for all the drain and gate voltages analyzed.

As mentioned in Chapter 2 and as was the case with EGOFETs in Chapter 3, the changes in electrostatic force at a specific pixel are directly linked to the local conductivity changes at that point, assuming conductivity is the sole electrical property affected by bias voltages. However, in the case of OECTs, the penetration of ions happens into the bulk of the semiconductor which substantially changes the effective Stern interfacial or 3D bulk fixed capacitance (which in the case of EGOFETs was assumed constant) as a function of bias voltages. Therefore, the electrostatic force measured in the case of OECTs depends on both the local conductivity and effective 3D interfacial capacitance. This dual dependence makes the behaviour of measured electrostatic force complex but at the same, it is advantageous as we can indirectly track the ions penetration or hydration of

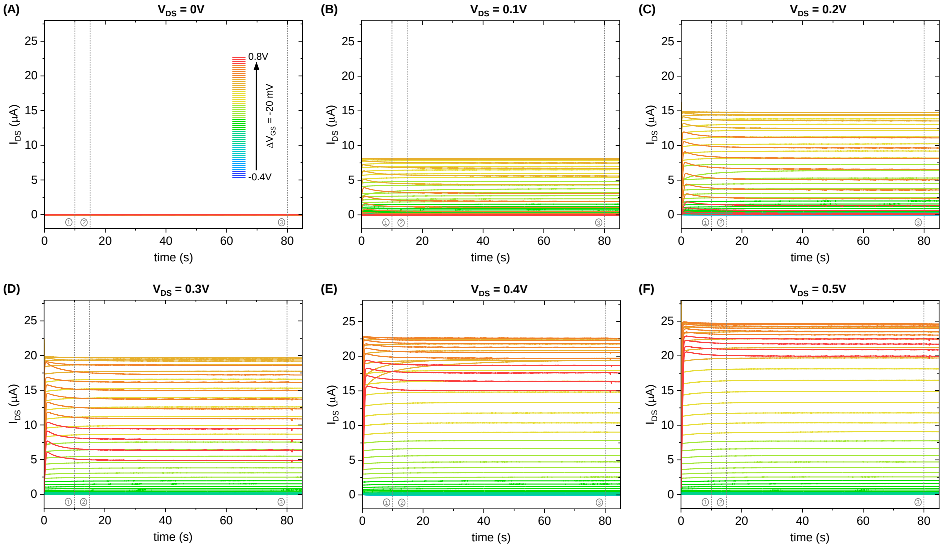

Figure 4.8: I_{DS} vs time evolution during operando in-Liquid SDM measurements (A) I_{DS} vs time traces for V_{GS} from $-0.4V$ to $0.8V$ and V_{DS} (A) $0V$, (B) $0.1V$, (C) $0.2V$, (D) $0.3V$, (E) $0.4V$, and (F) $0.5V$. The legends are the same for all graphs, so they are displayed only for the case of $V_{\text{DS}} = 0V$. For each measurement, at $time = 0s$, the bias voltages (V_{GS} and V_{DS}) are applied, and after a wait of $10s$ (denoted by the dotted line ① in the graph) the SDM probe is approached to the surface, thereafter it waits for $5s$ more (denoted by the dotted line ② in the graph) before starting the imaging. The single image takes $65s$, and then the tip is retracted (denoted by the dotted line ③ in the graph), and then the bias voltages are kept for $5s$ more before turning them off.

the polymer electrically, besides the direct access through mechanical stiffness mapping. This allows corroborating findings with each other modalities. The dependence of electrostatic force on the conductivity and interfacial capacitance is discussed in Chapter 1 (subsection 1.6.4), which we will extensively use here to explain the results qualitatively.

The individual nanoscale electrical and mechanical images shown in Figure 4.9 and Figure 4.10 are quite uniform in the vertical direction. So, to simplify the analysis, we reconstruct a single merged image by considering all gate voltages together for each drain voltage, where a scan line is an average of an image in the vertical direction, giving us the spectrums of the local property as a function of gate voltages while preserving the longitudinal variation across the source-channel-drain region.

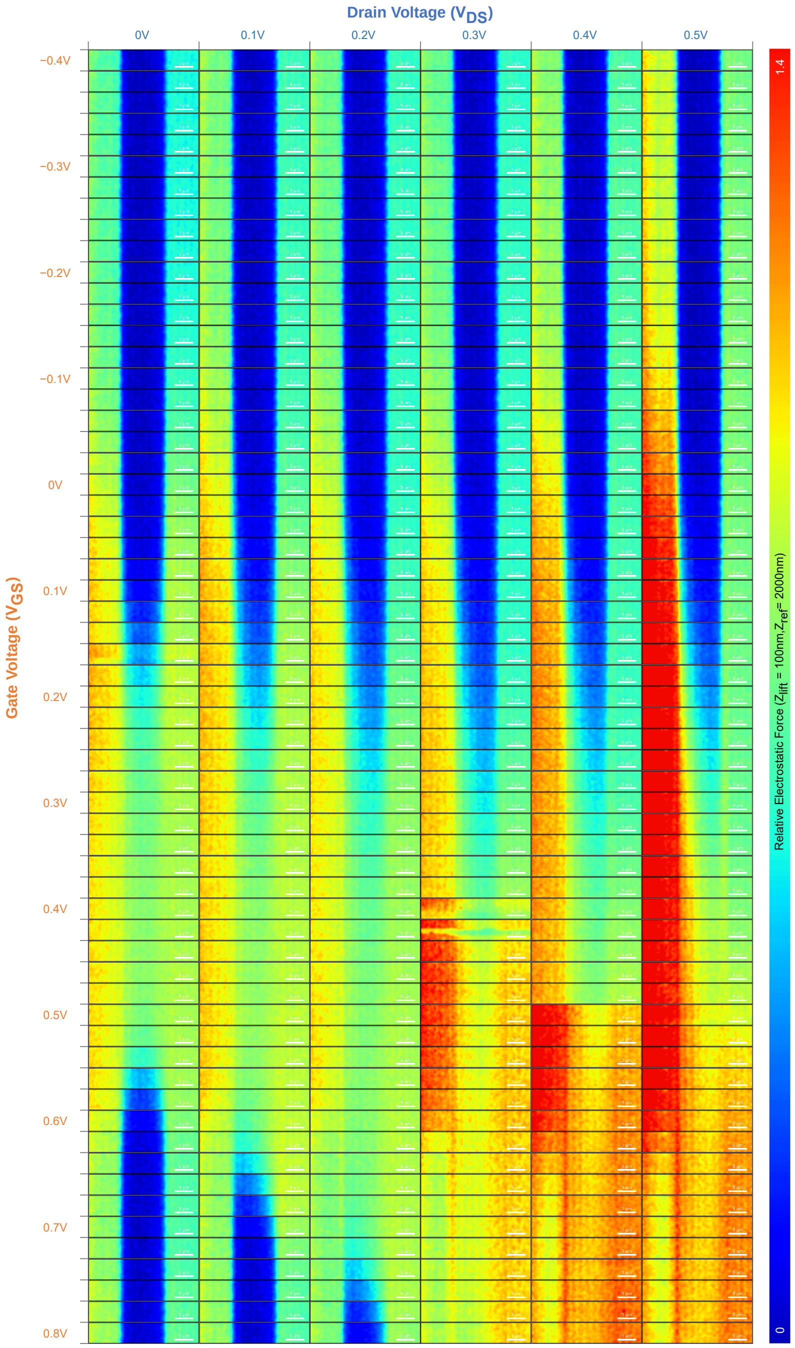

Figure 4.9: Nanoscale Electrical Probing of OECT. Lift-mode relative electrostatic force images ($Z_{lift} = 100nm$ and $Z_{ref} = 2000nm$) for V_{GS} ($\Delta V_{\mathrm{GS}} = 20mV$) and V_{DS} ($\Delta V_{\mathrm{GS}} = 100mV$) voltages covering all operating regimes. The scale bar is $5\mu m$.

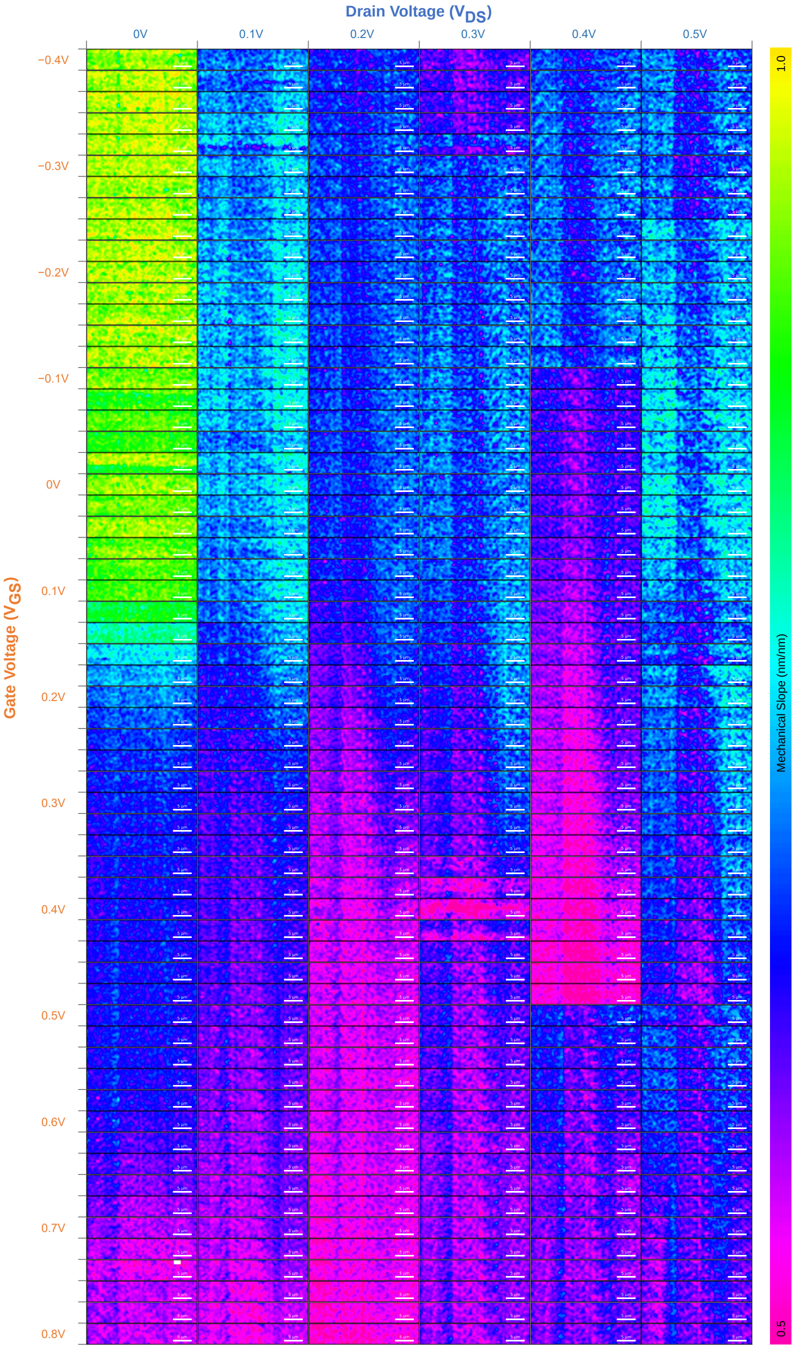

Figure 4.10: Nanoscale Mechanical Probing of OECT. Mechanical slope (m) images for V_{GS} ($\Delta V_{\text{GS}} = 20mV$) and V_{DS} ($\Delta V_{\text{GS}} = 100mV$) voltages covering all operating regimes. The scale bar is $5\mu m$.

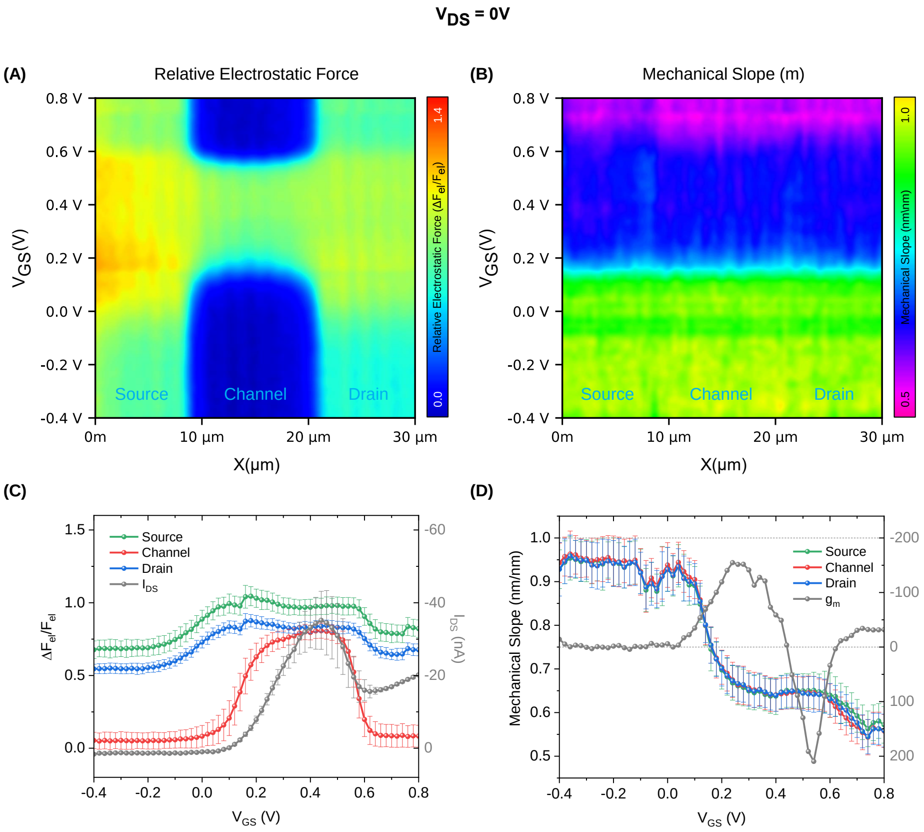

Figure 4.11: Multimodal Measurements at $V_{\mathrm{DS}} = 0V$ (A) Relative electrostatic force vs gate voltage spectrum of the source-channel-drain cross-section of the OECT reconstructed from Figure 4.9 by averaging images in the vertical direction, similarly (B) Mechanical slope (m) spectrum reconstructed from Figure 4.10. (C) Relative electrostatic force trends over the whole source, channel and drain regions, along with the reconstructed transfer curve obtained from the operando drain current recording in Figure 4.8 by averaging over the whole scan duration. Similarly, (D) Mechanical trends along with the transconductance curve by taking the derivative of the reconstructed transfer curve.

Figure 4.11 shows such a spectrum of relative electrostatic force versus gate voltage (A) and another for mechanical slope versus gate voltage (B) at $V_{\mathrm{DS}} = 0V$. These spectrums are to be read from bottom to top, where the bottom indicates the low gate voltages and the top high gate voltages. The source, channel and drain regions are also highlighted. As we see, as the gate voltage increases, the (relative) electrostatic force increases first on the electrodes and later in the channel, see Figure 4.11C. This is due to the different sensitivity ranges of the in-liquid SDM to the conductivity on the electrodes and on the channel, see Figure 1.20 for the simulations. These simulations are for the isotropic transport in transverse and longitudinal directions and in such cases, the conductivity axis can be considered equivalent to the gate voltage, any shift in the conductivity range is a shift in the gate voltage. However, for an anisotropic case, such as in the EGOFETs studied in Chapter 3, the conductivity increases faster in the channel by a factor determined by the anisotropy. For a high enough factor, the sensitivity gate voltage range (not conductivity) of the in-liquid SDM is the same for the electrodes and for the channel, such as in the EGOFETs studied in Chapter 3.

The electrostatic force in the channel increases at the same gate voltage (threshold) at which the recorded drain current increases, see Figure 4.11C. As a side note, since the measurements are done at $V_{\mathrm{DS}} = 0V$ (not short-circuited Source-Drain), the recorded drain current stems from the difference in the gate-source and gate-drain current path. Ideally, it is an electrically equal path especially when source and drain are shorted causing equal gate current distribution between source and drain and thus leading to a zero drain current[8]. However, it is not the case here as also seen from the difference in the measured electrostatic forces on the source and drain. Nonetheless, we can use the recorded drain current for making inferences.

Coming back to the Figure 4.11C, as the voltage increases past the threshold, the electrostatic force increases and then saturates. This saturation in the force is not linked to saturation in the conductivity, instead, it is due to a convoluted response with the sensitivity of in-liquid SDM. Beyond a particular conductivity value (different for electrodes and channel), the response of the electrostatic force saturates as a function of conductivity, as clear from earlier referred simulations in Figure 1.20. In this range of conductivity, we are not sensitive to the conductivity changes anymore, although changes in interfacial capacitances can be tracked. As the gate voltage keeps on increasing, the channel electrostatic starts decreasing concurrent with the decrease in the recorded drain current. At this point, the OECT enters the negative transconductance regimes, see the transconductance curve in Figure 4.11D on the right y-axis. The electrostatic force decreases uniformly in the channel (Figure 4.11A) at high gate voltages.

The mechanical response exhibits interesting behaviour as well (Figure 4.11B and Figure 4.11D). The semiconducting polymer is initially hard for the chosen cantilever (cantilever deflection sensitivity, $s = 24.19 nm/V$ and cantilever spring constant $k_{cantilever} = 1.201 N/m$), as indicated by the mechanical slope (m) value being closer to one, refer subsection 2.2.2 for more information on the mechanical slope. Once the gate voltage surpasses the threshold, the semiconducting polymer starts becoming softer and then reaches a plateau at intermediate gate voltages. Once, the gate voltage enters the negative transconductance regime, a further increase in the mechanical slope is observed indicating that the material becomes more softer in this regime. The softening of the semiconducting polymer is a direct signature of ion penetration into the polymer bulk. Also, it appears that when the plateau starts and ends, the maximum positive and negative transconductance occurs respectively.

It is important to ensure that the changes seen here are not due to the electrostatic effects or is in correlation with the electrostatic force throughout the gate voltages analyzed. As we see, from the Figure 4.11D itself, the mechanical slope seems to be anti-correlated with force at lower gate voltages and in direct correlation at the high gate voltages in the negative transconductance regime, indicating that mechanical slope probes different modalities, where the correlation and anticorrelation behaviour is arising due to nature of ionic-electronic coupling as a function of charge carrier density in these materials. To further assure, we look at the case of EGOFETs analyzed in Chapter 3, and see how the mechanical slope changes as a function of drain and gate voltages. The EGOFET measurements are also done in pristine conditions and with the same type of cantilevers (cantilever deflection sensitivity, $s = 36.65 nm/V$ and cantilever spring constant $k_{cantilever} = 1.097 N/m$).

Figure 4.12 shows the mechanical behaviour of EGOFETs as a function of drain and gate voltages for the dataset shown in Figure 3.7. As it is quite clear, EGOFETs don’t show modulation in mechanical properties whatsoever as expected since EGOFETs are interfacial devices and no ion penetration happens into the bulk of the semiconductor in the stable gate voltage operation window. These results indicate that mechanical slope indeed probes the material’s mechanical properties and is a direct signature of ion uptake by the organic semiconductors upon doping by the gate voltage.

This multimodal electrical and mechanical response of OECTs is probed further at non-zero drain voltages. After the measurements at zero drain voltage, a non-zero drain voltage is applied, starting with $V_{\mathrm{DS}} = 0.1V$ and ending with $V_{\mathrm{DS}} = 0.5V$ in steps of $\Delta V_{\mathrm{DS}} = 100mV$, and at each drain voltage, the gate voltage is scanned

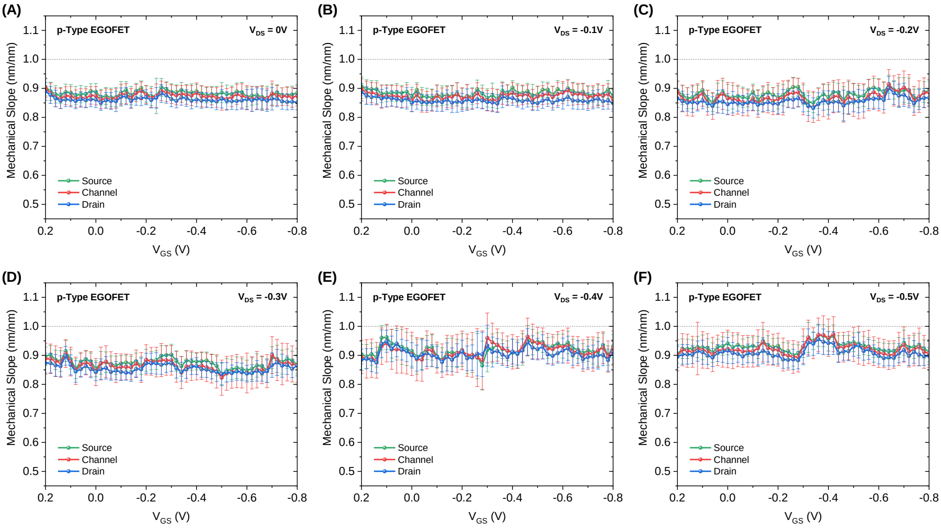

Figure 4.12: Mechanical slope (m) trends for the EGOFET data shown in Chapter 3 Figure 3.7. The slope stays more or less constant and does not show the modulation in the mechanical properties as the function of gate voltage since the ions do not penetrate the channel in EGOFETs (a key distinction, refer section 1.4).

from $-0.4V$ to $0.8V$, as was done for $V_{\mathrm{DS}} = 0V$ case, to see how the polymer response changes in subsequent gate voltage cycling.

Figure 4.13 shows the similar figure as Figure 4.11 but for $V_{\mathrm{DS}} = 0.1V$. Looking at Figure 4.13A, an asymmetry in the electrostatic force is observed when a non-zero drain voltage is applied, as was the case with EGOFETs. The applied drain voltage decreases the effective gate voltage spatially, leading to an asymmetry in the conductivity over the source-channel-drain region which is reflected in the measured (relative) electrostatic force, notice the shift in drain curve in Figure 4.13C. The mechanical response also shows an asymmetry, see Figure 4.13B and Figure 4.13D. Interestingly, the mechanical slope didn't start from the initial hard levels seen in Figure 4.11A, which indicates that there is some irreversibility in the mechanical behaviour. This could be attributed to the hydration of the BBL polymer which is accomplished in the first gate voltage cycle and in the second cycle the polymer is more hydrated. A recent study by Guo and Ginger et al.[9] reported that the seemingly hydrophobic side-chain-free BBL polymer could readily undergo hydration in the initial doping cycle and is irreversible, thus in corroboration with our findings of irreversible mechanical behaviour. Also, again

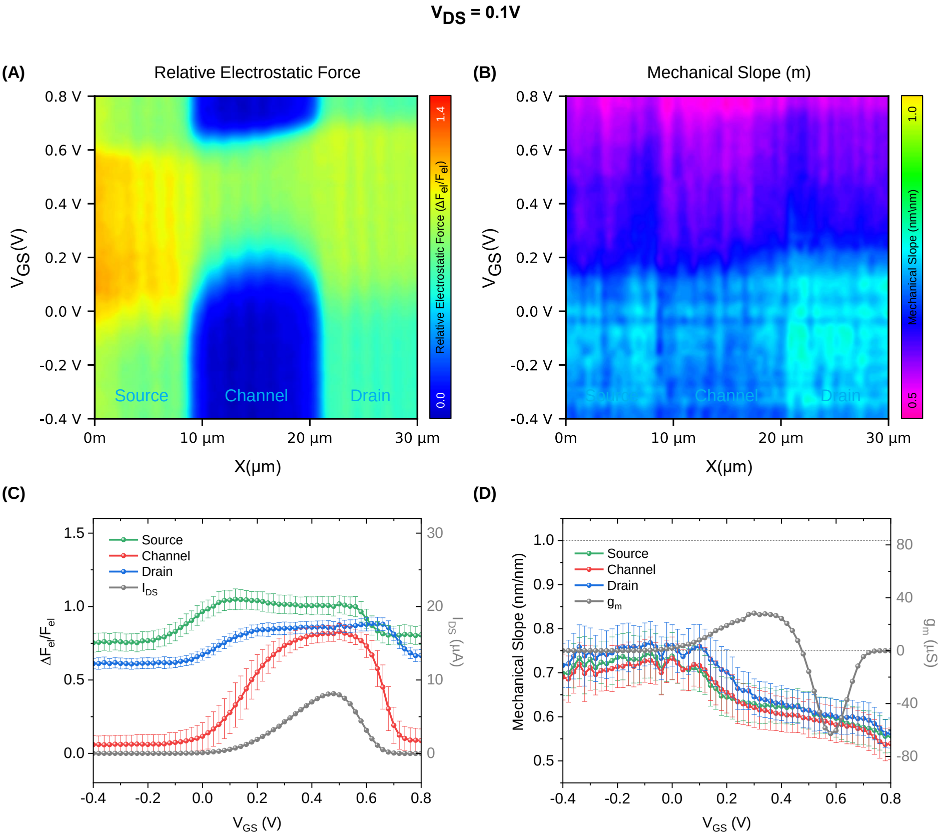

Figure 4.13: Multimodal Measurements at $V_{\mathrm{DS}} = 0.1V$ Same as in Figure 4.11 but for $V_{\mathrm{DS}} = 0.1V$.

we notice that the maximum (positive and negative) transconductance is at the ends of the intermediate plateau.

Figure 4.14 shows the behaviour for $V_{\mathrm{DS}} = 0.2V$. As we see that the asymmetry is increased in the electrostatic force. While in the mechanical maps, the asymmetry persists with increased levels of initial hydration. The hydration seems to be a slow process as the measurements at one drain voltage for the whole gate voltage set takes around 1.5 hours. Also, the behaviour of peak transconductance taking place at the ends of the plateau continues.

Figure 4.15 shows the behaviour for $V_{\mathrm{DS}} = 0.3V$. Here, something interesting happened at peak transconductance. In the electrical map, we see an increase

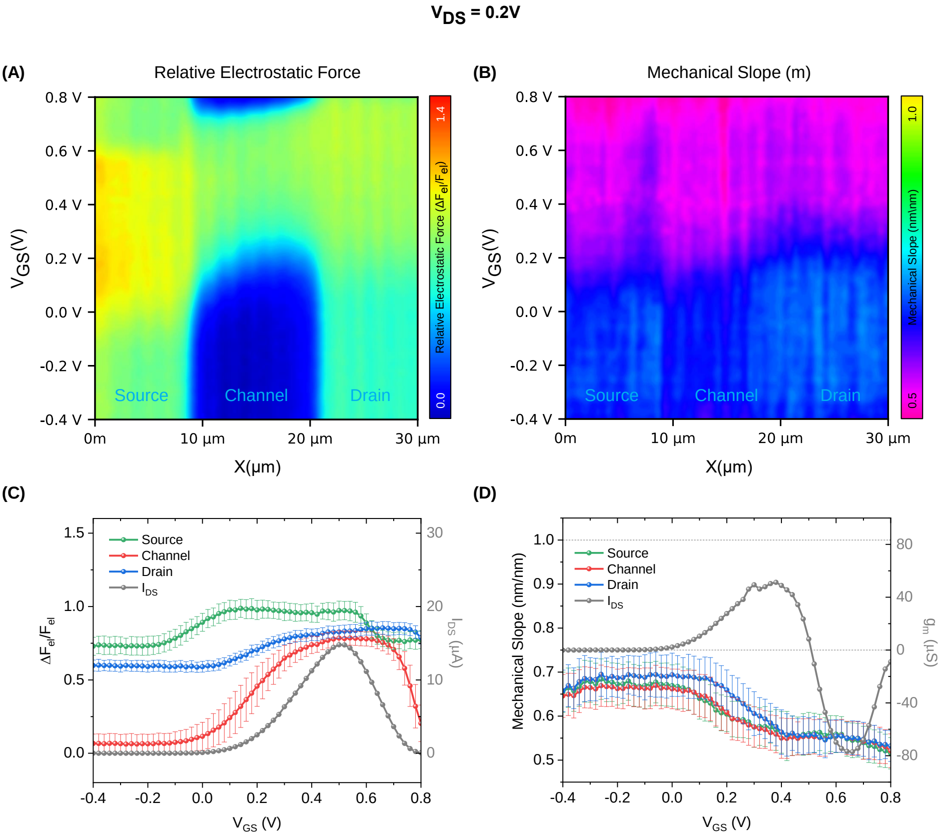

Figure 4.14: Multimodal Measurements at $V_{\mathrm{DS}} = 0.2V$ Same as in Figure 4.11 but for $V_{\mathrm{DS}} = 0.2V$.

in the electrostatic force in the region where it is in-sensitive to conductivity, which implies that the change is due to the change in (read it as bulk or 3D or effective) interfacial capacitance. The mechanical map on the other hand shows a sudden softening of the polymer like a phase change has occurred, giving rise to a dip in the mechanical response. This dip coincides with the steep changes in electrostatic force and both of these coincides with the peak transconductance obtained from the operando recorded drain current measurements. This indicates that at peak transconductance, in this case, a sudden influx of ions in the polymer semiconductor has occurred which increased the capacity of the polymer thereby increasing the electrostatic force. During this influx, the material became quite soft but once the period is over (in terms of gate voltage, not time), the material

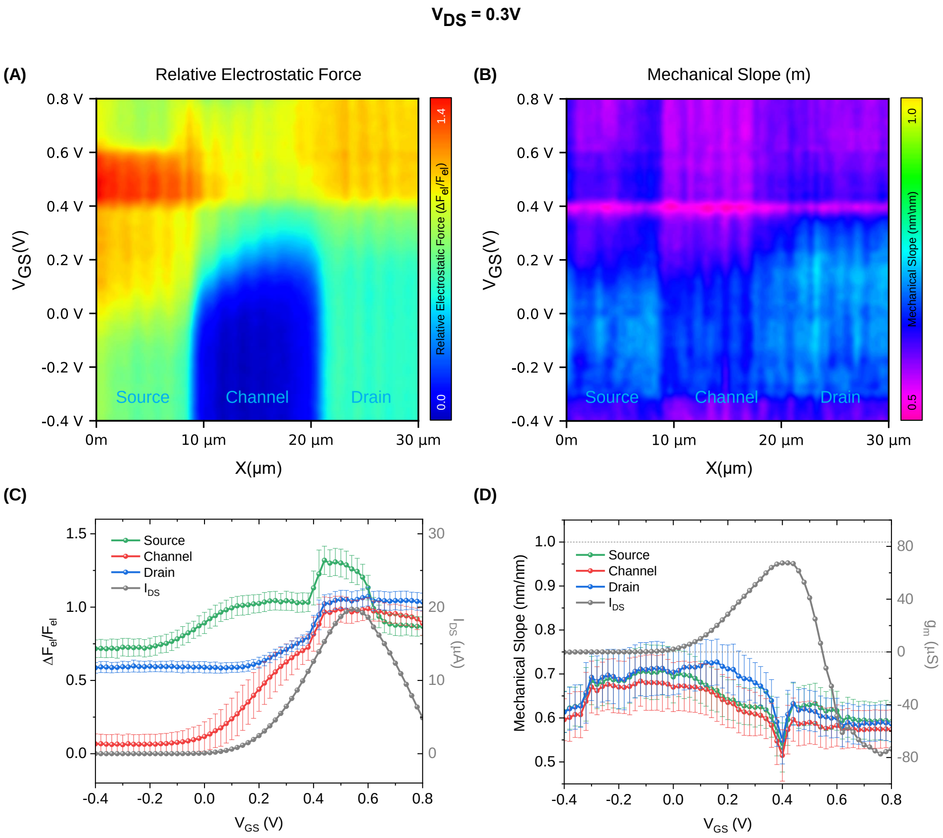

Figure 4.15: Multimodal Measurements at $V_{\mathrm{DS}} = 0.3V$ Same as in Figure 4.11 but for $V_{\mathrm{DS}} = 0.3V$.

stiffness regained the level it started at before the dip. This behaviour is observed in repeat experiments (discussed later) and whenever a dip in mechanical response is seen, it is at the peak transconductance usually.

Figure 4.16 shows the behaviour for $V_{\mathrm{DS}} = 0.4V$, which resembles that of the $V_{\mathrm{DS}} = 03V$, however, here an important thing to point out is that the huge change is due to a disturbance in the experiment which leaked the electrolyte droplet on the transistor and after putting the new electrolyte solution, while some ions remain in the bulk of the polymer, an application of gate voltage might have triggered an increase in the density of ionic concentration in the bulk which lead to a step increase in electrostatic force. Nonetheless, this dataset act as a confirmation of

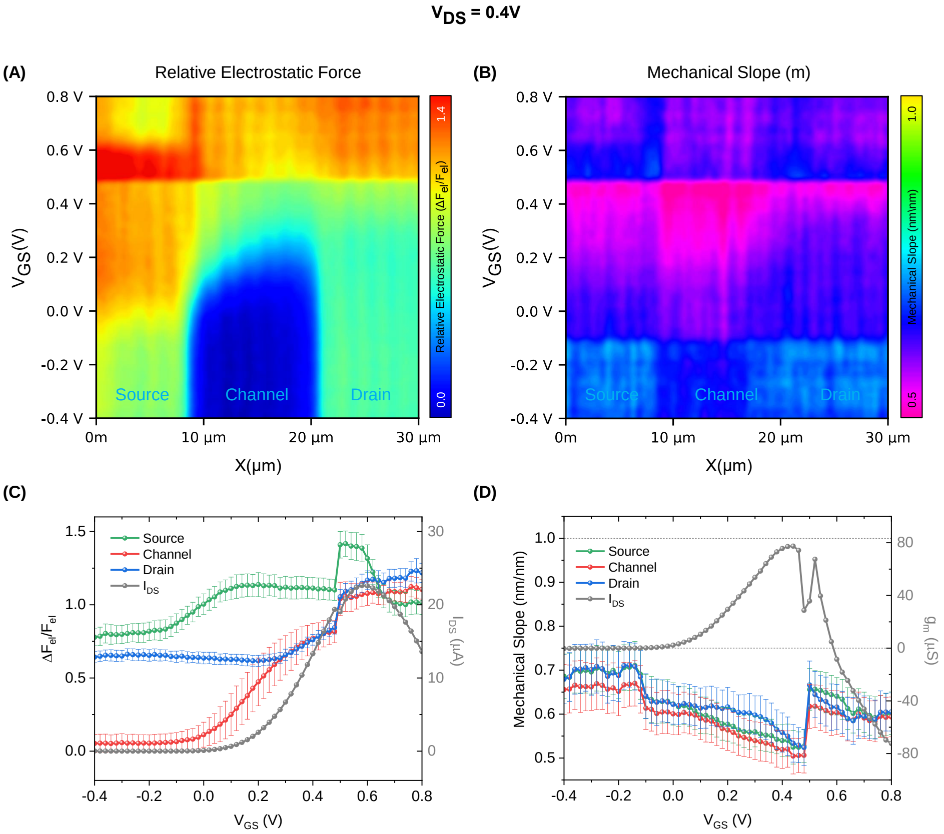

Figure 4.16: Multimodal Measurements at $V_{\mathrm{DS}} = 0.4V$ Same as in Figure 4.11 but for $V_{\mathrm{DS}} = 0.4V$.

an increase in electrostatic force due to an increase in the effective interfacial capacitance.

Finally for this datset, Figure 4.17 shows the behaviour for $V_{\mathrm{DS}} = 0.5V$. Interestingly, if we observe carefully, a dip in the mechanical coinciding with peak transconductance and an increase in electrostatic force is visible.

Figure 4.18 combines the previous dataset for different drain voltages together and separates it for source, channel and drain as the function of gate voltages. The changes in the electrostatic force even in the off-state due to interfacial capacitance change, which are not visible in the channel, qualitatively match the expected behaviour from simulation results referred to earlier in Figure 1.20.

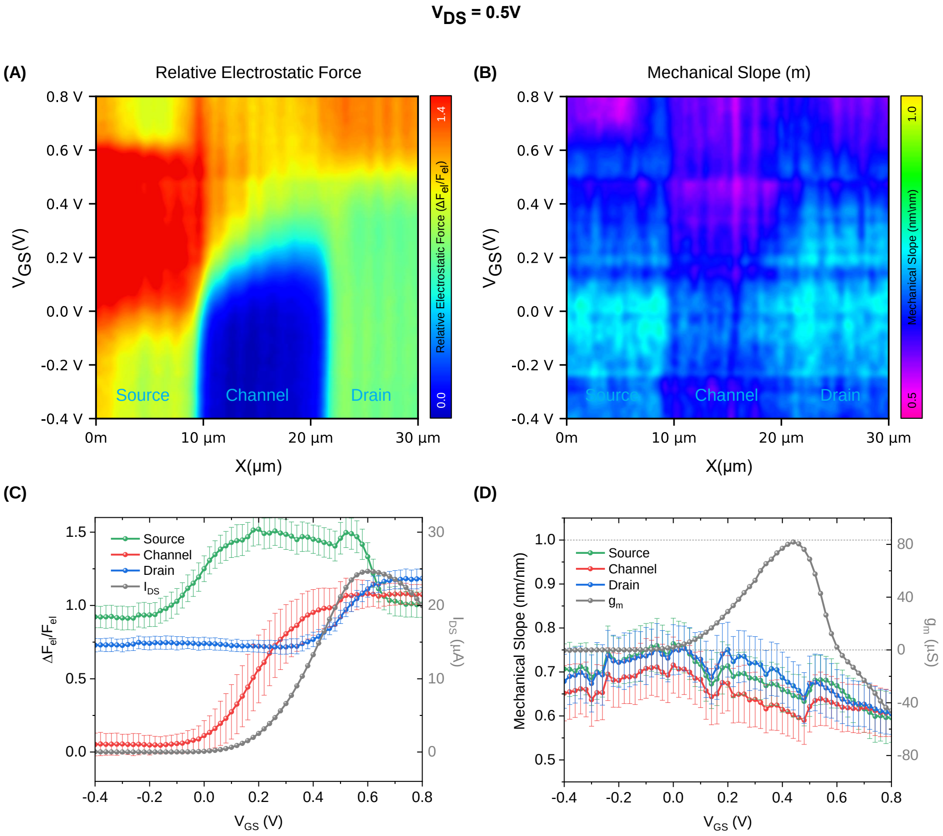

Figure 4.17: Multimodal Measurements at $V_{\mathrm{DS}} = 0.5V$ Same as in Figure 4.11 but for $V_{\mathrm{DS}} = 0.5V$.

We can also quantify the mechanical property in terms of effective sample stiffness in N/m using the measured mechanical slope m, using the Equation 2.5 described earlier in Chapter 2 subsection 2.2.2. Figure 4.19 shows the corresponding mechanical stiffness maps in N/m for all drain voltages. The stiffness of the polymer once hydrated is $< 3N/m$.

As mentioned during the global I-V characterization of OECTs, we also aim to explain the behaviour of drain current onset shifting to higher drain voltages at high gate voltages shown in Figure 4.2B. Figure 4.20 paints this behaviour using the corresponding nanoscale electrostatic force images. As we have seen earlier, in the negative transconductance regime, the electrostatic force is lowered, which implies that the local conductivity is low. For the case of $V_{\mathrm{GS}} = 0.6V$ and

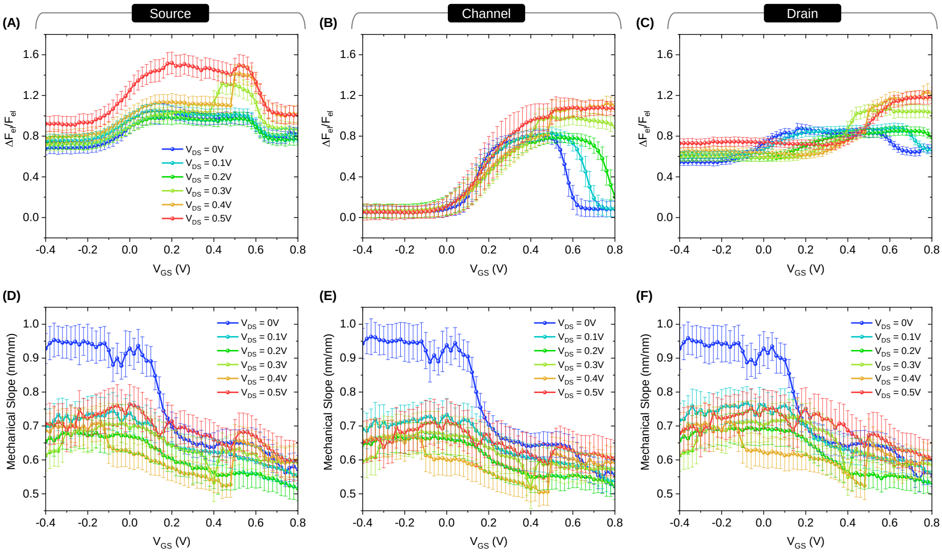

Figure 4.18: Relative electrostatic force trends at (A) Source, (B) Channel and (C) Drain region, along with Mechanical slope (m) trends at (D) Source, (E) Channel and (F) Drain region for all drain voltages probed.

$V_{DS} = 0V$, the channel conductivity is very low and is pinched off completely due to negative transconductance behaviour. As we apply the drain voltage, it increases the local potential which decreases the local effective gate potential thereby taking a portion of the channel out of the negative transconductance regime. As the drain voltage continues to increase, more and more channel region regains conductivity and ultimately bridges the source drain which leads to the drain current. However, if we increase the gate voltage, this condition arrives later and consequently, the drain current onset shifts to high drain voltages as higher local potentials are needed to overcome the increased gate potential. Recently, Xu and Fabiano et al.[6] also explained this behaviour using UV-Vis and Raman microspectroscopy in wide channel length devices ($L \approx 500\mu m$).

In the next section, we provide some supporting data for some of the observations made previously.

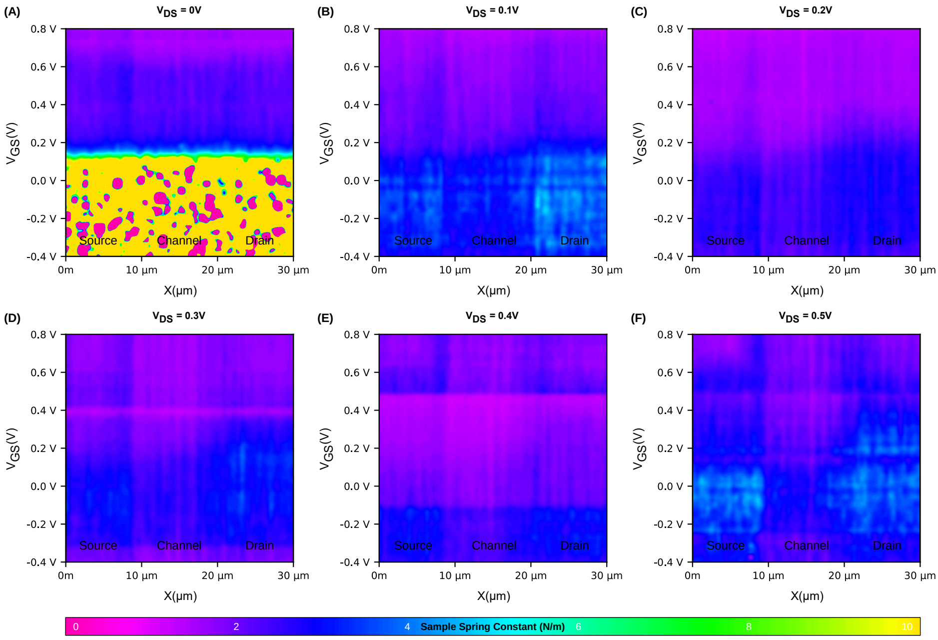

Figure 4.19: Sample spring constant (stiffness) quantified from the measured mechanical slope (m) using the equation Equation 2.5 for V_{DS} equal to (A) 0V, (B) 0.1V, (C) 0.2V, (D) 0.3V, (E) 0.4V, and (F) 0.5V.

Supporting Data

In this section, we explore the coincidence of the sudden phase change with the maximum transconductance peak.

We consider an experiment done in pristine conditions starting at $V_{\mathrm{DS}} = 0V$ as shown in Figure 4.21(A-B) and thereafter at $V_{\mathrm{DS}} = 0.1V$ shown in Figure 4.21(C-D). In the case of $V_{\mathrm{DS}} = 0V$, we do see a sudden phase change in mechanical which again coincides with the peak transconductance. In the case of $V_{\mathrm{DS}} = 0.1V$, we also see a sudden phase change with an increase in the electrostatic force. It seems that when this sudden phase change happens it leads to an increase in electrostatic force. What if we do the measurements in pristine condition at a fixed non-zero drain voltage and sweep the gate voltage forward and backwards?

Figure 4.22 shows the measurements done in the pristine conditions directly at $V_{\mathrm{DS}} = 0.3V$ while sweeping the gate voltage forward from $-0.4V$ to $0.8V$ and then

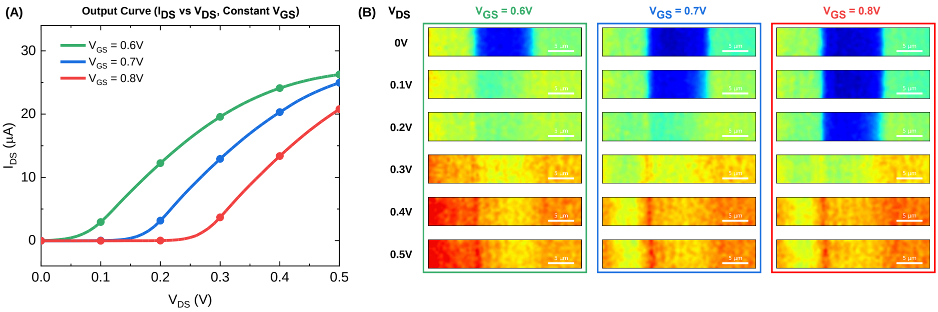

Figure 4.20: The drain current onset in (A) is explained based on the corresponding nanoscale electrical images at the highlighted data points. The effective gate voltage once surpasses the negative transconductance region, leads to a locally off-state. As the applied gate voltage in this regime increases, more region is locally off, especially at the source where the effective gate voltage is the largest.

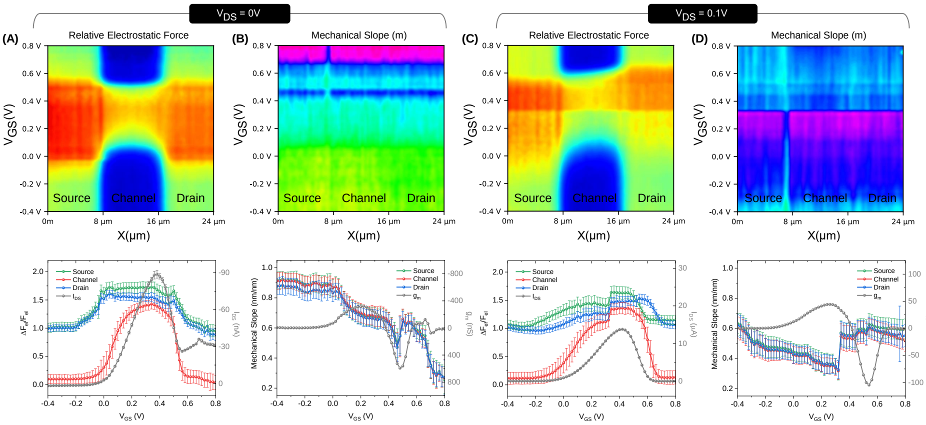

Figure 4.21: [Supporting Data] Measurement performed on a pristine sample with V_{GS} sweeping from $-0.4V$ to $0.8V$ first at (A) $V_{\mathrm{DS}} = 0V$ and then thereafter at (B) $V_{\mathrm{DS}} = 0.1V$. Relative electrostatic force and mechanical slope (m) reconstructed spectrums as in other cases are plotted along with trends at the source, channel and drain region. The reconstructed transfer curve and its derivative (transconductance) are also shown alongside.

backwards from $0.78V$ to $-0.4V$. In the forward sweep, we do see the asymmetry in electrical and mechanical maps, with peak transconductance at the start of the plateau. Whereas in the backward sweep, we see a sudden phase change again and it more or less coincides with the peak transconductance. Also, we notice that the electrostatic force has increased after passing this sudden phase change.

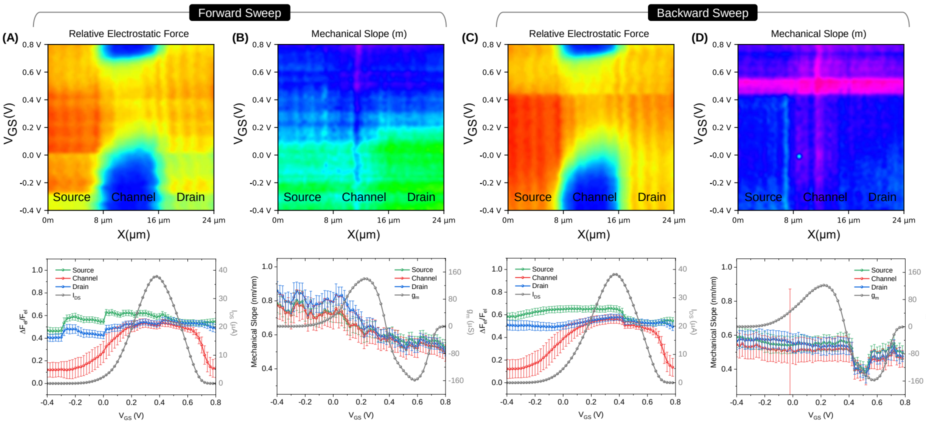

Figure 4.22: [Supporting Data] Measurement performed on a pristine sample direct at $V_{\mathrm{DS}} = 0.3V$ and V_{GS} sweeping (A-B) from $-0.4V$ to $0.8V$ and then backwards (C-D) from $0.78V$ to $-0.4V$. Relative electrostatic force and mechanical slope (m) reconstructed spectrums as in other cases are plotted along with trends at the source, channel and drain region. The reconstructed transfer curve and its derivative (transconductance) are also shown alongside.

This supports that whenever this phase change happens, it leads to an increase in effective interfacial stern capacitance which probably is due to the sudden influx of ions into the polymer.

Figure 4.23 shows the recorded drain current in the forward and backward sweep, where we see that the initial forward curve is steeper than the backward leading to hysteresis, which is also the case for electrostatic force corresponding to the channel region. The steepness in the initial cycle is also seen in Figure 4.18B.

4.3. Open Questions

The measurements done on OECTs are indeed very rich in information and the system itself is very complex. The measured electrical and mechanical behaviour is coupled in these devices which mirrors the electronic-ionic coupling, providing valuable insights into the operating mechanism of these devices. However, there are still some open questions which pertain to the observations made in this chapter whose fundamental basis is yet to be understood, specifically:

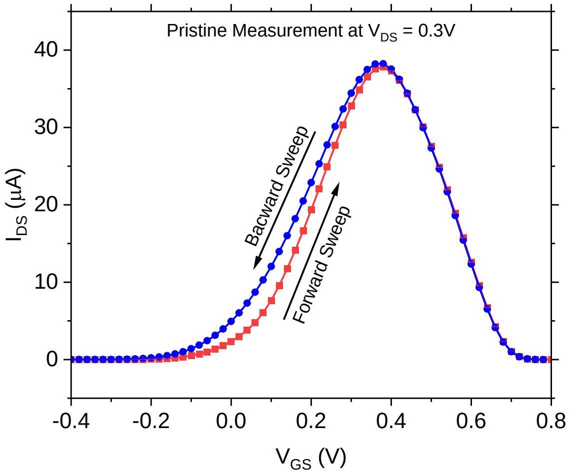

Figure 4.23: Reconstructed forward and backward transfer curves corresponding to data shown in Figure 4.22 are plotted together to highlight the difference.

1. Why the sudden mechanical phase change coincides with the maximum (positive or negative) peak transconductance?
2. What controls this phase change?
3. How does this phase change depend on the doping history of the organic polymer? Is there a memory effect?
4. Why there are sometimes big topographic swelling and what controls them? (see below for measurements.)

The above questions are very fundamental in nature and require probing in numerous other scenarios to pinpoint the origin of the observed behaviours. As shown in this thesis, in-liquid SDM can be a very important tool to aid in exploring the answer to these questions, especially the automated data acquisition and analysis approach can substantially speed up this discovery process.

Regarding the last question posed, there are sometimes big topographic swellings observed in these devices, as shown in Figure 4.24, whose origin is not yet clear. Are they just highly hydrated or are they a byproduct of some electrochemical side reactions? These huge topographic bubbles don't seem to affect the device properties as they don't appear to have impacted the rigidity of the organic polymer. It requires quite a lot of force to rupture one such topographic bubble and once ruptured, they expose the substrate like puncturing a rubber-type elastic thin film, see Figure 4.25.

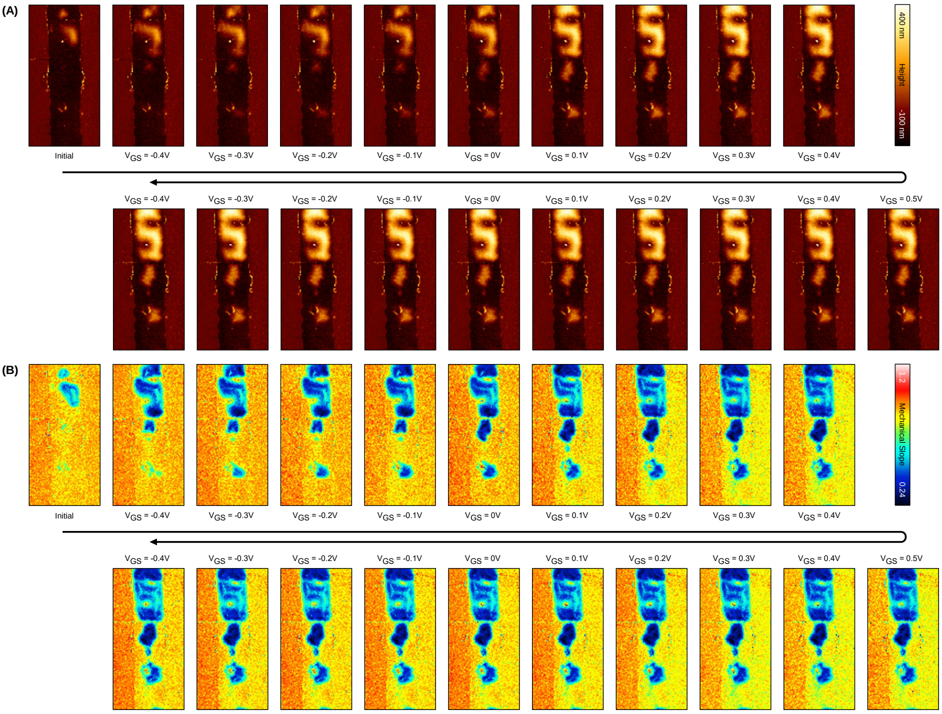

Figure 4.24: (A) Observed big topographic swelling (B) Corresponding mechanical maps. Measurements are done in Milli-Q and at a drain voltage of $V_{\mathrm{DS}} = 0.5V$.

4.4. Conclusion

We observed how the nanoscale electrical and mechanical properties of the operating OECT relate to the device level I-V characteristics in different operating regimes. The spatial variability in the nanoscale electrical and mechanical properties as the function of drain and gate voltages is highlighted. The negative transconductance regime is visualized and correlated with the characteristic features observed in the device I-V characteristics such as the delayed drain current onset to high drain voltages at high doping levels of the semiconductor. A peculiar phase change is observed that coincides with the maximum (positive or negative)

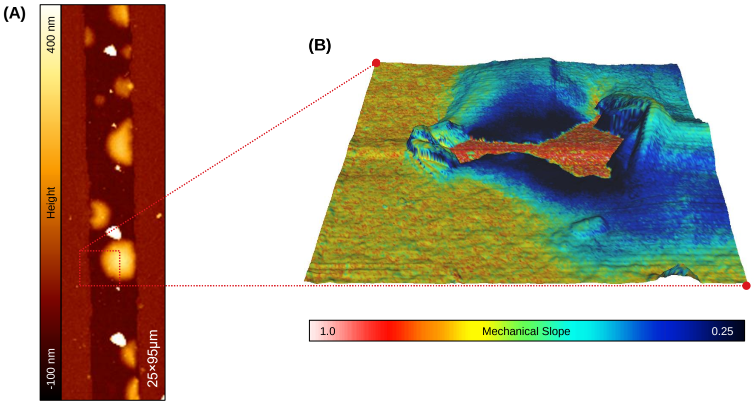

Figure 4.25: (A) Topography of a transistor showing big topographic bubbles (B) Mechanical slope superimposed on the topographic image of a ruptured bubble by the AFM tip, notice the wrinkles on the edges of the ruptured area indicating elastic nature.

transconductance points and seems to be related to a sudden influx of ions into the polymer increasing its effective interfacial capacitance and thus the measured electrostatic force.

A set of open questions are highlighted whose further exploration can be substantially aided using the implemented automated in-liquid SDM. The present approach represents significant advancements in experimental methods that provide rich multiscale and multimodal information about the operating electrolyte-gated devices.

4.5. References

1. J. Rivnay, S. Inal, A. Salleo, R. M. Owens, M. Berggren, and G. G. Malliaras, “Organic electrochemical transistors,” *Nature Reviews Materials*, vol. 3, p. 17086, 2018. doi:10.1038/natrevmats.2017.86
2. B. D. Paulsen, K. Tybrandt, E. Stavrinidou, and J. Rivnay, “Organic mixed ionic–electronic conductors,” *Nature Materials*, vol. 19, pp. 13–26, 2020. doi:10.1038/s41563-019-0435-z
3. R. Wu, M. Matta, B. D. Paulsen, and J. Rivnay, “Operando characterization of organic mixed ionic/electronic conducting materials,” *Chemical Reviews*, vol. 122, pp. 4493–4551, 2022. doi:10.1021/acs.chemrev.1c00597

4. S. Jiang, Q. Dai, J. Guo, and Y. Li, “In-situ/operando characterization techniques for organic semiconductors and devices,” *Journal of Semiconductors*, vol. 43, p. 041101, 2022. doi:10.1088/1674-4926/43/4/041101

5. P. C. Harikesh, C.-Y. Yang, H.-Y. Wu, et al., “Ion-tunable antiambipolarity in mixed ion–electron conducting polymers enables biorealistic organic electrochemical neurons,” *Nature Materials*, vol. 22, pp. 242–248, 2023. doi:10.1038/s41563-022-01450-8

6. K. Xu, T.-P. Ruoko, M. Shokrani, et al., “On the origin of seebeck coefficient inversion in highly doped conducting polymers,” *Advanced Functional Materials*, vol. 32, p. 2112276, 2022. doi:10.1002/adfm.202112276

7. S. E. Chen, R. Giridharagopal, and D. S. Ginger, “Artificial neuron transmits chemical signals,” *Nature Materials*, vol. 22, pp. 416–418, 2023. doi:10.1038/s41563-023-01509-0

8. G. C. Faria, D. T. Duong, and A. Salleo, “On the transient response of organic electrochemical transistors,” *Organic Electronics*, vol. 45, pp. 215–221, 2017. doi:https://doi.org/10.1016/j.orgel.2017.03.021

9. J. Guo, L. Q. Flagg, D. K. Tran, et al., “Hydration of a side-chain-free n-type semiconducting ladder polymer driven by electrochemical doping,” *Journal of the American Chemical Society*, vol. 145, pp. 1866–1876, 2023. doi:10.1021/jacs.2c11468

PART IV

FINAL REMARKS

Chapter 5

Discussion

This thesis presented significant advances towards nanoscale multimodal characterization of operating electrolyte-gated transistors (EGTs), in particular, Electrolyte-Gated Organic Field-Effect Transistors (EGOFETs) and Organic Electrochemical Transistors (OECTs), which are fundamental building blocks for various potential applications, such as biosensing[1–6], bio-interfacing[7,8], toxicology[9,10], wearable and on-skin health monitoring[11–13], neuromorphic computing[14–20], electrochromic devices[21,22], integrated circuits[23–25] and many more.

The wide range of applications addressed by these foundational architectures demands a detailed, comprehensive understanding of their operating mechanism so they can be tailored for efficient and reliable use in a specific application. A rudimentary understanding might suffice for developing proof-of-concept devices through trial-and-error approaches without relying on understanding the detailed operating mechanism. However, once the technologies and devices become complex, a rudimentary understanding is not sufficient to make further progress, especially on the stability and performance front of these devices, which still needs to be improved quite significantly to enable reliable and efficient working technologies in real-world scenarios. Pertinently, many recent reviews[26–28] highlighted shifting the focus towards developing characterization tools that can allow one to see precisely what is happening in the device through a multimodal perspective, which includes information on morphology, electrical and mechanical properties, among others.

Revealing the operating mechanism not only makes us more confident in our assertions but also enables directing our resources to the right question to ask and answer once the mechanism and its bottlenecks are visible, which itself is the basis of scientific discourse.

To address the objective of revealing the operating mechanism of EGTs, in this thesis, we further developed an earlier implementation of in-Liquid SDM on EGOFETs by Kyndiah et al.[29], where we not only added automated data acquisition and analysis capabilities with mechanical probing but also focused on the signal interpretation itself as EGTs represents a complex dynamic system, and a lot of prior assumption made might not be valid anymore. Specifically, on the instrumentation side we identified high-frequency artefacts that lead to changes in the AC tip voltage, not only when the conductivity of the semiconducting material changes as a function of gate voltage but also when the SDM probe traverses the source-channel-drain region. Thanks to the automation that we designed to grab all the external parameters during experiments, it enabled us to find the impact of this artefact and also propose approaches to make corrections. Previous approaches addressed this artefact through the use of a renormalization factor as described in subsection 2.1.2. However, such an approach is neither practical nor sufficient, especially when the conductivity of the system changes. However, it is important to note that the usual quantitative analysis using the finite element simulation is slightly immune to this artefact as other unimportant fitting parameters absorb the variation. Nonetheless, it is not possible at present to do simulations representing the actual system without making simplifying assumptions. We need an easy and efficient approach.

To our surprise, the correction turns out to be very simple: just taking the relative variation with respect to a reference tip-sample distance in the measured raw electrical signal (refer subsection 2.1.2) instead of following the usual calibration procedure[30]. Considering relative variations of the measured electric forces presented another advantage, that the requirements of knowing various calibration factors (Equation 2.4) are not required anymore as they cancel out when taking relative changes (Equation 2.3). Despite, this result being apparently simple it has huge associated advantages with significant implications on a typical workflow via simplifying the whole process, especially when very large data sets are to be analyzed as we did in the present thesis.

From the analysis of the relative electric force changes, it could effectively be identified a trend between the local electric force values and the expected local potential. The underlying relation has been that the measured electrostatic force depends on the local conductivity, and the local conductivity depends on the local effective gate potential, which is directly affected by the local potential. Based on that property, we developed an approach introduced in section 2.3 that enabled mapping the local electric potential quantitatively in a working EGT directly from the measured raw signal (relative electrostatic forces). The critical aspect is that this is achieved without relying on finite element simulations. This result is more significant as it circumvented the fundamental and technical limitations of the conventional KPFM technique in aqueous electrolytes[31], which have been commonly used in the air for mapping electrical potentials in OFETs[32]. The quantitative electric potential mapping enabled the quantification of various crucial charge transport parameters such as contact access resistance, inter-and intra-domain charge transport, and anisotropy, which weren't accessible earlier at the nanoscale in EGTs.

We used these developments first on an EGOFET based on a blend of organic semiconducting material diF-TES-ADT and the insulating polymer polystyrene (PS) in Chapter 3, where we mapped the operation across all operating regimes of the device. We found that the contact resistance and grain boundaries have heavily limited the charge transport, whereas the intra-domain charge transport is quite efficient. It indicates that we need to focus on improving the contact and grain boundary characteristics instead of intrinsic intra-domain charge transport, as it is already quite efficient. The focus on improving performance has mainly been towards improving the charge carrier mobility[33] in general, whereas in the studied system, the focus needs to be shifted to contact and grain boundary interface engineering. This insight certainly comes through direct probing of the operating mechanism, which was not possible earlier and has been the core objective of this thesis.

In Chapter 4, we move to a more complex device, an OECT based on ladder-type polymer BBL, where complex physical and chemical changes occur due to ion penetration into the bulk of the semiconductor, leading to bulk ionic-electronic coupling. Instead, in EGOFETs, the ionic-electronic coupling is limited to the semiconductor/electrolyte interface, and no penetration of ions happens into the semiconductor. In OECTs, we monitored the motion of the ions into the semiconductor indirectly through the electrical signal and directly through the mechanical indentation during a typical force-volume acquisition mode of in-liquid SDM (refer subsection 2.2.2). The initial injection of ions generally accompanies the swelling of the organic semiconductor, which leads to changes in its mechanical properties, usually making it softer, which is probed during an indentation part of the approach curve. The mechanical properties of the organic mixed-ionic electronic conductors in operando had been investigated previously using Electrochemical Strain Microscopy (discussed in subsection 1.6.1) and recently using Biomodal Atomic Force Microscopy (discussed in subsection 1.6.2). However, the advantage of our method is that we simultaneously probed also the local electrical properties, which gives our measurements a multimodal character and allows for a unified understanding of the material response to applied electric fields.

We observed that OECTs show rich mechanical behaviour, which is absent in the EGOFETs, and consequently, more complex dynamics are present. We noticed two behaviours at maximum (positive or negative) transconductance points. In a semiconductor which is still undergoing hydration, the peak transconductance appears at a transition point where the mechanical changes are stabilizing and reaching a plateau or vice versa. In a pre-hydrated film, sometimes, the peak transconductance appears in conjunction with a sudden decrease in mechanical stiffness and an increase in the capacity of the material. It indicates that an influx of ions happens into the polymer at peak transconductance, and the material becomes soft during this influx; after this influx, the capacity of the material (the fixed effective interfacial capacitance) has increased. In EGOFETs, during the stable voltage operating window, no mechanical changes happen, but it seems that once the voltage outside the stability window is applied, thereby forcing the ions into the material, such peaks are also observed at the maximum transconductance point (see Appendix C Figure C.2B), however, the material is not stable for ion penetration and consequently degrades quickly. These observations point towards a universal phenomenon that is linked with the ion penetration in such materials at these characteristic operating points. Such behaviour warrants closer examination to reveal the exact nature of this phenomenon, which comes into the future prospects beyond this thesis. Besides, using the nanoscale electrical mapping of OECT, we also explained the shift of drain current onset to higher drain voltages at high doping conditions in a negative transconductance regime, which offers insights into how this mechanism plays out and how it is linked with the device response. Finally, we highlighted some open questions (section 4.3) that will become a topic of research beyond this thesis.

Besides all the advantages mentioned previously, it is also important to point out the limitations of the current technique so that future efforts can be directed towards a better version of in-Liquid SDM implementation on EGTs. The main limitation has been that the measurements are relatively slow and take a long time. However, automation has improved the data throughput, but the imaging speed needs to be a few seconds instead of tens of seconds currently. The system under study needs to be stable, so the degradation and bias stress effects can be neglected or avoided. Nonetheless, in the case of an unstable or degrading system, the technique can still be a valuable tool to pinpoint the origin of degradation, such as the measurements shown in Appendix C.

To summarise this discussion, the developments and results presented provide a comprehensive understanding of electrolyte-gated transistors through a multimodal perspective in operating conditions, and the current thesis lays the foundation for further advanced studies and future improvements in experimental implementation.

5.1. References

1. L. Kergoat, B. Piro, M. Berggren, M.-C. Pham, A. Yassar, and G. Horowitz, “Dna detection with a water-gated organic field-effect transistor,” *Organic Electronics*, vol. 13, pp. 1–6, 2012. doi:https://doi.org/10.1016/j.orgel.2011.09.025

2. E. Macchia, K. Manoli, C. Di Franco, et al., “Organic field-effect transistor platform for label-free, single-molecule detection of genomic biomarkers,” *ACS Sensors*, vol. 5, pp. 1822–1830, 2020. doi:10.1021/acssensors.0c00694

3. S. Ricci, S. Casalini, V. Parkula, et al., “Label-free immunodetection of α-synuclein by using a microfluidics coplanar electrolyte-gated organic field-effect transistor,” *Biosensors and Bioelectronics*, vol. 167, p. 112433, 2020. doi:https://doi.org/10.1016/j.bios.2020.112433

4. M. Selvaraj, P. Greco, M. Sensi, et al., “Label free detection of mirna-21 with electrolyte gated organic field effect transistors (egofets),” *Biosensors and Bioelectronics*, vol. 182, p. 113144, 2021. doi:https://doi.org/10.1016/j.bios.2021.113144

5. R. Hasler, C. Reiner-Rozman, S. Fossati, et al., “Field-effect transistor with a plasmonic fiber optic gate electrode as a multivariable biosensor device,” *ACS Sensors*, vol. 7, pp. 504–512, 2022. doi:10.1021/acssensors.1c02313

6. K. Solodka, M. Berto, D. Ferraro, et al., "Detection of neurofilament light chain with label-free electrolyte-gated organic field-effect transistors," *Advanced Materials Interfaces*, vol. 9, p. 2102341, 2022. doi:https://doi.org/10.1002/admi.202102341

7. K. Lieberth, P. Romele, F. Torricelli, et al., "Current-driven organic electrochemical transistors for monitoring cell layer integrity with enhanced sensitivity," *Advanced Healthcare Materials*, vol. 10, p. 2100845, 2021. doi:https://doi.org/10.1002/adhm.202100845

8. C. Pitsalidis, A.-M. Pappa, A. J. Boys, et al., "Organic bioelectronics for in vitro systems," *Chemical Reviews*, vol. 122, pp. 4700–4790, 2022. doi:10.1021/acs.chemrev.1c00539

9. A. Kyndiah, F. Leonardi, C. Tarantino, et al., "Bioelectronic recordings of cardiomyocytes with accumulation mode electrolyte gated organic field effect transistors," *Biosensors and Bioelectronics*, vol. 150, p. 111844, 2020. doi:https://doi.org/10.1016/j.bios.2019.111844

10. Y. Zhang, Q. Zeng, Y. Shen, L. Yang, and F. Yu, "Electrochemical stability investigations and drug toxicity tests of electrolyte-gated organic field-effect transistors," *ACS Applied Materials & Interfaces*, vol. 12, pp. 56 216–56 221, 2020. doi:10.1021/acsami.0c15024

11. H. Lee, S. Lee, W. Lee, T. Yokota, K. Fukuda, and T. Someya, "Ultrathin organic electrochemical transistor with nonvolatile and thin gel electrolyte for long-term electrophysiological monitoring," *Advanced Functional Materials*, vol. 29, p. 1906982, 2019. doi:https://doi.org/10.1002/adfm.201906982

12. M. Galliani, L. M. Ferrari, and E. Ismailova, "Interdigitated organic sensor in multimodal facemask's barrier integrity and wearer's respiration monitoring," *Biosensors*, vol. 12, 2022. doi:10.3390/bios12050305

13. A. Yang, J. Song, H. Liu, Z. Zhao, L. Li, and F. Yan, "Wearable organic electrochemical transistor array for skin-surface electrocardiogram mapping above a human heart," *Advanced Functional Materials*, vol. 33, p. 2215037, 2023. doi:https://doi.org/10.1002/adfm.202215037

14. Q. Lai, L. Zhang, Z. Li, W. F. Stickle, R. S. Williams, and Y. Chen, "Ionic/electronic hybrid materials integrated in a synaptic transistor with signal

processing and learning functions," *Advanced Materials*, vol. 22, pp. 2448–2453, 2010. doi:https://doi.org/10.1002/adma.201000282

15. P. Gkoupidenis, N. Schaefer, B. Garlan, and G. G. Malliaras, "Neuromorphic functions in pedot:pss organic electrochemical transistors," *Advanced Materials*, vol. 27, pp. 7176–7180, 2015. doi:https://doi.org/10.1002/adma.201503674

16. P. Gkoupidenis, D. A. Koutsouras, and G. G. Malliaras, "Neuromorphic device architectures with global connectivity through electrolyte gating," *Nature Communications*, vol. 8, p. 15448, 2017. doi:10.1038/ncomms15448

17. Y. van de Burgt, E. Lubberman, E. J. Fuller, et al., "A non-volatile organic electrochemical device as a low-voltage artificial synapse for neuromorphic computing," *Nature Materials*, vol. 16, pp. 414–418, 2017. doi:10.1038/nmat4856

18. J. Y. Gerasimov, R. Gabrielsson, R. Forchheimer, et al., "An evolvable organic electrochemical transistor for neuromorphic applications," *Advanced Science*, vol. 6, p. 1801339, 2019. doi:https://doi.org/10.1002/advs.201801339

19. S. T. Keene, C. Lubrano, S. Kazemzadeh, et al., "A biohybrid synapse with neurotransmitter-mediated plasticity," *Nature Materials*, vol. 19, pp. 969–973, 2020. doi:10.1038/s41563-020-0703-y

20. S. Wang, X. Chen, C. Zhao, et al., "An organic electrochemical transistor for multi-modal sensing, memory and processing," *Nature Electronics*, vol. 6, pp. 281–291, 2023. doi:10.1038/s41928-023-00950-y

21. P. Andersson, R. Forchheimer, P. Tehrani, and M. Berggren, "Printable all-organic electrochromic active-matrix displays," *Advanced Functional Materials*, vol. 17, pp. 3074–3082, 2007. doi:https://doi.org/10.1002/adfm.200601241

22. E. Zeglio, M. Vagin, C. Musumeci, et al., "Conjugated polyelectrolyte blends for electrochromic and electrochemical transistor devices," *Chemistry of Materials*, vol. 27, pp. 6385–6393, 2015. doi:10.1021/acs.chemmater.5b02501

23. R. Porrazzo, A. Luzio, S. Bellani, et al., "Water-gated n-type organic field-effect transistors for complementary integrated circuits operating in an aque-

ous environment," *ACS Omega*, vol. 2, pp. 1–10, 2017. doi:10.1021/acsomega.6b00256

24. H. Sun, M. Vagin, S. Wang, et al., "Complementary logic circuits based on high-performance n-type organic electrochemical transistors," *Advanced Materials*, vol. 30, p. 1704916, 2018. doi:https://doi.org/10.1002/adma.201704916

25. P. Andersson Ersman, R. Lassnig, J. Strandberg, et al., "All-printed large-scale integrated circuits based on organic electrochemical transistors," *Nature Communications*, vol. 10, p. 5053, 2019. doi:10.1038/s41467-019-13079-4

26. B. D. Paulsen, K. Tybrandt, E. Stavrinidou, and J. Rivnay, "Organic mixed ionic–electronic conductors," *Nature Materials*, vol. 19, pp. 13–26, 2020. doi:10.1038/s41563-019-0435-z

27. R. Wu, M. Matta, B. D. Paulsen, and J. Rivnay, "Operando characterization of organic mixed ionic/electronic conducting materials," *Chemical Reviews*, vol. 122, pp. 4493–4551, 2022. doi:10.1021/acs.chemrev.1c00597

28. S. Jiang, Q. Dai, J. Guo, and Y. Li, "In-situ/operando characterization techniques for organic semiconductors and devices," *Journal of Semiconductors*, vol. 43, p. 041101, 2022. doi:10.1088/1674-4926/43/4/041101

29. A. Kyndiah, M. Checa, F. Leonardi, et al., "Nanoscale mapping of the conductivity and interfacial capacitance of an electrolyte-gated organic field-effect transistor under operation," *Advanced Functional Materials*, vol. 31, p. 2008032, 2021. doi:10.1002/adfm.202008032

30. R. Millan-Solsona, M. Checa, L. Fumagalli, and G. Gomila, "Mapping the capacitance of self-assembled monolayers at metal/electrolyte interfaces at the nanoscale by in-liquid scanning dielectric microscopy," *Nanoscale*, vol. 12, pp. 20 658–20 668, 2020. doi:10.1039/D0NR05723A

31. L. Collins, S. Jesse, J. I. Kilpatrick, et al., "Probing charge screening dynamics and electrochemical processes at the solid–liquid interface with electrochemical force microscopy," *Nature Communications*, vol. 5, p. 3871, 2014. doi:10.1038/ncomms4871

32. V. Palermo, M. Palma, and P. Samorì, “Electronic characterization of organic thin films by kelvin probe force microscopy,” *Advanced Materials*, vol. 18, pp. 145–164, 2006. doi:https://doi.org/10.1002/adma.200501394

33. G. Schweicher, G. Garbay, R. Jouclas, F. Vibert, F. Devaux, and Y. H. Geerts, “Molecular semiconductors for logic operations: Dead-end or bright future?” *Advanced Materials*, vol. 32, p. 1905909, 2020. doi:10.1002/adma.201905909

Chapter 6

Conclusion and Future Perspectives

Nanoscale multimodal characterization of operating electrolyte-gated transistors (EGTs) is essential to enable investigation of the fundamental operating mechanism governing the device response. Revealing the operating mechanism facilitates asking the right scientific questions and points toward potential solutions. The thesis favors following a rational approach for developing structure-property-function relationships towards targeted optimization of devices in contrast to commonly used trial-and-error approaches.

In this thesis, we presented significant advancements and improvements made in the earlier (subsection 1.6.4) in-liquid Scanning Dielectric Microscopy (SDM) implementation on EGTs. We standardized and automated the measurement protocol and data analysis. We included the mechanical properties into the analysis. We identified high-frequency artefacts plaguing the dataset owing to changes in the AC tip-sample potential during imaging. An easy and robust approach is introduced to take care of this artefact by simply considering the relative electrostatic force variations with respect to a reference tip-sample distance instead of absolute values as usually considered (subsection 2.1.2). This approach has significant appeal as there is no need for the usual calibration procedure (Equation 2.4) or knowing various calibration factors such as cantilever spring constant (k), AFM optical system deflection sensitivity (s), lock-in amplifier gain (G), applied AC potential amplitude (v_{ac}), and the renormalization factor (α). Also, we introduced a new potential mapping mode based on in-liquid SDM that gives the quantitative local electric potential of operating semiconducting devices directly from raw experimental data (relative electrostatic force) without invoking finite element simulations, providing access to crucial charge transport parameters such as contact access resistance, inter-and intra-domain charge transport and anisotropy, which weren't accessible earlier at the nanoscale in EGTs. To give multimodal character to the measurements, we utilized the force-volume data acquisition mode of in-liquid SDM to extract mechanical properties during the indentation segment of the approach curves in contact, whereas the non-contact part gave access to the usual local electrical properties. It allowed us to simultaneously investigate the material response through electrical and mechanical modalities for unified understanding.

We first focused on p-type EGOFETs based on a blend of organic semiconducting material diF-TES-ADT and the insulating polymer polystyrene (PS), where we investigated the evolution of local electrical properties in various operating regimes, namely sub-threshold, linear and saturation. The pinch-off characteristics are found to be dependent on the microstructural signature of the organic semiconductor, which controls the extension of the pinch-off into the channel region. The evolution of nanoscale electrical properties as a function of gate voltage is investigated under different structural features of the organic semiconductors, thereby identifying the traits that lead to inferior charge transport characteristics. The developed potential mapping mode quantified the impact of thin-film polycrystalline nature on the charge transport, where we found that the intrinsic conductivity of an individual domain as high as $\approx 40S/m$ was diminished to an effective conductivity of $\approx 14S/m$ in the polycrystalline film due to grain boundaries under applied biases. The contact access resistances further decreased it to an effective device conductivity of $\approx 4S/m$. This result suggests that the research efforts need to focus on removing these charge transport bottlenecks by contact and grain boundary interface engineering to enable reaching characteristics close to that of individual crystalline grains.

After that, we focused on n-type OECTs based on ladder-type polymer BBL, where we investigated the coupled electrical and mechanical behaviour across different operating regimes by utilizing the multimodal character of our in-liquid SDM implementation. The spatial variability in the mechanical stiffness in response to applied drain potentials was correlated with the corresponding local electrical properties. A peculiar sudden phase change in mechanical response was observed that coincides with the maximum (positive or negative) transconductance points of the device, where an influx of ions into the polymer affirmed with a simultaneous increase of the effective interfacial capacitance happens. The electrical mapping was also used to explain the drain current onset to higher drain voltages at high gate voltages in the negative transconductance regimes.

Overall, this thesis has resulted in a significant contribution to a detailed understanding of the operating mechanism in EGTs through a multimodal perspective. This thesis's current developments and results can be utilized to understand transduction mechanisms in more complex architectures, devices and materials.

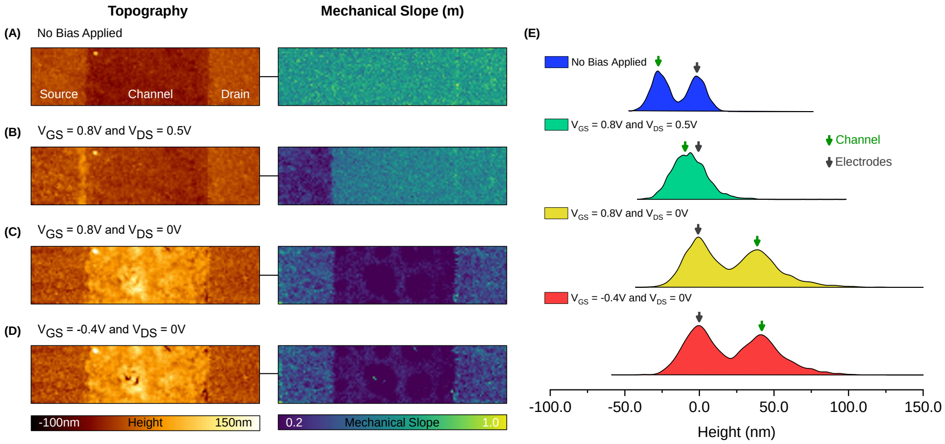

Figure 6.1: Preliminary measurements on N2200 glycolated OECTs. (A)-(D) Topographic and mechanical images as a function of bias voltages. (E) Histograms of the height distribution of the topographies in (A)-(D). The N2200 OECTs are fabricated by Fabrizio Antonio Viola at IIT Milano, Italy.

An example of a future potential study could be to investigate glycolated organic semiconductors such as N2200 which are specifically designed molecularly via the incorporation of the hydrophilic glycol side chain to the polymer backbone to facilitate water uptake and ion intercalation for efficient ionic-electronic coupling. N2200 consequently shows significant topographic changes and associated mechanical modulation, as shown by preliminary experiments in Figure 6.1. It would be interesting to compare such a system with respect to the BBL polymer which is a hydrophobic side-chain-free polymer and is still readily hydrated in an aqueous environment and works efficiently.

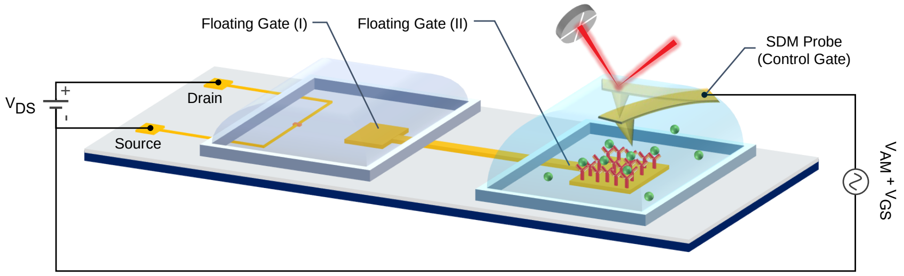

Figure 6.2: Possible implementation of in-liquid SDM on a functional electronic biosensor in a floating gate architecture for correlating local and macroscale response. The SDM tip probes the dynamic local electrical characteristics of a functionalized floating gate (II) where biorecognition events are happening while simultaneously acting as a control gate. The biosensor response is monitored macroscopically through drain current monitoring in the coupled EGT.

Another possible application is shown in Figure 6.2 where in-liquid SDM could be implemented on a working electronic biosensor in a floating gate architecture. The SDM probe can simultaneously act as a control gate and as an electrostatic force sensor probing the dynamic local electrical characteristics of a functionalized floating gate (II) where biorecognition events are happening. The coupled EGT via the floating gate (I) with floating gate (II) allows simultaneous monitoring of the bio-recognition events macroscopically through drain current monitoring. This probable implementation would allow correlating the local bio-recognition events with biosensor electrical response and could provide insights into the transduction mechanism.

In a nutshell, the current thesis provides crucial tools and methods for the fundamental investigation of the operating mechanism in electrolyte-gated devices, which eventually would aid in designing stable, reliable and efficient electronic devices for numerous applications in the field of biosensing and bioelectronics.

PART V

APPENDIX

Appendix A

Hardware Instrumentation

This appendix shows the hardware instrumentation of the in-Liquid SDM implementation on electrolyte-gated transistors photographically. A video demonstration of a typical in-Liquid SDM experiment (without automation) with explanations of various steps was created as part of the BORGES Training Workshop, which is available at https://youtu.be/VQSJnbmEMgE.

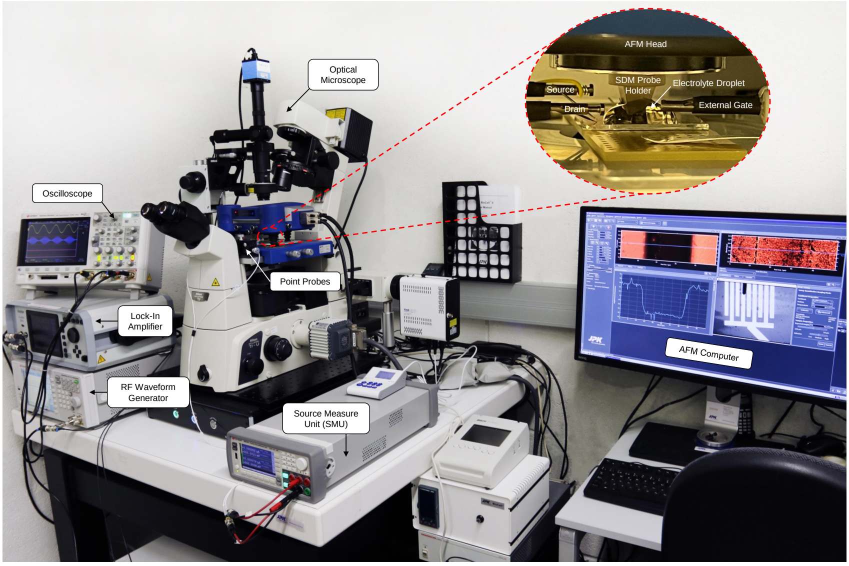

Figure A.1: Photo of in-Liquid SDM implementation on electrolyte-gated transistors with zoomed inset of the sample stage, with different coupled instruments coupled highlighted.

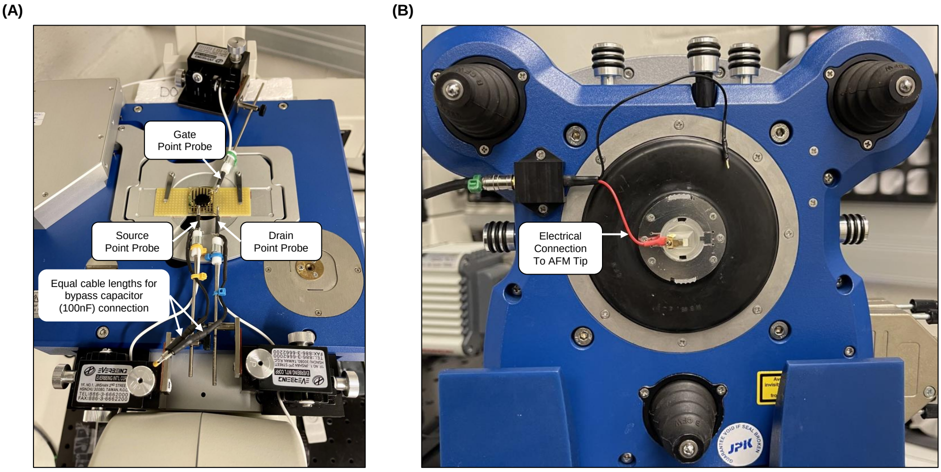

Figure A.2: (A) Point probe connections to the transistor highlighting Source, Drain and Gate probes. The connections to the external bypass capacitor are also highlighted. (B) Customized electrical connection to the AFM tip for applying the tip voltage.

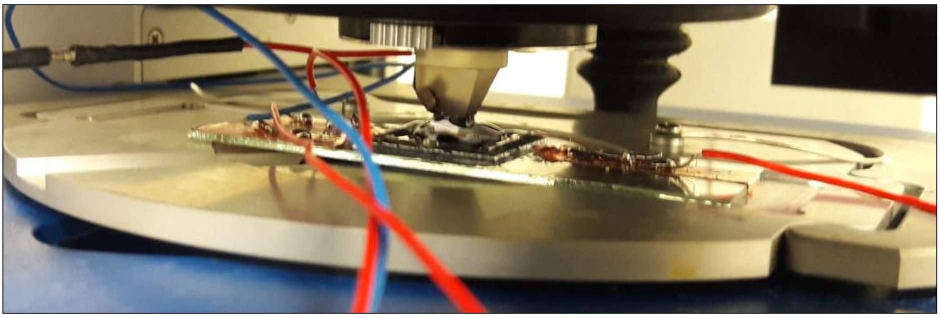

Figure A.3: Initial version of electrical connections to the transistor and AFM probe as implemented by Kyndiah et al. in subsection 1.6.4, showing permanent soldered and silver paste connections.

Appendix B

Python Automation and Analysis Toolbox

The *inLiquidSDM* custom Python package developed as part of this thesis for automated data acquisition and analysis is available at the GitHub repository:

https://github.com/shubhamtanwarphy/InstrumentControl.

The documentation is provided there detailing the structure and usage of the Python package with examples of the data analysis. Information regarding additional software and package installations for controlling the instruments is also provided. The *inLiquidSDM* package repository link provided above is maintained up-to-date with new functionalities/modules added as per requirements.

Appendix C

EGOFET Voltage Stability Window

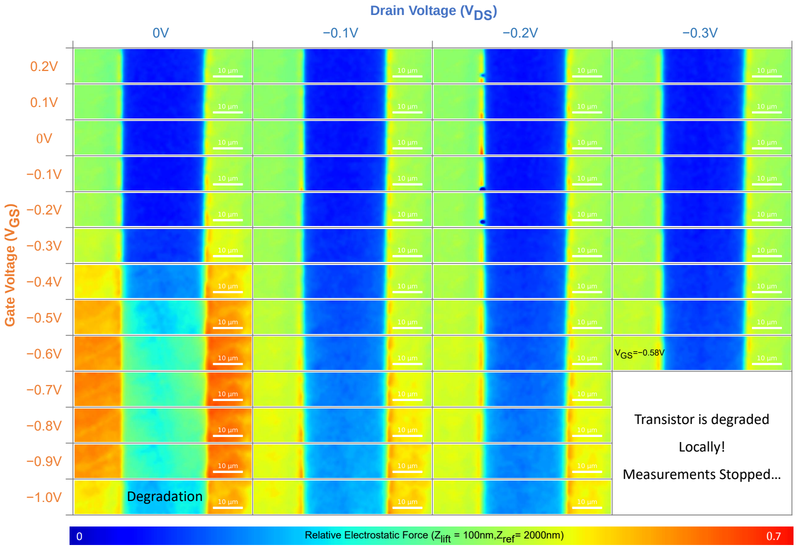

Transistor is degraded

Locally!

Measurements Stopped...

Figure C.1: Relative Electrostatic force images ($Z_{lift} = 100nm$ and $Z_{ref} = 2000nm$) for selected source-gate voltages and drain voltages. The full dataset contains images taken at ($\Delta V_{\mathrm{GS}} = 20mV$), starting with $V_{\mathrm{GS}} = 0.2V$ and ending with $V_{\mathrm{GS}} = -1.0V$; not all images are shown here for clarity. The measurements are stopped at $V_{\mathrm{DS}} = -0.3V$, $V_{\mathrm{GS}} = -0.58V$ due to the degradation of the transistor identified from the local electrical images not showing significant modulation as a function of gate voltage. The scale bar is $10\mu m$. Experimental parameters for in-liquid SDM measurements: Transistor: EGOFET based on DiF-TES-ADT:PS blend, Electrolyte: 1mM NaCl, Gate: Au SDM probe (HQ:NSC19/Cr-Au) + Pt external electrode, $f_{el} = 25MHz$, $f_{mod} = 10kHz$, $V_{ac} = 2VPP$, pixels 64×12, $k = 1.182N/m$, $s = 21.31nm/V$, $f_{res} = 35.45kHz$ (cantilever).

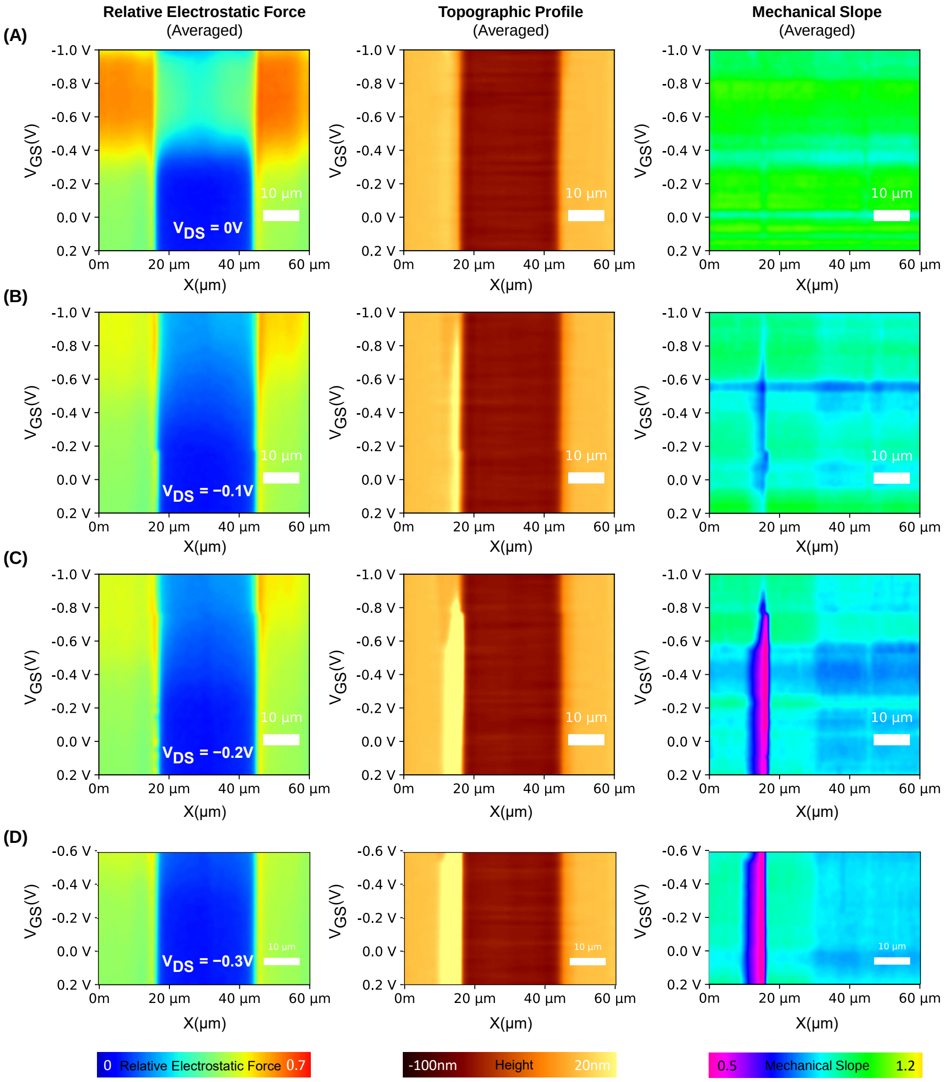

Figure C.2: Relative electrostatic force, topographic profile and mechanical slope spectrums across the source-channel-drain region as a function of gate voltage for the data shown in Figure C.1 for (A) $V_{DS} = 0V$, (B) $V_{DS} = -0.1V$, (C) $V_{DS} = -0.2V$, and (D) $V_{DS} = -0.3V$. Topographic changes are clearly visible on the source side of the transistor. The mechanical slope also indicates that the ions in the electrolyte have penetrated the semiconductor and made it softer which degraded the nanoscale evolution of local electrical properties of the measured EGOFET.

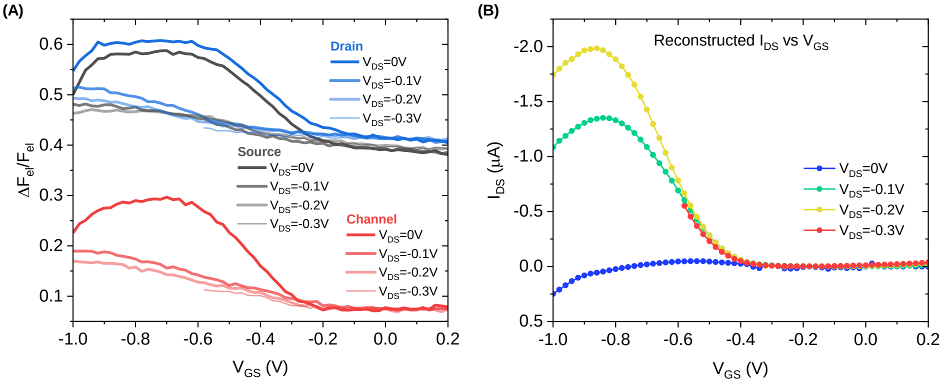

Figure C.3: (A) Relative electrostatic force trends on the middle of source, channel and drain region from the dataset in Figure C.2, showing the successive degradation. (B) Corresponding transfer curves reconstructed from the drain current recording during operando measurements. The drain current level is smaller than expected for these devices.

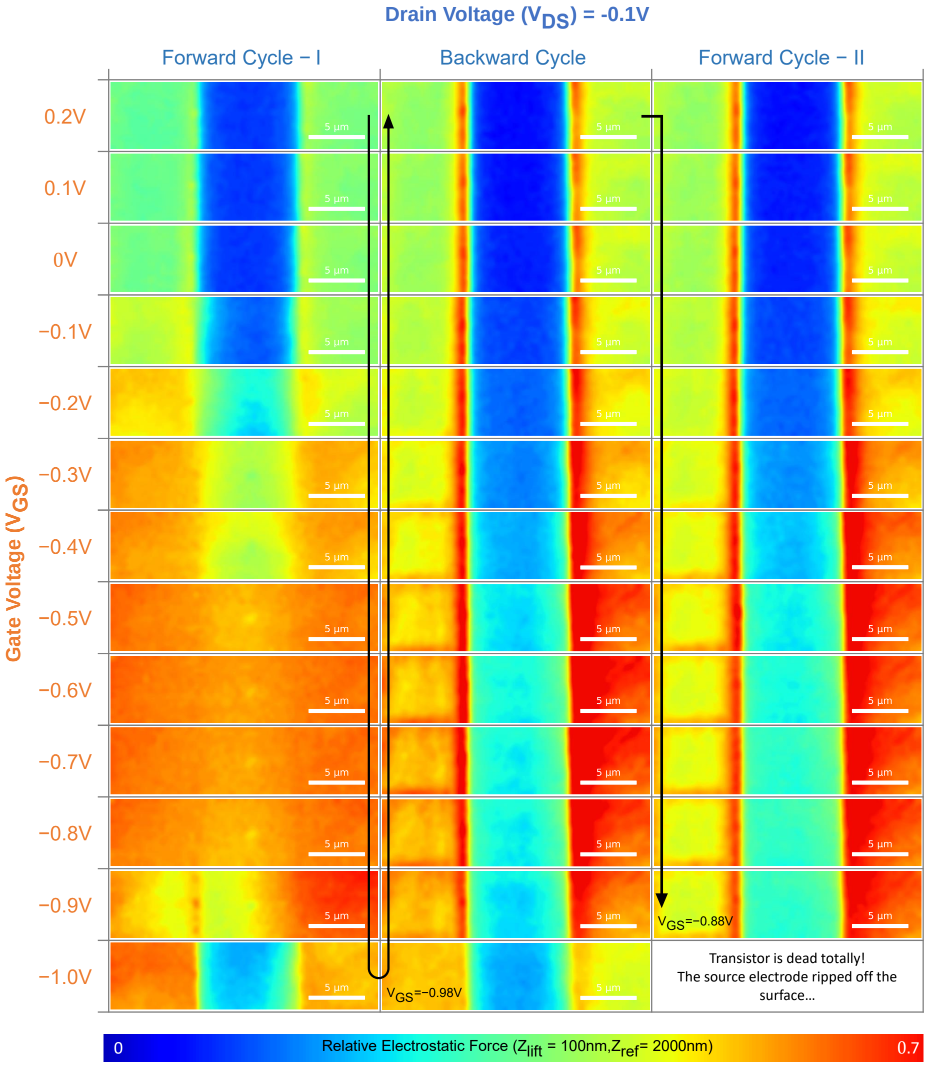

Figure C.4: Relative Electrostatic force images ($Z_{lift} = 100nm$ and $Z_{ref} = 2000nm$) for selected source-gate voltages in different cycles at the same drain voltage ($V_{\mathrm{DS}} = -0.1V$). The full dataset contains images taken at ($\Delta V_{\mathrm{GS}} = 20mV$), starting with $V_{\mathrm{GS}} = 0.2V$ and ending with $V_{\mathrm{GS}} = -1.0V$; not all images are shown here for clarity. The measurements are stopped in the second (II) forward cycle at $V_{\mathrm{GS}} = -0.88V$ because of the catastrophic damage of the device; the source electrode completely ripped off the surface, as shown in Figure C.7. The scale bar is $5\mu m$. Experimental parameters for in-liquid SDM measurements: Transistor: EGOFET based on DiF-TES-ADT:PS blend, Electrolyte: 1mM NaCl, Gate: Au SDM probe (HQ:NSC19/Cr-Au) + Pt external electrode, $f_{el} = 25MHz$, $f_{mod} = 10kHz$, $V_{ac} = 2VPP$, pixels 64×16, $k = 1.162N/m$, $s = 27.71nm/V$, $f_{res} = 35.68kHz$ (cantilever).

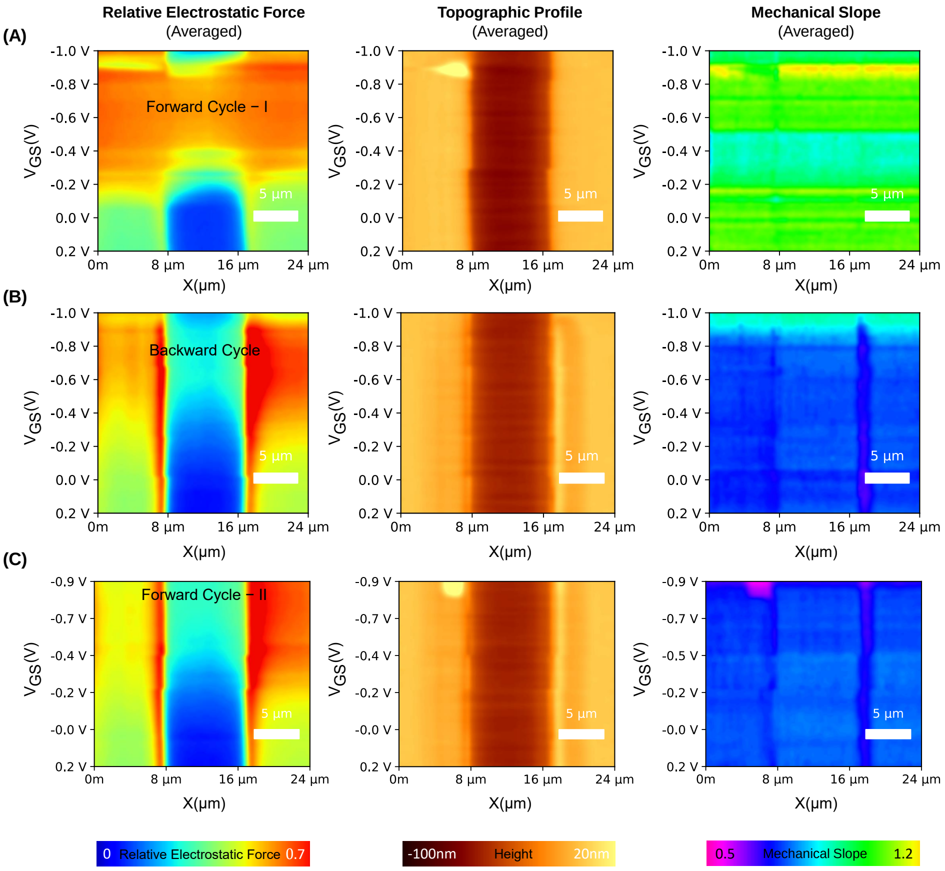

Figure C.5: Relative electrostatic force, topographic profile and mechanical slope spectrums across the source-channel-drain region as a function of gate voltage for the data shown in Figure C.4 for different cycles (A) Forward Cycle-I, (B) Backward Cycle, (C) Forward Cycle-II. Some topographic changes are visible at high gate voltages. The mechanical slope also indicates that the ions in the electrolyte have penetrated the semiconductor and made it much softer which ultimately caused catastrophic damage to the device, probably by exposing the electrodes which then are detached from the surface (Figure C.7) due to strong redox reactions at high gate voltages.

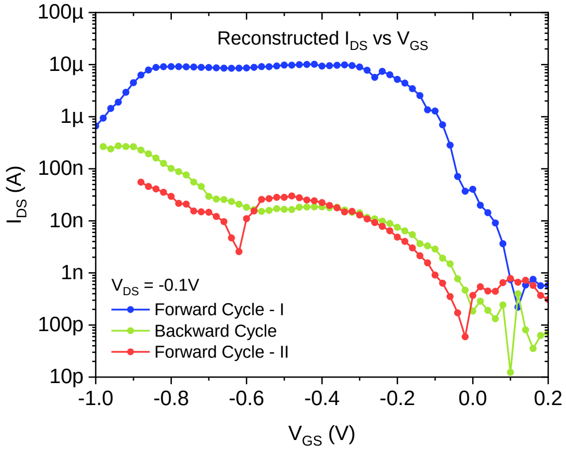

Figure C.6: Transfer curves reconstructed from the drain current recording during operando measurements shown in Figure C.5. The drain current clearly shows the degradation in successive cycles.

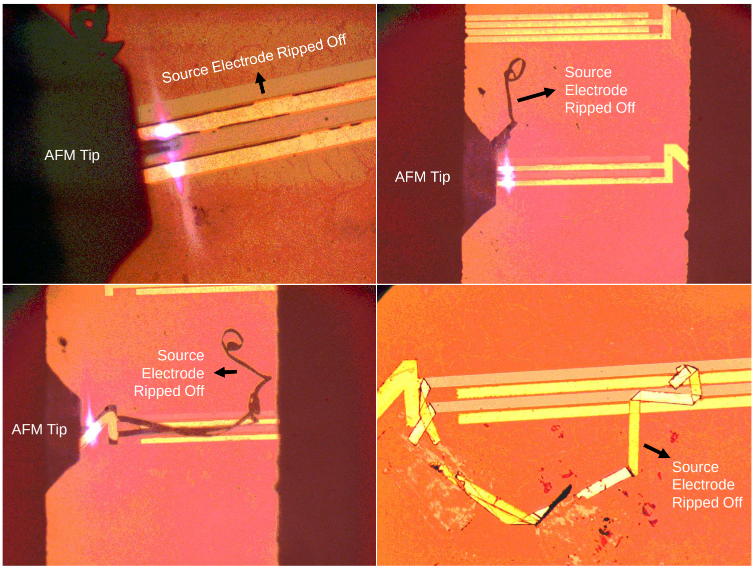

Figure C.7: Catastrophic damage of the device at high gate voltage. The source electrodes ripped off the surface. Corresponds to data shown in Figure C.4

Appendix **D**

List of Publications

- A. Kyndiah, M. Checa, F. Leonardi, R. Millan-Solsona, M. Di Muzio, **S. Tanwar**, L. Fumagalli, M. Mas-Torrent and G. Gomila, "Nanoscale Mapping of the Conductivity and Interfacial Capacitance of an Electrolyte-Gated Organic Field-Effect Transistor under Operation", *Adv. Funct. Mater.* 31, 2008032 (2021), DOI: 10.1002/adfm.202008032

- **S. Tanwar**, et. al., "Automated Scanning Probe Microscopy Toolbox for Functional Electrolyte-Gated Transistors", *(under preparation)*

- **S. Tanwar**, et. al., "Nanoscale Structure-Property-Function Mapping of Operating EGOFETs Reveals Bottlenecks to Charge Carrier Transport", *(under preparation)*

- **S. Tanwar**, et. al., "Simultaneous Multiscale and Multimodal Operando Characterization of Organic Electrochemical Transistors", *(under preparation)*

- **S. Tanwar**, "Lockdown taught me the value of reading the manual", *Nature* (2020) (**Non-scientific**), DOI: 10.1038/d41586-020-03566-w

[Google Scholar Link]

Appendix E

List of Conferences

- E-MRS 2023 Spring Meeting, Strasbourg, France, "Local Potential Mapping of Functional Electrolyte-Gated Transistors", (Oral)

- 15th IBEC Symposium on Bioengineering for Active Ageing (2022), Barcelona, Spain, "Probing Defects in Operating Electrolyte-Gated Organic Field-Effect Transistors at the Nanoscale", (Poster)

- 78th International Workshop & 6th Orbitaly (2022), Erice, Italy, "Imaging Functional Electrolyte-Gated Transistors at the Nanoscale", (Poster) - **ACS Omega Sponsored Best Poster Award**

- MRS 2022 Spring Meeting & Exhibit, Honolulu, Hawaii, "Nanoscale Electrical Characterisation of Functional Electrolyte-Gated Transistors by in-Liquid Scanning Dielectric Microscopy: Exploring Different Operating Regimes", (Oral)

- 7th International Winterschool on Bioelectronics - BioEl 2022, Kirchberg in Tirol, Austria, "Nanoscale Electrical Characterisation of Functional Electrolyte-Gated Organic Field-Effect Transistor by in-Liquid Scanning Dielectric Microscopy", (Poster)

- 2022 IBEC PhD Discussions, "Imaging Functional Organic Bioelectronic Platforms at the Nanoscale", (Invited Oral)

- 14th IBEC Symposium on Bioengineering for Regenerative Therapies (2021), Barcelona, Spain, "Exploring Different Operating Regimes of Electrolyte-Gated Organic Field-Effect Transistor at the Nanoscale", (Online Poster) - **Best Virtual Space by Popular Vote Award**

- 13th IBEC Symposium on Bioengineering for Future and Precision Medicine (2020), Barcelona, Spain, "Nanoscale Mapping of the Conductivity and Interfacial Capacitance of an Electrolyte Gated Organic Field Effect Transistor under Operation", (Online Oral Flash and Poster) - [Video Link]